APPLICATIONS OF SATELLITE RETRIEVALS IN DERIVING POLLUTANT EMISSIONS AND TRENDS

A Dissertation
Presented to
The Academic Faculty

by

Ruixiong Zhang

In Partial Fulfillment
of the Requirements for the Degree
Doctor of Philosophy in the
School of Earth and Atmospheric Sciences

Georgia Institute of Technology
December 2017

APPLICATIONS OF SATELLITE RETRIEVALS IN DERIVING POLLUTANT EMISSIONS AND TRENDS

Approved by:

Dr. Yuhang Wang, Advisor
School of Earth and Atmospheric Sciences
Georgia Institute of Technology

Dr. Rodney Weber
School of Earth and Atmospheric Sciences
Georgia Institute of Technology

Dr. Greg Huey
School of Earth and Atmospheric Sciences
Georgia Institute of Technology

Dr. Jintai Lin
School of Physics
Peking University

Dr. Nga Lee Ng
School of Earth and Atmospheric Sciences
School of Chemical and Biomolecular Engineering
Georgia Institute of Technology

Date Approved: November 2, 2017

To my parents, my parents-in-law, my wife Xue, Apollo and Loopal

ACKNOWLEDGEMENTS

I would like to address my deepest and most sincere thanks to my advisor, Dr. Yuhang Wang, who continuously supports my research with patient guidance, insightful advice, and invaluable trust. It is his never-failing enthusiasm for science filling my graduate studies with the joy of piecing together the puzzles and desire for what's next. I deeply appreciate my Ph.D. thesis committee members: Dr. Greg Huey, Dr. Nga Lee Ng, Dr. Rodney Weber, and Dr. Jintai Lin for their reviewing of this thesis, most helpful comments, and suggestions for my graduate studies.

My gratitude also goes to my colleagues in Wang's group, namely Dr. Tao Zeng, Dr. Yongjia Song, Dr. Dasa Gu, Dr. Ja-Ho Koo, Dr. Yuzhong Zhang, Tom Loadholt, Charles Smeltzer, Hang Qu, Jianfeng Li, Ye Cheng, Aoxing Zhang, and Qiyang Yan. I specially thank Hang Qu for being my roommate, collaborator and friend through my graduate life.

The distance in space and time never dims the ever-lasting love from my parents, my wife Xue, my little princesses Apollo and Loopal. They unconditionally support me to pursue my ideals without any reservation. I give my deepest gratitude to my parents who have always enlightened and encouraged me to discover the unknown and to face the challenges since my childhood.

TABLE OF CONTENTS

LIST OF TABLES

LIST OF FIGURES

LIST OF SYMBOLS AND ABBREVIATIONS

AMF	air mass factor
AMF_l	air mass factor for each vertical layer
AQS	Air Quality System
BC	black carbon
C_{CHOCHO}^{REAM}	model simulated glyoxal vertical column density
$C_{CHOCHO}^{SCIAMACHY}$	satellite observed glyoxal vertical column density
ΔC_{CHOCHO}	the difference between REAM simulated and satellite observed glyoxal vertical column density
CAPE	Convective Available Potential Energy
CBD	Central Business District
CFSR	Climate Forecast System Reanalysis
CG	cloud-to-ground lightning
CHOCHO	glyoxal
CONUS	contiguous United States
CTM	chemistry transport model
DAK	Doubling Adding KNMI
deNOx	denitrificiation
DI	Daily Inversion
DJF	December, January, and February
DOAS	Differential Optical Absorption Spectroscopy
DOMINOv2.0	Dutch OMI NO2 retrieval
DRI	Daily Retrieval-Inversion
ENVISAT	Environmental Satellite

EPA	Environmental Protection Agency
GFED4.1s	Global Fire Emissions Database Version 4.1 with small fires
GHG	greenhouse gas
GOME	Global Ozone Monitoring Instrument
GOME-2	Global Ozone Monitoring Experiment-2
GTOPO30	Geological Survey Global 30 Arc-Second Elevation
HDRI	High-resolution Daily Retrieval Inversion
hPa	hundred pascal
HTP	the Himalayas and the Tibetan Plateau
INTEX-b	Intercontinental Chemical Transport Experiment-Phase B
JJA	June, July, and August
KNMI	Royal Dutch Meteorological Institute
LT	local time
MAM	March, April and May
MEIC	Multi-resolution Emission Inventory for China
MODIS	MODerate-resolution Imaging Spectroradiometer
NAAQS	National Ambient Air Quality Standards
NCEP	National Centers for Environmental Prediction
NEI	National Emission Inventory
NLDN	National Lightning Detection Network
NO_2	nitrogen dioxide
NOx	nitrogen oxides
O_3	Ozone
OMI	Ozone Monitoring Instrument
PM	particulate matter

PMF	Positive Matrix Factorization
REAM	Regional chEmical trAnsport Model
RMB	renminbi (Chinese yuan)
RTM	radiative transfer model
SCD	slant column density
SCIAMACHY	SCanning Imaging Absorption spectroMeter for Atmospheric CHartographY
SCR	Selective Catalytic Reduction
SMOKE	Sparse Matrix Operator Kernel Emission
SNCR	Selective Non-Catalytic Reduction
SON	September, October, and November
TROPOMI	TROPospheric Monitoring Instrument
VCD	vertical column density
VOC	volatile organic compound
WRF	the Weather Research and Forecasting model
x_l	the real nitrogen dioxide profile
$x_{l,a\ priori}$	the a priori nitrogen dioxide profile

SUMMARY

Atmospheric pollutants are harmful to human health and ecosystem. Satellite retrievals of trace gases have been extensively used in quantifying pollutant emissions and identification of pollutant trends. This dissertation employs various satellite retrievals and the 3-D Regional chEmical trAnsport Model (REAM) to (1) identify and quantify the emission sources, and (2) derive pollutant trends.

First, we use short-lived reactive aromatics as proxies to diagnose transport of pollutants through the Himalayas to Tibet. In situ observations of short-lived reactive aromatics across the Tibetan Plateau are analyzed using REAM. The model performance using the current emission inventories over the region is poor due to problems in the inventories and model transport. Top-down emissions constrained by satellite observations of glyoxal (CHOCHO) are a factor of 2-6 higher than the bottom-up emissions over the industrialized Indo-Gangetic Plain. Using the top-down emissions, the agreement between model simulated and in situ observed aromatics improves. We find enhancements of reactive aromatics over Tibet by a factor of 6 on average due to rapid transport from India and nearby regions during the presence of a high-altitude cut-off low system. Our results suggest that the cut-off low system is a major pathway for long-range transport of pollutants such as black carbon. The modeling analysis reveals that even the state-of-the-science high-resolution reanalysis cannot simulate this cut-off low system accurately, which probably explains in part the underestimation of black carbon deposition over Tibet in previous modeling studies. Another model deficiency of underestimating pollution transport from the south is due to the complexity of terrain, leading to enhanced transport.

It is therefore challenging for coarse-resolution global climate models to properly represent the effects of long-range transport of pollutants on the Tibetan environment and the subsequent consequence for regional climate forcing.

Second, we derive anthropogenic NOx emissions with 4km spatial resolution using Ozone Monitoring Instrument (OMI) NO_2 retrieval in Yangtze River region during June-July-August (JJA) of 2005-2009 and 2010-2015. The NOx emission inversion using High-resolution Daily Retrieval-Inversion (HDRI) method proves powerful in quantifying the effects of urbanization. The traditional bottom-up emission approach and super-sampling of satellite NO_2 VCDs have difficulty diagnosing the detailed NOx emission changes, because of the low resolution and the spatial smoothing of data, respectively. Due to the high economic portion of service sector, Pudong New Area of Shanghai has the smallest NOx emission per gross domestic product (GDP) of 302±15, 181±7ton yr^{-1} per billion RMB during the two periods, compared to the regional average of 905±38, 504±16ton yr^{-1} per billion RMB. The rapid development in Pudong New Area results in a 13±5% NOx emission increase, despite the NOx emission reduction of 8±8% in Shanghai. Although the total coal-fired powerplant capacities in the region increases by about 50%, the total coal-fired powerplant NOx emissions decrease by 6%. This results from the implementation of denitrification (deNOx) systems in coal-fired powerplants, which reduces the averaged NOx emission factor from 2.8±0.2 g/kWh during 2005-2009 to 1.8±0.1g/kWh during 2010-2015.

Finally, we retrieve OMI tropospheric NO_2 VCDs and obtain the NO_2 relative trends over the United States, which are compared with coincident in situ measurements from the Air Quality System (AQS) network. The Mann-Kendall method is applied to

derive the NO_2 seasonal and annual trends for four regions at coincident sites during 2005-2014. The OMI-based NO_2 seasonal relative trends are generally biased high compared to the in situ trends by up to 3.7% yr^{-1}, except for the underestimation in the Midwest and Northeast during Dec-Jan-Feb (DJF). We improve the OMI retrievals for trend analysis by removing the ocean trend, using MODerate-resolution Imaging Spectroradiometer (MODIS) albedo data in air mass factors (AMFs) calculation, and applying lightning event filter to screen data. These improvements result in close agreement (within 0.8% yr^{-1}) between in situ and OMI-based NO_2 annual relative trends. Thus, we recommend future studies to apply these procedures to ensure the quality of satellite-based NO_2 trend analysis, especially in regions without reliable long-term in situ NO_2 measurements. We derive optimized OMI-based NO_2 annual relative trends using all available data for the West (-2.8%±0.4 yr^{-1}), Midwest (-2.4%±0.4 yr^{-1}), Northeast (-3.5%±0.5 yr^{-1}), South (-1.3%±0.3 yr^{-1}). The OMI-based annual mean trend over the contiguous United States is -2.0%±0.2 yr^{-1}. It is a factor of 2 lower than that of the AQS in situ data (-3.9%±0.4 yr^{-1}); the difference is mainly because the locations of AQS sites are concentrated in urban and suburban regions.

CHAPTER 1. INTRODUCTION

1.1 Statement of the Problem

Atmospheric pollutants such as nitrogen dioxide (NO_2) and aromatics are detrimental to the environment (e.g., acid rain) and human health (e.g., respiratory diseases, cancers) despite that they only account for a small fraction of the atmosphere (Liu et al., 2012a, 2012b; Gu et al., 2013). Also, pollutants play active roles in the atmosphere, as NO_2 and Volatile Organic Compounds (VOCs) can serve as precursors of ozone (O_3) and initiate photochemistry. Although the chemistry mechanism has been widely studied, there remains two questions to be answered: (1) what the pollutant sources are, and (2) how the pollutants change overtime. These two questions are essential for environmental policy makers to carry out effective regulations and evaluate existing pollutant trends.

In this dissertation, I use different satellite retrievals and the 3-D Regional chEmical trAnsport Model (REAM) to (1) identify and quantify the emission sources, and (2) derive pollutant trends. Specifically, to achieve the first objective, I will investigate the sources of observed aromatics in the Tibetan Plateau, and derive high-resolution nitrogen oxides ($NOx=NO+NO_2$) emissions in Yangtze River region. In the latter topic, I will calculate the satellite-based NO_2 trends in the U.S. These studies are discussed in CHAPTER 2, CHAPTER 3, and CHAPTER 4, respectively.

1.1.1 Identification of Emission Sources

Most atmospheric pollutants in urban areas, where pollution is most concerned, are anthropogenically emitted (e.g., Gu et al., 2013). The most common way to quantify the anthropogenic emission sources is the bottom-up approach, in which researchers utilize

statistics, measured emission factors, and spatial proxies to estimate anthropogenic activities and subsequent emissions (Streets et al., 2003; Zhang et al., 2009). However, the bottom-up approach is limited to the data availability (Zhao and Wang, 2009; Gu et al., 2013), resulting in large uncertainties in developing regions.

Space-based observations serve as excellent proxies for specific pollutant species, complementing the ground-based data (Zhao and Wang 2009; Liu et al., 2012a; Gu et al., 2013, 2014, 2016). Satellite instruments provide global coverage, frequent and consistent measurements. Researches have used different inverse modelling techniques to constrain emissions from satellite concentrations.

Beirle et al. (2011) developed a method to infer top-down NO_2 emission of an isolated megacity without a chemistry transport model (CTM). The NOx lifetime is estimated by the shift of satellite observed NO_2 plume under different wind scenarios. The total emission of the city can be calculated using the NO_2 vertical column densities (VCDs) and the NOx lifetime. This simplified approach assumes that the target city or powerplant is a point emission source and is not applicable to city clusters. The uniformly estimated NOx lifetime introduces additional error due to the chemical non-linearity (Gu et al., 2013). Also, this method is only performed on a city level and does not fully make use of the spatial information from the satellite.

Martin et al. (2003) applied a CTM to Global Ozone Monitoring Instrument (GOME) NO_2 retrievals to derive monthly NO_2 emissions (2°×2.5°). In this approach, the top-down NO_2 emissions are calculated based on the a priori emissions (usually bottom-up emissions) and the ratio between satellite retrieved and CTM simulated NO_2 VCDs. The top-down emission estimates are considered as the observations in the Bayesian method. The a posteriori emissions are then derived using the top-down emissions, the a priori

emissions, and the corresponding errors. Zhao et al. (2009) improved this approach by iteratively calculating the a posteriori emissions and updating the a priori emissions on a daily basis. Gu et al. (2014) included online NO_2 retrieval on the basis of previous works, further reducing the emission uncertainty. This method incorporates NO_2 retrievals from Ozone Monitoring Instrument (OMI) and achieves higher spatial resolution (70km×70km).

The latest generation of satellite trace gas monitoring instrument, the TROPospheric Monitoring Instrument (TROPOMI, Veefkind et al., 2012), was launched in October 2017. It features much higher spatial resolution (7km×7km at nadir), surpassing all its predecessors (e.g., 13km×24km at nadir for OMI). New emission inversion method is needed to fully unleash the potential of TROPOMI. As discussed in CHAPTER 3, we develop the High-resolution Daily Retrieval Inversion (HDRI) technique (4km×4km) and estimate the NOx emissions from OMI retrievals in Yangtze River region.

Some atmospheric pollutants, which are not directly measured by satellite instruments, can be indirectly inferred. Shim et al. (2005) constrained global isoprene from GOME formaldehyde (HCHO) measurements. Liu et al. (2012a) derived the anthropogenic aromatic emissions in China with the SCanning Imaging Absorption spectroMeter for Atmospheric CHartographY (SCIAMACHY) glyoxal (CHOCHO) retrieval. The precursors of CHOCHO include isoprene, aromatics, acetylene, and ethylene. With the implementation of the REAM CTM, Liu et al. (2012a) found that the underestimation of simulated CHOCHO VCDs mainly resulted from the low bias of the bottom-up aromatic emissions instead of other precursors. The top-down aromatics were then estimated based on the difference between the retrieved and simulated CHOCHO VCDs.

The Tibetan Plateau, also referred as “the Third Pole”, has little local anthropogenic emissions. However, Li et al. (2017) found the observed VOCs are much higher than the Arctic and Antarctic regions. The Positive Matrix Factorization (PMF) model showed that the VOCs were emitted from industry, biomass burning, and transportation. The back-trajectory model result revealed that the air mass was transported from the industrialized Indo-Gangetic Plain. Considering the high altitude of the Himalayas, it is unclear how the pollutants penetrated this natural barrier. Although different pollutants share various physical and chemical properties, other pollutants such as black carbon (BC) can be transported into the Tibetan Plateau in a similar manner. Uunderstanding this transport mechanism is hereby important. We follow Liu et al. (2012) and use the indirect emission inversion method to investigate the source and transport mechanism of the observed aromatics in CHAPTER 2.

1.1.2 Satellite-based NO_2 Trends

NO_2 trend analysis is essential to quantify the effectiveness of current environmental policies and carry out new NO_2 regulations. Even the more robust emission inventories lack temporal representativeness and are not suitable for trend analysis. For example, U.S. National Emission Inventory (NEI) only updates triennially due to the high time costs to collect and process the data. Surface NO_2 measurements (e.g., the Environmental Protection Agency (EPA) Air Quality System (AQS) network) are usually located in more urbanized cities, leaving majority of area uncovered (Lamsal et al., 2015).

Thus, satellite NO_2 retrievals have been widely used to identify the NO_2 temporal evolution, including NO_2 changes during the economic recession (Lin et al., 2010; Gu et

al., 2013), NO_2 reduction during Beijing Olympics (Yang et al., 2011), and other NO_2 trend studies (Lin et al., 2011; Castellanos et al., 2012; Russell et al., 2012; Lamsal et al., 2015; Lu et al., 2015; Tong et al., 2015; Cui et al., 2016; Duncan et al., 2016; de Foy et al., 2016a, 2016b; Krotkov et al., 2016; Liu et al., 2017).

The NO_2 retrieval algorithm is not specifically designed for trend analysis. Whether satellite NO_2 VCDs are suitable for trend analysis is yet to be studied. The U.S. EPA AQS NO_2 monitoring network acts as a good proxy to evaluate OMI-based trend. Previous studies have found the non-negligible divergence between OMI-based and AQS in situ NO_2 trends.

Tong et al. (2015) reported that OMI-based NO_2 trend was biased high (-35%) compared to in situ trend (-38%) from 2005 to 2012 in eight cities. Lamsal et al. (2015) also found that the annual NO_2 trend inferred from OMI differed from the EPA AQS in situ trend. The OMI-based and in situ NO_2 trends were -4.8% yr^{-1} vs -3.7% yr^{-1} during 2005-2008, and -1.2% yr^{-1} vs -2.1% yr^{-1} during 2010-2013. Lamsal et al. (2015) suggested that the divergence between the two datasets could result from high NO_2 concentrations in the free troposphere, poor spatial representativeness, high uncertainties in less polluted regions, and interference in AQS NO_2 measurements.

Although NO_2 satellite retrievals are potentially useful for trend analysis in regions without long-term ground-based NO_2 monitoring network, this discrepancy between OMI-based and EPA AQS in situ trends may reduce the credibility of trend analysis using satellite data. It is therefore crucial to understand how the NO_2 retrieval procedures affects the resulting OMI-based trends and whether this disagreement can be diminished or eliminated. We discuss the necessary procedures to ensure the quality of NO_2 retrieval and derive OMI-based NO_2 trend in CHAPTER 4.

1.2 Description of REAM Model

We use the 3-D REAM to examine the chemistry evolution and regional transport of aromatics (CHAPTER 2), to perform inverse modelling of pollutant emissions (CHAPTER 2, CHAPTER 3), and to retrieve pollutant VCDs with a radiative transfer model (RTM) (CHAPTER 3, CHAPTER 4).

REAM has been used in previous studies, including large-scale transport (Wang et al., 2006; Zhao et al., 2009a, 2010), vertical transport (Zhao et al., 2009b; Zhang et al., 2014, 2016), emission estimates (Zhao and Wang, 2009; Liu et al., 2012a; Gu et al., 2013, 2014, 2016) and other air quality studies (Zeng et al., 2003, 2006; Choi et al., 2005, 2008a, 2008b; Wang et al., 2007; Liu et al.,2010, 2012b, 2014; Gray et al., 2011; Yang et al., 2011; Zhang and Wang, 2016; Zhang et al., 2017; Cheng et al., 2017).

REAM has 30 vertical levels in the troposphere and 5 vertical levels in the stratosphere. The model top is at 10 hpa. The spatial resolution of REAM is set as 36km in CHAPTER 2 and CHAPTER 4, and 4km in CHAPTER 3. Meteorological fields in REAM are obtained from the Weather Research and Forecasting model (WRF) assimilations constrained by National Centers for Environmental Prediction (NCEP) Climate Forecast System Reanalysis (CFSR, Saha et al., 2010) 6-hourly products, which have a horizontal resolution of T382 (~38 km). We run the WRF model with the same resolution as in REAM. Meteorological inputs related to convective transport are updated every 5 minutes while the others are updated every 30 minutes. The KF-eta scheme is used for sub-grid convective transport in WRF (Kain and Fritsch,1993).

The recent update of REAM expands the GEOS-Chem standard chemical mechanism (V9-02) to include a detailed description of SAPRC-07 aromatic chemistry (Bey et al., 2001; Liu et al., 2010, 2012a; Zhang et al., 2017). We use the Multi-resolution Emission Inventory for China (MEIC), the Intercontinental Chemical Transport Experiment-Phase B (INTEX-B, Zhang et al., 2009, Li et al., 2014), and the National Emissions Inventory (NEI) emission inventories for anthropogenic emissions from China, South Asia and the U.S., respectively. REAM calculates biogenic emissions using the Model of Emissions of Gases and Aerosols from Nature (MEGAN) algorithm (v2.1) (Guenther et al., 2012; Zhang et al., 2016). Soil NOx emissions and lightning NOx are both parameterized in REAM, following Wang et al. (1998) and Choi et al. (2005), respectively.

For recent model evaluations of REAM, we refer readers to Zhang et al. (2016), Zhang and Wang (2016), Cheng et al. (2017), and Zhang et al. (2017).

1.3 Description of Satellite Retrievals

1.3.1 SCIAMACHY CHOCHO Retrieval

We use the CHOCHO retrieval from the SCIAMACHY in CHAPTER 2 to determine the aromatic emissions in South Asia during October 2010. SCIAMACHY onboard Environmental Satellite (ENVISAT) operated from 2002 to 2012 (Burrows et al., 1995; Bovensmann et al., 1999), with an overpassing time at about 10:00 AM local time (LT). SCIAMACHY made passive measurements of the upwelling radiation from the top of the atmosphere in alternate nadir and limb viewing geometry. CHOCHO VCDs are retrieved through mathematical inversion of SCIAMACHY measurements. The retrieval

uses the Differential Optical Absorption Spectroscopy (DOAS) technique (Wittrock et al., 2006; Vrekoussis et al., 2009; Alvarado et al., 2014). The CHOCHO retrieval used in this study is based on the algorithm developed in Alvarado et al. (2014), which includes corrections for the interferences with NO_2 over the regions with high NOx emissions as well as liquid water over oceans (Alvarado, 2016). The detection limit for SCIAMACHY CHOCHO VCD is about $1\times10^{14}\ molecules\ cm^{-2}$. The overall monthly uncertainty of CHOCHO VCDs ($C_{CHOCHO}^{SCIAMACHY}$) in the selected region during October 2010 is given by $\alpha\times C_{CHOCHO}^{SCIAMACHY} + 1\times10^{14}\ molecules\ cm^{-2}$, where the value of α is in a range of 0.1 to 0.3.

1.3.2 OMI NO_2 Retrieval

We use OMI NO_2 retrieval in REAM evaluation (CHAPTER 2), NO_2 emission inversion (CHAPTER 3), and NO_2 trend analysis (CHAPTER 4). We derive tropospheric NO_2 VCDs from the Royal Dutch Meteorological Institute (KNMI) Dutch OMI NO2 retrieval (DOMINOv2.0, Boersma et al., 2011). OMI onboard Aura was launched in July 2004 and is still active now. OMI overpasses the equator at about 13:30 LT and achieves global coverage with 2600 km viewing swath spanning 60 rows. OMI features up to $13km\times24km$ ground level spatial resolution at nadir. DOMINOv2.0 product derives NO_2 slant column densities (SCDs) from a fitting window of 405-465nm of backscattered sunlight. The stratospheric portion of SCDs are estimated and subsequently removed with the implementation of a global CTM TM4 (Boersma et al., 2007). Deriving tropospheric VCDs from the residual tropospheric SCDs requires the calculation of tropospheric air

mass factors (AMFs). The AMF is determined by the a priori NO_2 vertical profile, the surface reflectance, cloud fraction and pressure, the pressure and temperature profile, and the satellite viewing geometry (Boersma et al., 2011).

As an optically thin gas, tropospheric AMF for NO_2 can be calculated from AMF for each vertical layer (AMF_l) weighted by NO_2 VCDs at the corresponding layer (x_l) (Palmer et al., 2001; Boersma et al., 2004), as shown in Equation 1.

$$tropospheric\ AMF = \frac{tropospheric\ SCD}{tropospheric\ VCD} = \frac{\int AMF_l x_l dl}{\int x_l dl} \quad (1)$$

As the vertical distribution of NO_2 is usually unknown, we typically substitute x_l by an a priori profile ($x_{l,a\ priori}$) from a CTM. AMF_l is the sensitivity of NO_2 absorption at a given altitude weighted by NO_2 abundance (Palmer et al., 2001; Eskes and Boersma, 2003), and is computed using a RTM. As in DOMINOv2.0 standard product, the NO_2 profiles are from TM4 with 3°×2° spatial resolution and 35 vertical layers, and AMF_l is calculated by Doubling Adding KNMI (DAK) RTM.

1.4 Scope of This Work

With the implantation of the satellite retrievals as well as the 3-D REAM CTM, this dissertation (1) identifies the source of aromatics observed in the Tibetan Plateau of China; (2) derives high resolution NOx emissions from OMI retrieval in Yangtze River region of China; and (3) calculates the relative trends of NO_2 in the U.S.

Each of these three objectives is presented as a separate chapter. The remainder of this dissertation is organized as follows.

Chapter 2, "Enhanced trans-Himalaya Pollution Transport to the Tibetan Plateau by the Cut-off Low System", investigates rapid aromatics transport pathway in the presence of a 300hpa cut-off low from South Asia towards the Tibetan Plateau. The updated aromatic emissions in the South Asia using satellite retrieval explains the underestimation of the model simulated aromatics. Model shows that the air mass fluxes across the Himalayas increase by a factor of 2-5 when the cut-off low is presented. The subsequent increasing transport of aromatics constitutes the majority of aromatics in the Tibetan Plateau.

Chapter 3, "NOx Emission Changes due to Urbanization and Powerplant Denitrification in Yangtze River Region", develops and applies the High-resolution Daily Retrieval Inversion (HDRI) method to derives NOx emission from OMI retrieval in Yangtze River region during 2005-2009 and 2010-2015. The HDRI NOx emissions reveal more details (4km×4km) than the bottom-up emission inventory (0.25°×0.25°), showing that anthropogenic NOx emissions shift from industrialized regions towards more urbanized regions in big cities. Small cities and fast developing regions feature high emission growth. The application of deNOx system successfully decreases the NOx emissions from coal-fired powerplants by 6%, despite the increase of the total electricity generation capacity by about 50%.

Chapter 4, "Reconciling the Differences between OMI-based and EPA AQS In Situ NO2 Trends", evaluates and derives NO_2 relative trends from OMI NO_2 VCDs in the U.S. during 2005-2014. Three procedures are necessary to ensure a robust trend analysis, i.e. (1) ocean trend removal, (2) MODerate-resolution Imaging Spectroradiometer (MODIS) albedo update in AMFs calculation, and (3) lightning event filter. These corrections bring OMI-based NO_2 annual trends close (<0.8% yr^{-1}) to the trends derived from coincident EPA AQS sites. Using all available data, we find that the OMI-based NO_2 reduction is less than the in situ one by a factor of 2. This results from the fact that EPA AQS sites are located in more polluted urban areas while OMI covers urban and rural areas alike. This is further confirmed since that OMI-based reduction rates increase almost linearly with higher observed NO_2 VCDs. As a result, the annual relative NO_2 trends are more evident in polluted areas than clean regions.

Chapter 5, "Conclusions and Future Works" presents the summary of this dissertation and recommendations for future studies.

CHAPTER 2. ENHANCED TRANS-HIMALAYA POLLUTION TRANSPORT TO THE TIBETAN PLATEAU BY THE CUT-OFF LOW SYSTEM[1]

2.1 Introduction

The Tibetan Plateau, commonly referred as the Third Pole and the last pristine land of the Earth, has drawn much attention in environmental and climate research in recent years (Menon et al., 2002). Although Tibet appears to be isolated from industrialized regions due in part to the transport barrier by its being a plateau and its pollutant concentrations being generally low, the Third Pole is vulnerable to regional climate change. Areas of the Tibetan Plateau over 4 km in altitude are warming at a rate of 0.3 °C per decade, twice as fast as the global average (Xu et al., 2009). In addition to the increase of greenhouse gases (GHGs) and the associated global warming, BC is likely another important contributor to the warming of the Tibetan Plateau. The deposition of BC on the vast glaciers of the Tibetan Plateau will decrease the surface albedo, accompanied by increased sunlight absorption and subsequent enhanced melting (Hansen and Nazarenko, 2004; Ramanathan and Carmichael, 2008; Ming et al., 2009; Yasunari et al., 2010).

[1] This chapter is an extension of "Enhanced trans-Himalaya Pollution Transport to the Tibetan Plateau by the Cut-off Low System", published in Atmospheric Chemistry and Physics. The co-authors are Ruixiong Zhang, Yuhang Wang, Qiusheng He, Laiguo Chen, Yuzhong Zhang, Hang Qu, Charles Smeltzer, Jianfeng Li, Leonardo M.A. Alvarado, Mihalis Vrekoussis, Andreas Richter, Folkard Wittrock, and John P. Burrows.

Increasing BC concentrations were previously found in ice core and lake sediment records (Xu et al., 2009; Cong et al., 2013). The dwindling of glaciers over Tibet is a major concern for fresh water supply to a large portion of the Asian population through the Indus River, Ganges River, Yarlung Tsangpo River, Yangtze River and Yellow River (Singh and Bengtsson, 2004; Barnett et al., 2005; Lutz et al., 2014). Though melting glaciers favor river runoff temporarily, mass loss of glaciers endangers water supply during the dry season in the future (Yao et al., 2004; Kehrwald et al., 2008).

Besides narrowing the uncertainties of BC emissions, aging and deposition, better understanding the transport pathways are equally important in this region. Surrounded by the largest BC sources of East Asia and South Asia (Bond et al., 2007; Ohara et al., 2007), Tibet is primarily affected by pollutant transport from these two regions (Kopacz et al., 2011; Lu et al., 2012; Zhao et al., 2013; Wang et al., 2015; Zhang et al., 2015; Li et al., 2016; Wang et al., 2016; Kang et al., 2016). Kopacz et al. (2011) attempted to identify the sources of BC over glaciers in the Himalayas and the Tibetan Plateau (HTP) using the adjoint model of GEOS-Chem. Lu et al. (2012) developed a novel back-trajectory model with BC emissions, hydrophilic-to-hydrophobic aging, and deposition and found that South Asia and East Asia account for 67% and 17% of BC over the HTP. Using source tagging, biofuel and biomass burning emissions from South Asia are found to be the largest sources of BC in HTP followed by fossil fuel combustion emissions (Zhang et al., 2015). Hindman and Upadhyay (2002) suggested that the vertical lifting due to convection and subsequent horizontal mountain-valley wind lead to the transport of aerosols from Nepal to Tibet. Dumka et al. (2010) also stressed the importance role of mountain-valley wind in BC

concentration in Central Himalayas. Cong et al. (2015) suggested that both the large-scale westerlies from South Asia and the local mountain-valley wind from South Asia are major transport pathways. The synoptic scale trough and ridge can potentially lead to the trespassing of atmospheric brown clouds from South Asia to the Tibetan Plateau (Lüthi et al., 2015). Ji et al. (2015) indicated that the southwesterlies during monsoon season favor aerosols transport across the Himalayas from South Asia. Aerosols observations in previous studies are mostly limited to the southern and northern slopes of the Himalayas (Hindman and Upadhyay, 2002; Dumka et al., 2010; Cong et al., 2015) with very few in situ sites (e.g. Namco, Linzhi) inside Tibet (Kopacz et al., 2011; Ji et al., 2015; Lüthi et al., 2015; Zhang et al., 2015). Considering the complex topography (Lawrence and Lelieveld, 2010; Ménégoz et al., 2013; He et al., 2014; Kumar et al., 2015) and scarce observations (Maussion et al., 2011), it is crucial to evaluate model simulated transport performance over the Tibetan Plateau using available observations with a good spatial coverage. Observation-constrained modeling is needed to better understand potential model biases due to the uncertainties of model simulated transport from South Asia to Tibet.

In this study, we use short-lived reactive aromatics as proxies to diagnose transport of pollutants to Tibet. In situ observations of short-lived reactive aromatics across the Tibetan Plateau are analyzed (Section 2.2.1). Anthropogenic emissions including fossil fuel combustion, gasoline evaporation and solvent use constitute the main sources of atmospheric aromatics (Sack et al., 1992; Fu et al., 2008; Henze et al., 2008; Cagliari et al., 2010; Cabrera-Perez et al., 2016). Biofuel and biomass burning is another important source (Fu et al., 2008; Henze et al., 2008). The main sink of aromatics is hydroxyl radical (OH)

oxidation with lifetimes ranging from hours to days (Atkinson, 2000; Liu et al., 2012a). We use satellite observations to minimize the biases of emission inventories for upwind regions of Tibet (Sections 2.2.2, 2.2.3 and 2.2.4) and then apply a regional chemistry and transport model constrained by high-resolution reanalysis meteorological data to understand missing transport processes in model simulations (Section 2.3). On the basis of these results, we examine the implications for global climate modeling studies of anthropogenically driven changes over the Tibetan Plateau (Section 2.4).

2.2 Methods

2.2.1 In Situ Aromatic Data

Whole air samples were collected in 2-L electro-polished stainless-steel canisters, which had been cleaned and vacuumed according to the TO-15 method issued by US EPA before shipment to the sampling sites (Zhang et al., 2012). The restricted grab sampler (39-RS-x; Entech), which has a 5-μm Silonite-coated metal particulate filter, was placed on the inlet of the canister to completely filter out dust and other particulates during sampling. These samples were taken in daytime from 8:00 AM to 7:00 PM with an interval of 1 to 2 hours. The sampling time was 5 minutes to fill the vacuumed canisters. The filled canisters were transported back to the laboratory of Guangzhou Institute of Geochemistry, Chinese Academy of Science. Each air sample was analyzed for 65 light non-methane hydrocarbons species. The samples were pretreated by an Entech Model 7100 Preconcentrator (Entech Instruments Inc., California, USA), and analyzed by a gas chromatography-mass selective detector (GC-MSD/FID, Agilent 7890A/5973N, USA) using dual columns and dual detectors to simultaneously analyze both low- and high-boiling-point VOCs with each injection. The detailed analytical procedure is described by Zhang et al. (2012).

In this study, we analyze 65 measurements of aromatics (benzene, toluene, ethyl-benzene, m/p/o-xylene) and wind speed measurements taken across Tibet during October 2010 (Figure 2.1). Care was taken in sampling such that there were no direct urban, industrial, or road emissions in the upwind direction of the sampling location. The lifetimes of toluene, ethyl-benzene, m/p/o-xylene are relatively short (2-20 hours) and these reactive aromatic compounds therefore provide observational constraints for transport from India and nearby regions to Tibet. We group the samples into three periods based on the time and locations of the measurements, i.e. Period 1 from October 13 to 17, 2010 to the north of the Himalayas along the southern border of Tibet, Period 2 from October 19 to 24 across the interior of the Tibetan Plateau, and Period 3 of October 25 to the west of the Yarlung Tsangpo Grand Canyon in southeastern Tibet (Figure 2.1).

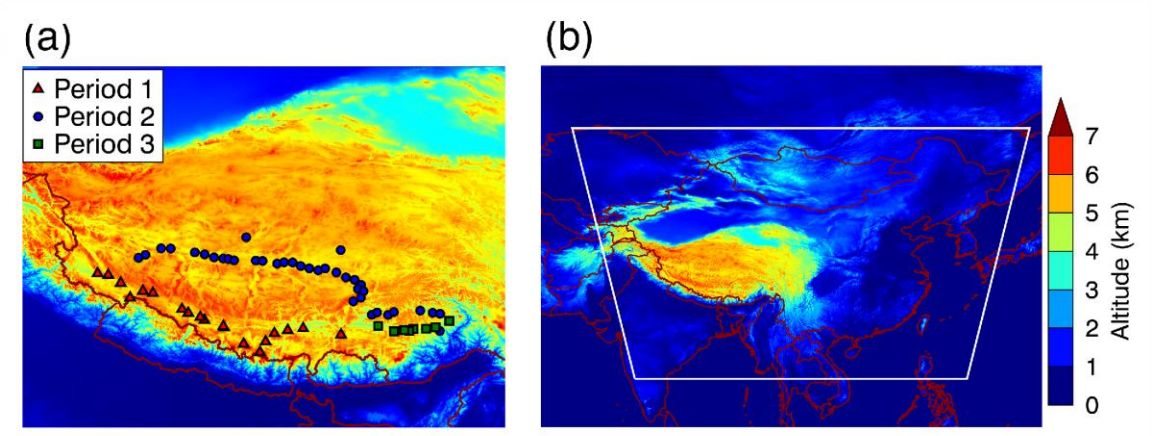

Figure 2.1 Overview of regions involved in this study. Locations of observations for Period 1 (October 13-17, 2010, triangle), Period 2 (October 19-24, 2010, circle) and Period 3 (October 25, 2010, square) are shown in (a). White polygon in (b) represents the model domain margin of REAM. Altitude data from Geological Survey Global 30 Arc-Second Elevation (GTOPO30, courtesy of the U.S. Geological Survey) is shown as colored background.

2.2.2 SCIAMACHY CHOCHO Measurements

The SCIAMACHY onboard ENVISAT operated from 2002 to 2012 (Burrows et al., 1995; Bovensmann et al., 1999), with an overpass time at about 10:00 AM LT. SCIAMACHY made passive remote sensing measurements of the upwelling radiation from the top of the atmosphere in alternate nadir and limb viewing geometry. Mathematical inversion of the measurements of SCIAMACHY yields a variety of data products including CHOCHO VCDs (unit: molecules cm^{-2}). The retrieval uses the DOAS technique (Wittrock et al., 2006; Vrekoussis et al., 2009; Alvarado et al., 2014). The CHOCHO retrieval used in this study is based on the algorithm developed in Alvarado et al. (2014), which includes corrections for the interferences with NO_2 over the regions with high NOx emissions as well as liquid water over oceans (Alvarado, 2016). Detection limit for SCIAMACHY CHOCHO VCD is about 1×10^{14} molecules cm^{-2}. The overall monthly uncertainty of CHOCHO VCDs ($C_{CHOCHO}^{SCIAMACHY}$) in the selected region during October 2010 is given by $\alpha\times C_{CHOCHO}^{SCIAMACHY} + 1\times10^{14}\ molecules\ cm^{-2}$, where the value of α is in a range of 0.1 to 0.3. Following the method as described by Liu et al. (2012a), we derive a top-down aromatics emission estimate for South Asia constrained by CHOCHO retrievals described in Section 2.2.4.

2.2.3 3-D REAM Model

We use the 3-D REAM CTM to examine the chemistry evolution and regional transport of aromatics. As introduced in Section 1.2, REAM has a horizontal resolution of 36 km with 30 vertical levels in the troposphere and 5 vertical levels in the stratosphere

covering adjacent regions of China (Figure 2.1). Meteorological fields in REAM are obtained from WRF assimilations constrained by NCEP CFSR 6-hourly products. We run the WRF model with the same resolution as in REAM with a domain larger than that of REAM by 10 grid cells on each side. The recent update of REAM expands the GEOS-Chem standard chemical mechanism (V9-02) to include a detailed description of aromatics chemistry (Bey et al., 2001; Liu et al., 2010, 2012a). Aromatics are lumped into three species based on reactivity, i.e. ARO1 (toluene, ethyl-benzene), ARO2 (m/p/o-xylene), and benzene. The atmospheric lifetimes of the three aromatics tracers against OH are 18 hours, 4.2 hours and 3.9 days during the study period (October 13-25, 2010), respectively. Due to the long atmospheric lifetime of benzene, it is more difficult to track and identify its sources; thus we do not explicitly discuss benzene in this study. We focus our analysis on reactive aromatics (toluene, ethyl-benzene, and m/p/o-xylene).

Initial and boundary conditions for chemical tracers are taken from GEOS-Chem (V9-02) 2°×2.5° simulation (Bey et al., 2001). Anthropogenic emissions are from the MIX inventory for October 2010 (Li et al., 2015). MIX is a mosaic Asian anthropogenic emission inventory with the MEIC for China and several other emission inventories for other Asian countries. In addition to the MIX inventory, we also conduct sensitivity simulations using INTEX-b emissions inventory (Zhang et al., 2009; Li et al., 2014), which was developed for the year 2006. We find that compared to the in situ observations of aromatics, the simulation results using the INTEX-B emissions are better. The main reason for the simulation improvements is due to the emissions of aromatics in South Asia. Given the large uncertainties in the emissions of aromatics (e.g., Liu et al., 2012a), this result is

not surprising. Since MEIC and INTEX-B inventories are developed by the same group, we replace MIX aromatics emissions outside China with INTEX-B data such that aromatics emissions in the model are consistent. The improvements of model simulations compared to in situ observations are shown in Figure 2.2. Since satellite observations are used to improve aromatics emissions (2.2.4), using either MIX or INTEX-B emissions in this work gives the same conclusions. Biogenic VOC emissions are computed with the MEGAN algorithm (v2.1, Guenther et al., 2012) and outdoor biomass burning emissions of CHOCHO and other species are based on Global Fire Emissions Database Version 4.1 with small fires (GFED4.1s, van der Werf et al., 2010; Andreae and Merlet, 2001; Lerot et al., 2010). Indoor burning CHOCHO emissions of India are computed using emission factors from Pettersson et al. (2011) and Li et al. (2014). Rural and urban population distributions of India for year 2010 are used as spatial proxies (Balk et al., 2006; CIESIN, 2011, 2016). We adopt the energy consumptions for rural and urban inhabitants on the basis of the National Sample Survey Office of India (N.S.S.O., 2012a, 2012b). Compared with satellite observed CO and NO2 VCDs, REAM performs reasonably well in the study region during October 2010 (Figure 2.3). For general model evaluations of REAM, we refer the readers to the papers cited early in this section.

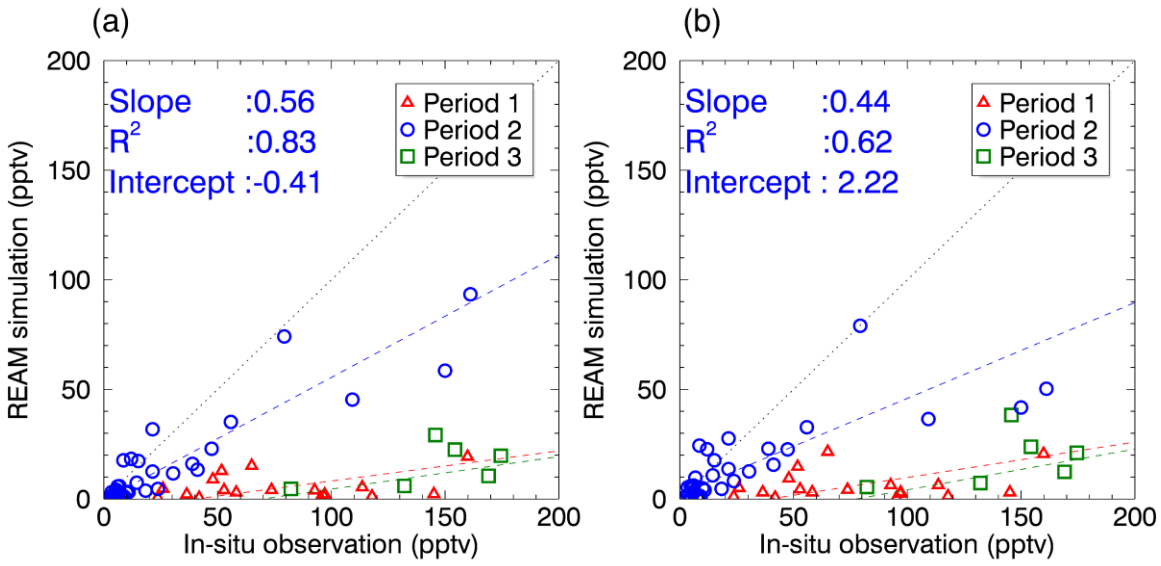

Figure 2.2 Comparisons between REAM simulated and in-situ observed reactive aromatics concentrations with (a) and without (b) INTEX-B aromatics emissions for countries excluding China.

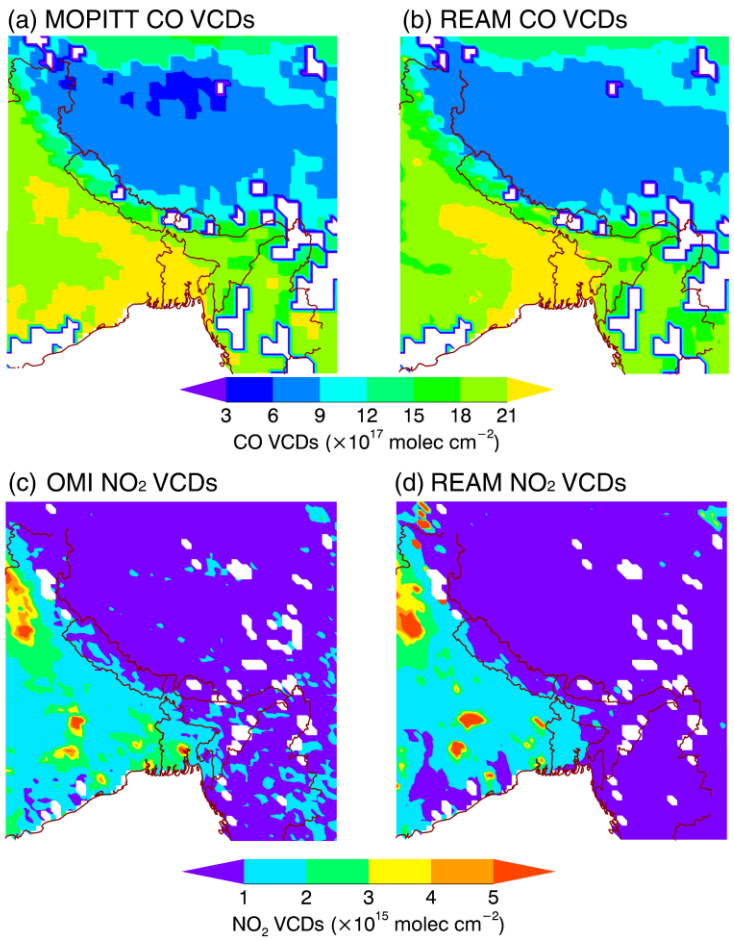

Figure 2.3 MOPITT retrieved (a) and REAM simulated (b) monthly averaged total CO VCDs during October 2010. OMI retrieved (c) and REAM simulated (d) monthly averaged tropospheric NO_2 VCDs during October 2010. White areas denote missing data. MOPITT data are from http://www.acom.ucar.edu/mopitt/MOPITT/. OMI data are from http://www.temis.nl/airpollution/no2col/. Averaging kernels are applied to the model results.

We updated the INTEX-B emission inventory in South Asian countries through inverse modeling constrained by SCIAMACHY CHOCHO VCDs (next section). We run REAM simulations with the a priori and top-down emission inventories, and compare the results with observations in Section 2.3.1 and 2.3.2, respectively. We find that some of the

model low bias is likely due to emission underestimation. We further carried out three model sensitivity tests to calculate the contributions to surface aromatics from emissions over Tibet, other provinces of China, and South Asia (India and nearby regions). Each simulation is run with only the aromatics emissions from the corresponding region. The OH concentrations in each simulation are specified to the archived values of the full model simulation. The results for two sub-periods of Period 2 are examined in Section 2.3.3.

2.2.4 Top-down Aromatics Emission Estimation

Compared with SCIAMACHY data, REAM using the original emission inventories archived at the overpass time of SCIAMACHY underestimates CHOCHO VCDs in the populated regions of India (Figure 2.4). This underestimation is especially significant in the Indo-Gangetic Plain located south of the Himalayas (Figure 2.4c). We then derive the top-down aromatics emissions for these regions constrained by SCIAMACHY CHOCHO data (Liu et al., 2012a; Alvarado, 2016).

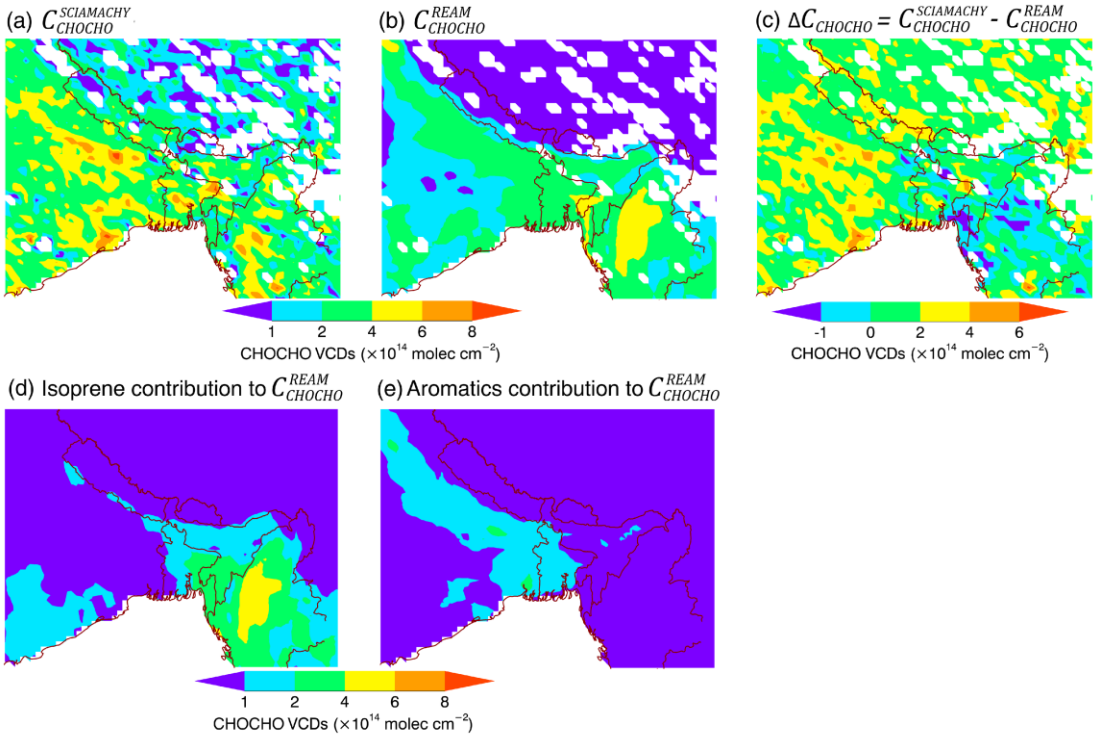

Figure 2.4 SCIAMACHY observed CHOCHO VCDs (a), REAM simulated (b) CHOCHO VCDs, the low bias of simulated CHOCHO VCDs (c), simulated isoprene (d) and aromatics (e) contributions to CHOCHO VCDs using the a priori emissions for October 2010. White areas denote missing satellite data or ocean. For each valid SCIAMACHY data point, a corresponding model value is sampled in (b) and (c).

First, we calculate the difference between observed ($C_{CHOCHO}^{SCIAMACHY}$, Figure 2.4a) and modeled (C_{CHOCHO}^{REAM}, Figure 2.4b) CHOCHO VCDs with original emissions ($\Delta C_{CHOCHO} = C_{CHOCHO}^{SCIAMACHY} - C_{CHOCHO}^{REAM}$, Figure 2.4c). This discrepancy greatly exceeds the uncertainties of SCIAMACHY retrieval. We then discuss the potential reasons for the difference, i.e. primary emissions from biomass burning and secondary sources from isoprene, acetylene, ethylene and aromatics (Fu et al., 2008; Liu et al., 2012a).

Biomass burning is often a major primary source of CHOCHO (Myriokefalitakis et al., 2008). GFED4.1s inventories, as well as fire hotspots observed by MODIS on board the Terra and Aqua satellites, indicate only a small number of fire occurrences during this period in South Asia, with the exception of crop residue burning in Punjab, an agricultural state in North India. The contribution to CHOCHO VCDs from outdoor biomass burning (Figure 2.5a) differs greatly from that of ΔC_{CHOCHO} (Figure 2.4c), which is large over the industrialized Indo-Gangetic Plain. Simulated indoor burning contribution to CHOCHO VCDs is lower by a factor of about 15 than the CHOCHO VCDs discrepancy between satellite retrieval and model simulation (Figure 2.5b). The uncertainty of the indoor burning CHOCHO emissions mainly results from that of the emission factor. Even we assume this uncertainty to be 300%, indoor burning cannot explain the low bias of the simulated CHOCHO VCDs. Therefore, the large model underestimation of CHOCHO over the Indo-Gangetic Plain is unlikely due to outdoor biomass burning or indoor burning during our analysis period.

Direct anthropogenic emissions of CHOCHO are small (Volkamer et al., 2005; Stavrakou et al., 2009; Liu et al., 2012a). CHOCHO is produced primarily from the photochemical oxidation of biogenic compounds (e.g., isoprene and terpenes) and hydrocarbon released by anthropogenic activities (e.g., acetylene, ethylene, and aromatics) (Fu et al., 2008). Due to the long atmospheric lifetime of acetylene and ethylene, their contributions to CHOCHO concentrations are quite small in South Asia during October 2010. The most significant secondary sources of CHOCHO in South Asia are isoprene (Figure 2.4d) and aromatics (Figure 2.4e). Biogenic isoprene emissions depend on

vegetation, sunlight, and temperature. The high isoprene contribution to CHOCHO VCDs is to the southeast of the Indo-Gangetic Plain, where CHOCHO VCDs are high in both the observations and model simulations. In comparison, aromatics oxidation dominates CHOCHO over the Indo-Gangetic Plain, where model underestimation is largest (Figure 2.4).

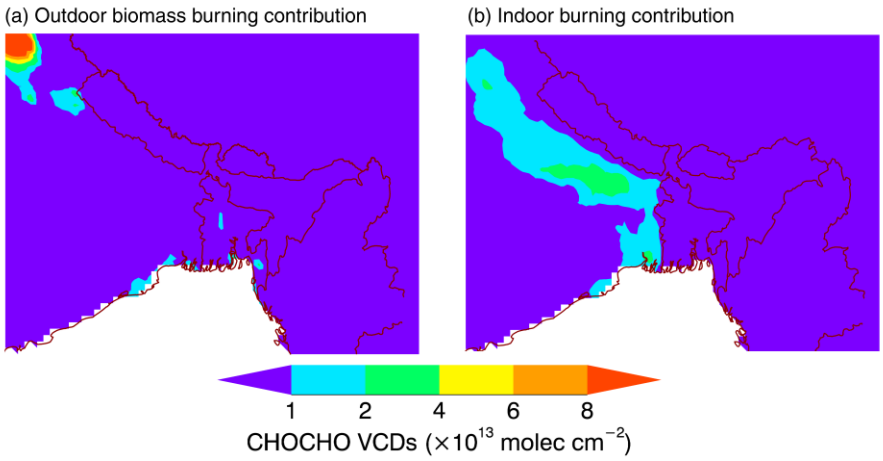

Figure 2.5 Contributions to CHOCHO VCDs from outdoor biomass burning (a) and indoor burning (b) emissions for October 2010.

We apply the approach by Liu et al. (2012b) to estimate the top-down emissions of aromatics based on SCIAMACHY CHOCHO VCDs. As found by Liu et al. (2012b), domain-wide inversion is impractical since model results correlate poorly with gridded satellite data, most likely reflecting the problems in the spatial distribution of a priori emissions. We therefore determine the emissions by inversion for each grid cell at the overpass time of SCIAMACHY as Liu et al. (2012a) and find similar results for India and nearby regions as Liu et al. (2012a) did for eastern China. The top-down biogenic isoprene

emissions are essentially the same as the a priori emissions. However, the top-down anthropogenic emissions of aromatics (Figure 2.6) increase by a factor of 2-6. The improved model comparison with in situ observations will be discussed in the next section. One caveat with respect to the top-down emission estimate is that we have to assume that the speciation of aromatics in the a priori emission inventory is correct. Since the purpose of this work is to study transport pathways to the Tibetan Plateau on the basis of in situ observations, we examine lumped reactive aromatics (defined as the sum of toluene, ethyl-benzene, and m/p/o-xylene) in the model evaluation (Section 2.3.2). Satellite observations cannot be used for this purpose since CHOCHO VCDs over Tibet are below or around the detection limit.

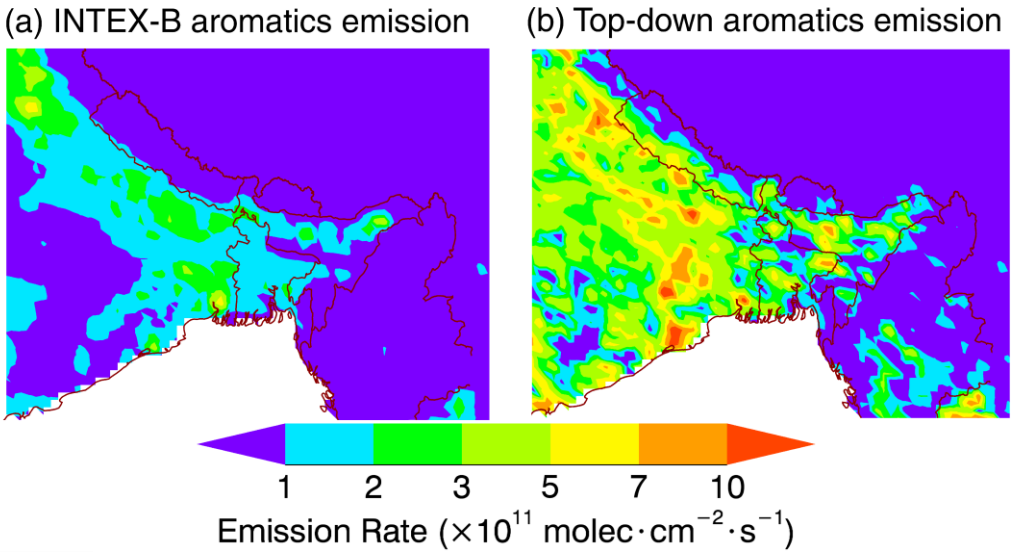

Figure 2.6 INTEX-B aromatics emissions (a) and top-down aromatics emissions (b).

2.3 Results and discussion

2.3.1 Observed and Simulated Reactive Aromatics

The average of observed reactive aromatics surface concentration (59±63 pptv) over the Tibetan Plateau is considerably lower than the values found for megacities of China, such as Beijing (8.04 ppbv) and Shanghai (5.2 ppbv) (Liu et al., 2012a). Higher aromatics levels were measured during Period 1 (76±39 pptv) and Period 3 (169±57 pptv) than in Period 2 (26±39 pptv). The model simulation using the a priori emissions in general compares poorly with the in situ observations (Figure 2.7). The best performance is during the low-concentration Period 2 when the model underestimates the observations by about a factor of 2. However, the relatively high correlation coefficient (R^2=0.83) suggests that atmospheric transport and emission distribution are reasonably simulated. This is in sharp contrast to Periods 1 and 3 when the model underestimates the observations by a factor of 7 with very low correlations between the model and the observations (slope=0.14 and 0.15, R^2=0.04 and 0.02 for Period 1 and 3, respectively). We discuss the different reasons for the model performance for Period 1, 2 and 3 in the next 3 sections.

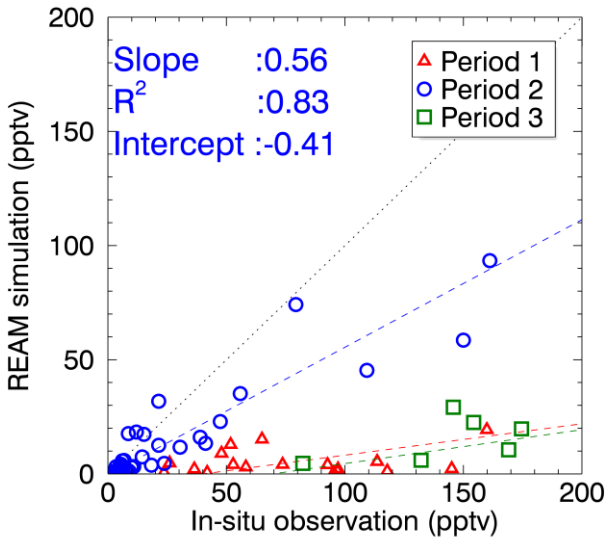

Figure 2.7 Comparison between REAM simulated reactive aromatics concentrations (Y-axis) and in situ observations (X-axis). REAM results are archived corresponding to the time and location of the observations. Linear regression results for three periods are shown in red (slope=0.14, R^2=0.04), blue (slope=0.56, R^2=0.83), and green (slope=0.15, R^2=0.02) dashed lines, respectively.

2.3.2 Improvements due to Top-down Emissions

Figure 2.4 and Figure 2.6 show that SCIAMACHY observations of CHOCHO suggest much higher industrial emissions of aromatics over the Indo-Gangetic Plain than the a priori emissions. We derive top-down emissions on the basis of SCIAMACHY CHOCHO VCDs (Section 2.2.4). Top-down emissions are higher than the a priori emissions by a factor of 2-6 over the Indo-Gangetic Plain, which is the upwind region of the Tibetan Plateau. Figure 2.8 shows the resulting improvement in the model simulation. The large underestimations of CHOCHO VCDs over the Indo-Gangetic Plain are corrected

as expected (Figure 2.8a). At the same time, in situ observations during Period 2 are much better reproduced by the model with the slope increasing from 0.56 to 0.91 and a similar R^2 value (0.66) (Figure 2.8b). In contrast, model simulations for Periods 1 and 3 are not improved using top-down emission estimates with low biases similar to the original model simulation. This indicates that the reasons for the discrepancies in Periods 1 and 3 are probably not related to the uncertainties in emissions but could be linked to deficiencies in model transport in this area.

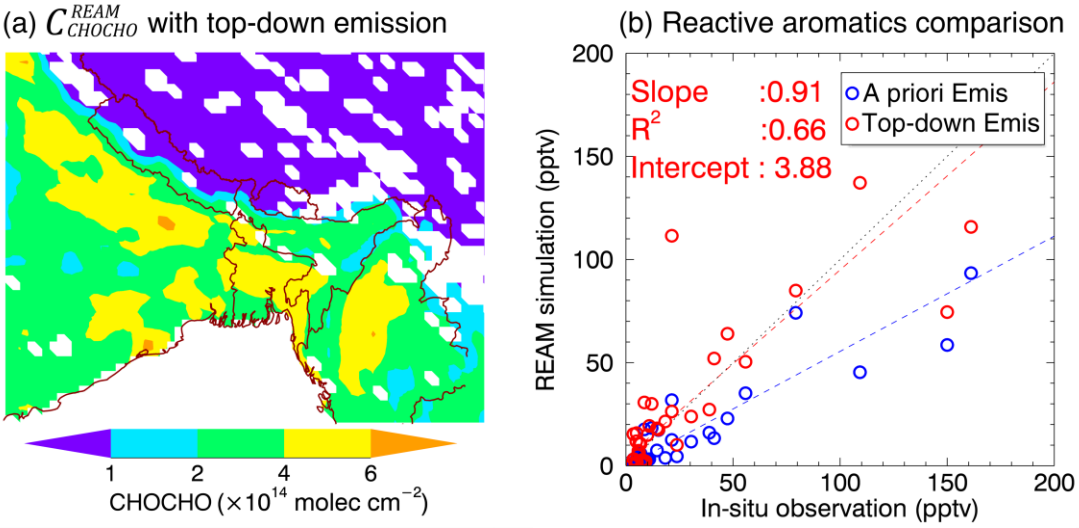

Figure 2.8 REAM simulated CHOCHO VCDs with top-down emissions (a) and comparison of simulated and observed reactive aromatics concentrations during Period 2 (b). Blue and black circles in panel (b) represent REAM simulation with a priori (slope=0.56, R^2=0.83) and with top-down (slope=0.91, R^2=0.66) emissions, respectively.

2.3.3 Rapid trans-Himalaya Transport due to a High-level Cut-off Low System

Observed and simulated reactive aromatics concentrations show large variabilities during Period 2 (Figure 2.8b). An investigation of these data shows that a major contributor is meteorology. Observed concentrations of reactive aromatics during October 19-20 are generally lower (6.6±3.4 pptv), in comparison to those during October 21-24 (37±45 pptv). The concentration difference during the two periods is captured by model simulations with top-down emissions (Figure 2.9). Analysis of WRF simulated surface wind speed shows an increase by a factor of 2-4 from October 19-20 (Figure 2.9a) to 21-24 (Figure 2.9b), corresponding well to increasing transport of aromatics from the Indo-Gangetic Plain.

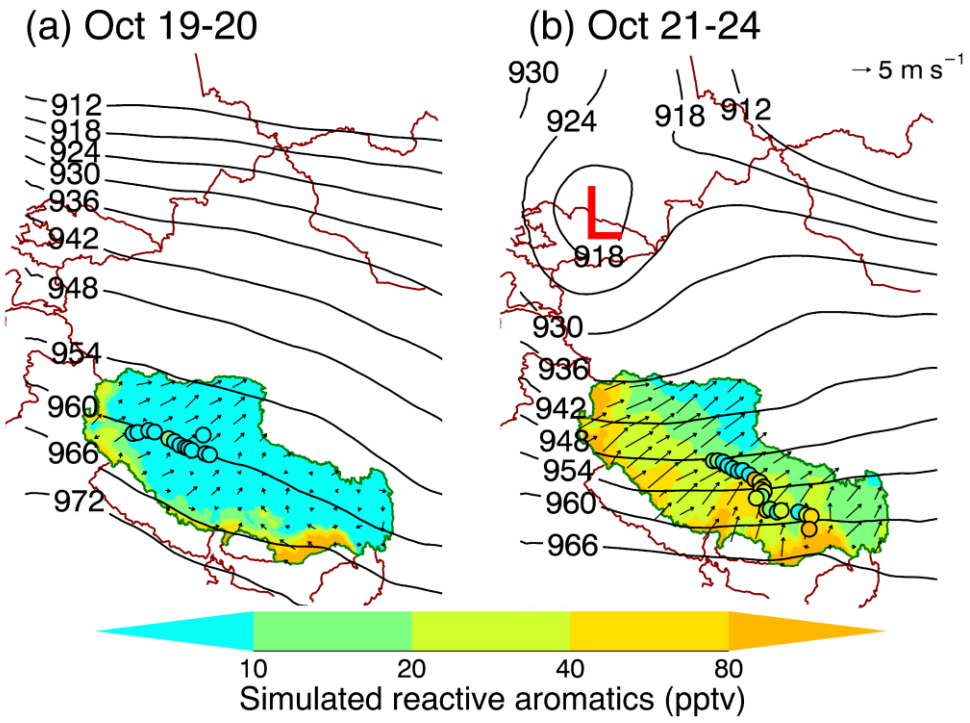

Figure 2.9 Distributions of WRF simulated surface wind and REAM simulated concentrations of reactive aromatics over the Tibetan Plateau during October 19-20, 2010 (a) and October 21-24, 2010 (b). Circles show the observed reactive aromatics

concentrations. Composite distributions of simulated reactive aromatics concentrations and surface wind over Tibet, corresponding to sampling time of the observations, are shown in color and by arrows, respectively. Corresponding WRF simulated 300 hPa geopotential height fields are shown by contour lines. The border of Tibet Autonomous Region is colored green.

To further analyze the difference between the two periods, we conduct sensitivity simulations as described in Section 2.2.3. We compute the source attributions for emissions over Tibet, India and nearby regions, and China excluding Tibet (Figure 2.10). During October 19-20, reactive aromatics are due to Tibetan emissions. With the exception of one data point, the concentrations are $\leqslant$ 7 pptv. On October 21, emissions from India and nearby regions become dominant while the concentrations are still low (7-21 pptv). During October 22-24, however, emissions from India and nearby regions contribute much higher concentrations (10−137 pptv). The only exception is one data point sampled at 30 km east of Lhasa, where about one fifth of the population of Tibet resides. The contribution by emissions of India and nearby regions to this data point is ~20 pptv, still much higher than during October 19-20. The contribution by emissions from China (excluding Tibet) is negligible (~1%) for this period.

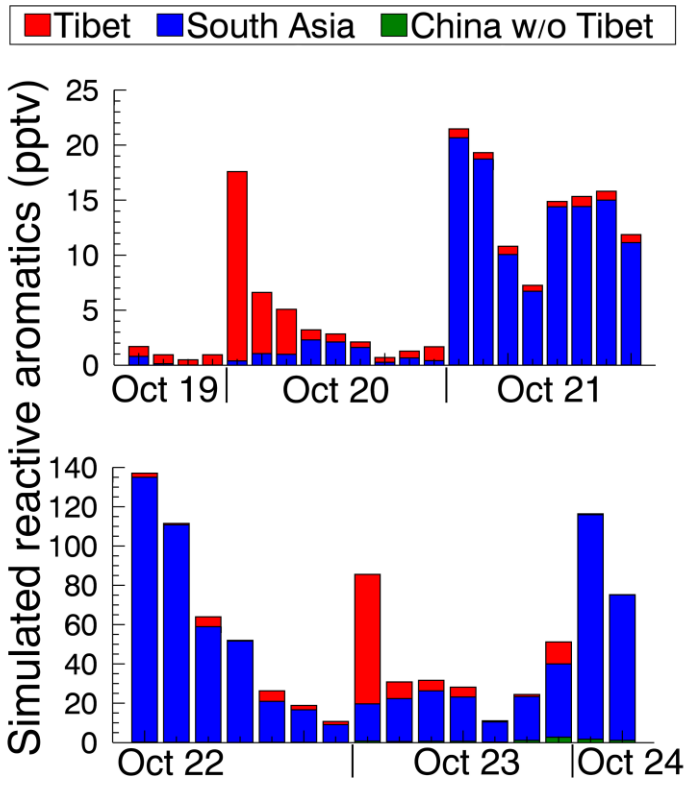

Figure 2.10 Reactive aromatics emitted from Tibet (red), India and nearby regions ("South Asia", blue) and China excluding Tibet ('China w/o Tibet', green) corresponding to the in situ observations in the REAM simulation with top-down emissions. Contributions from the other regions are negligible.

The rise of the Tibetan Plateau is a natural barrier for pollution transport (Figure 2.1). Considering the high altitude of the Tibetan Plateau, we analyze 300 hPa geopotential height field in order to understand the change of wind circulation over the region (Figure 2.9). During October 19-20, the upper troposphere shows a northward gradual pressure decrease, which does not promote near-surface forcing of trans-Himalaya transport (Figure 2.9a). During October 21-24, the presence of a southeastward-moving upper tropospheric

cut-off low system induces increasingly stronger surface wind from India to Tibet (Figure 2.9b, Hoskins et al., 1985). The cut-off low system is a closed low-pressure system detached from the westerlies. It began to form on October 21 and started to dissipate on October 24. Trans-Himalaya air mass flux in the lower atmosphere shows an increase by a factor of 2 to 5 (Figure 2.11). Accompanying this transport, large amounts of pollutants such as reactive aromatics analyzed here are transported to the Tibetan Plateau leading to much higher surface concentrations.

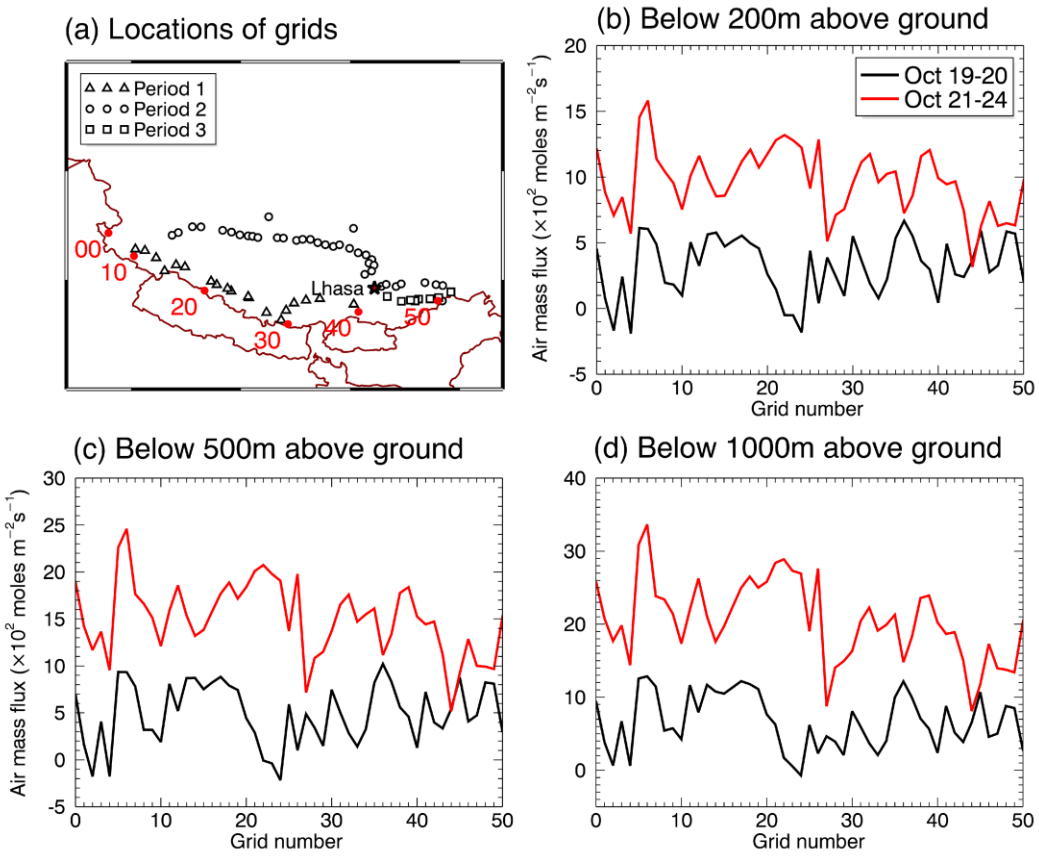

Figure 2.11 Trans-Himalaya air mass fluxes (positive towards Tibet) during October 19-20 (black line) and October 21-24 (red line) in the lower atmosphere below 200m (b), 500m (c) and 1000m (d). Red dots in panel (a) denote numbered grid cell locations for computed air mass fluxes; they are used as the x-axis in the other panels.

The cut-off low system provides a more rapid and efficient pollutants transport pathway compared with transport pathways previously proposed by other studies, such as westerlies (Cong et al., 2015; Ji et al., 2015) and mountain-valley winds (Hindman and Upadhyay 2002; Dumka et al., 2010). Compared to aromatics, BC is also subject to wet scavenging, which greatly reduces its transport efficiency by convection. In-cloud BC scavenging is due to cloud activation or ice nucleation and subsequent removal by precipitation, and below-cloud scavenging is due to collision with rain droplets (e.g., Taylor et al., 2014). During our analysis period, the cut-off low system and the associated precipitation are to the northwest of Tibet (Figure 2.12). Precipitation south of Tibet is weak and thus the subsequent removal of BC during trans-Himalaya transport is limited.

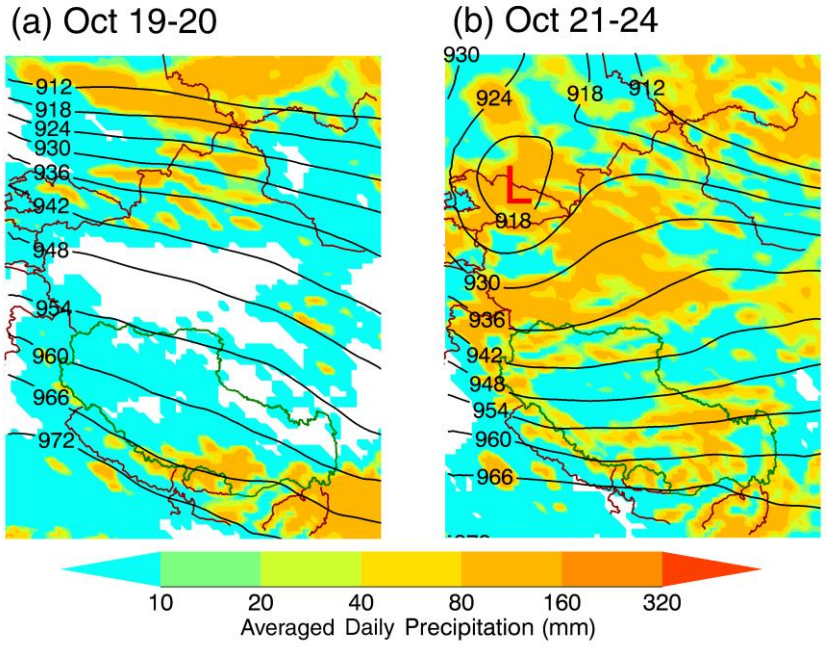

Figure 2.12 WRF simulated averaged daily precipitation for October 19-20 (a) and October 21-24 (b), respectively.

To examine the sensitivity of trans-Himalaya transport to the distribution of emission sources, we redistribute the INTEX-B total aromatics emissions over China and other South Asia countries on the basis of the MIX BC emission distributions. We conduct a sensitivity simulation using the redistributed emissions and compared the results to the original simulation. The trans-Himalaya transport from South Asia clearly dominates and it is strongly affected by the presence of a cut-off low system during our analysis period (Figure 2.13). Our analysis implies that BC transported in the presence of an upper tropospheric cut-off low is potentially a major contributor to BC deposition to Tibetan glaciers.

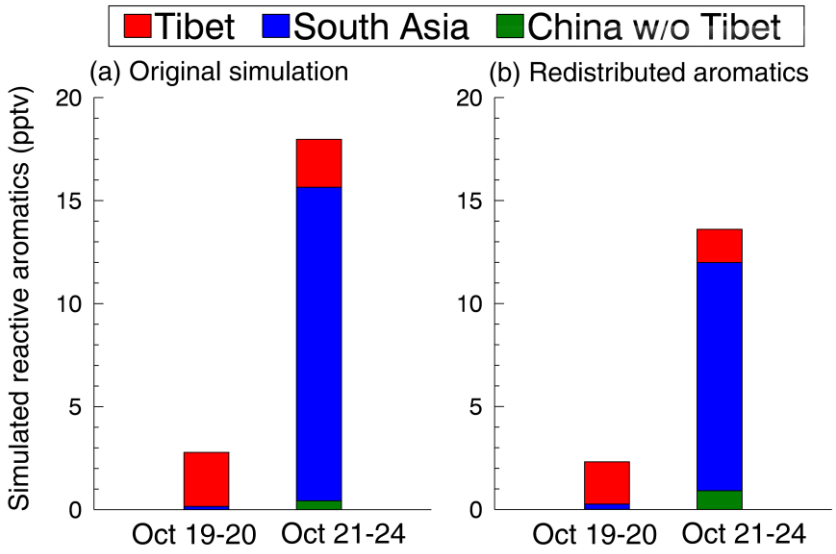

Figure 2.13 Averages of simulated reactive aromatics emitted from Tibet (red), India and nearby countries ("South Asia", blue) and China excluding Tibet ("China w/o Tibet", green) corresponding to in situ observations during October 19-20 and October 21-24. REAM simulations are conducted with original emissions (a) and the aromatics emissions redistributed following the BC emission distribution (b), respectively.

2.3.4 Missing Cut-off Low System and Complex Terrain

Compared to Period 2, model performance for Periods 1 and 3 is very poor with severe low biases (Figure 2.7). Transport deficiency appears to be the main problem. Figure 2.14 shows the histograms of observed and simulated surface wind speed for the 3 periods. The observed and simulated wind speed distributions are similar for Period 2 (Figure 2.14c). In comparison, the simulated wind speed distribution differs drastically for the other two periods (Figure 2.14a and Figure 2.14d).

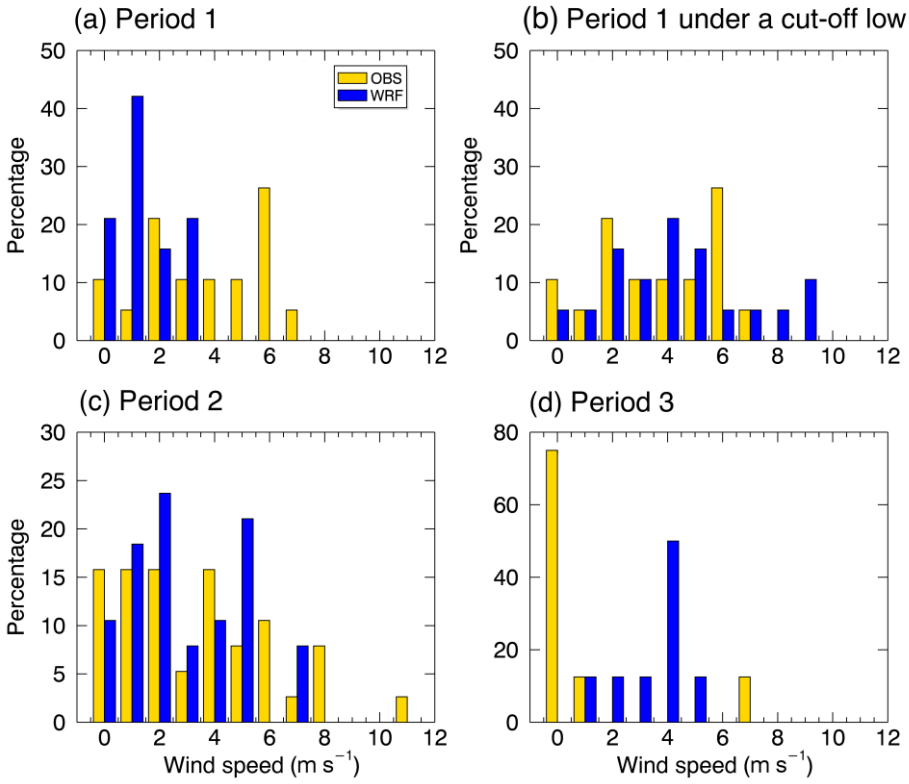

Figure 2.14 Histograms of observed and simulated surface wind speed for Period 1 (a), Period 2 (c) and Period 3 (d). Panel (b) shows the wind histogram of October 23 with an upper tropospheric cut-off low system. Model results are sampled at the same time and location as the observations. In Panel (d), the date information is not used. Wind speed is binned at 1 m/s interval.

The wind speed distributions are more similar between Period 1 and 2 in the observations than model simulations. The underestimation of wind speed in Period 1 leads to slower transport of pollutants from the Indo-Gangetic Plain and consequently to a low bias in surface reactive aromatics in the model. Examination of the 300 hPa geopotential height field during October 13-17 of Period 1 shows a weak trough northeast of Kazakhstan in CSFR reanalysis and WRF simulation results (Figure 2.15). A strong upper tropospheric low pressure system, akin to the cut-off low system of Figure 2.9b, will induce stronger lower troposphere wind circulation. The lack of radiosonde observations over the interior of the Tibetan Plateau to constrain the meteorological reanalysis is the plausible reason (Figure 2.16). The horizontal scale of the Rossby Wave at northern mid latitudes is thousands of kilometers, which can be reasonably represented by the density of the existing radiosonde network. We hypothesize that the smaller scale cut-off low system, not simulated in the reanalysis, is more likely the reason for the model-observation discrepancy during Period 1. We resample surface wind speed of October 23, when a cut-off low system leads to rapid trans-Himalaya transport in Period 2 analyzed in the previous section. At the same time of the day and location as the observations, the simulated wind speed histogram is in good agreement with the observations (Figure 2.14b). The corresponding air mass flux across the Himalayas would have been much stronger in the presence of a cut-off low system (Figure 2.17).

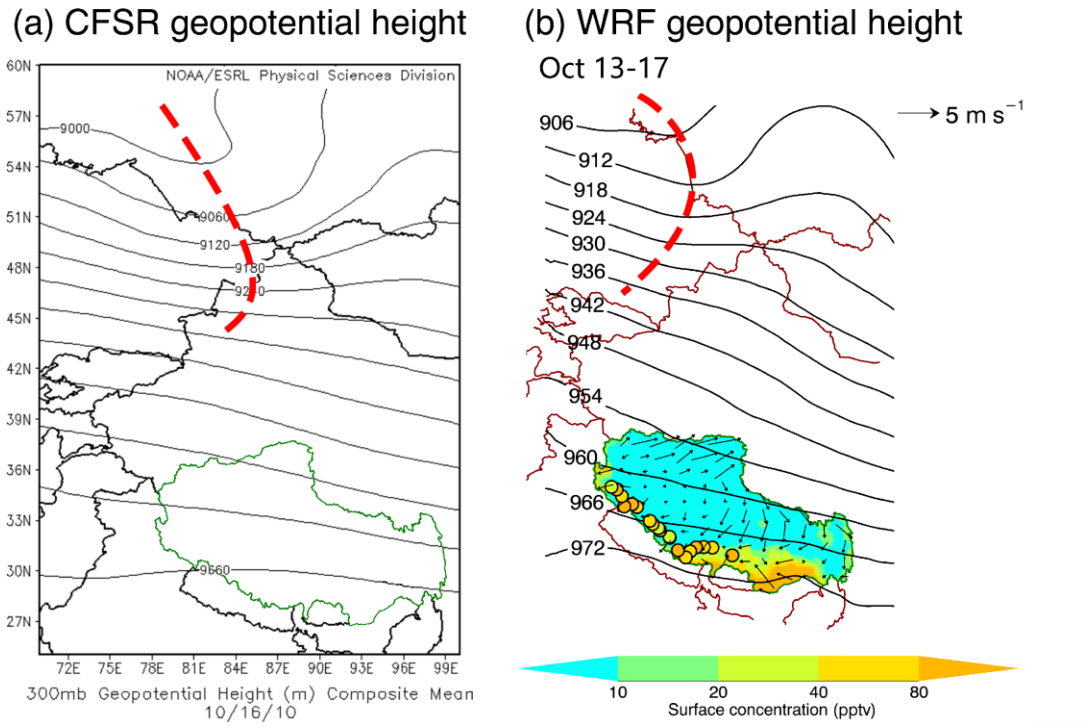

Figure 2.15 (a) CFSR reanalysis geopotential height at 300hpa on October 16, 2010 (available at http://www.esrl.noaa.gov/psd). (b) Same as Figure 5 for Period 1 (October 13-17). Red dashed line represents the trough in 300 hPa.

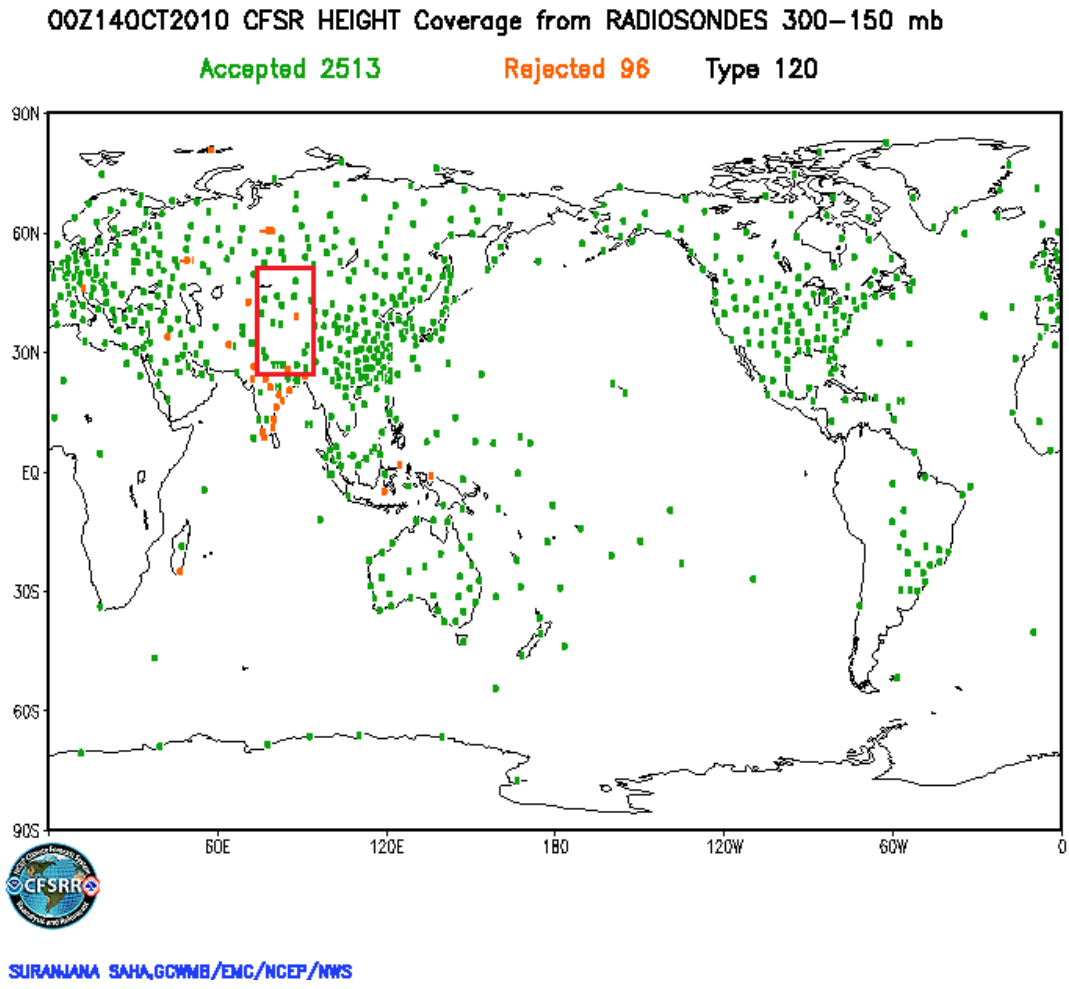

Figure 2.16 CFSR 300-150hPa observation coverage (http://cfs.ncep.noaa.gov) on October 14, 2010. The red frame indicates the domain of Figure 2.9 and Figure 2.15.

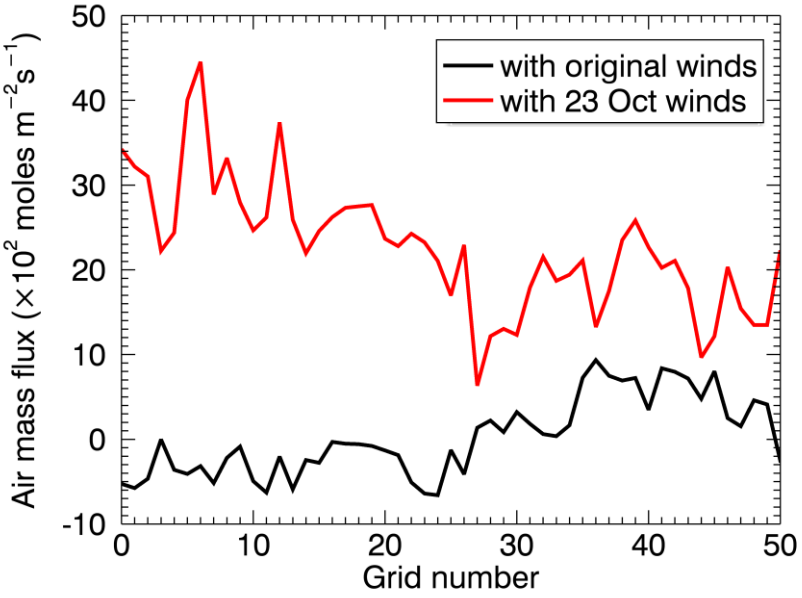

Figure 2.17 Same as Figure 2.11 but for ground-1 km air mass fluxes of Period 1 and on October 23 under a cut-off low system, colored as black and red respectively.

During Period 3, the observed wind speed histogram is skewed to very low wind speed (0-1 m/s) compared to the simulations (Figure 2.14d). Sampling bias to avoid locations with strong wind is a possible reason. Another reason is that these samples were taken at lower altitudes in valleys compared to higher altitudes in the other two periods. Inspection of Figure 2.1 shows the complex terrain surrounding the valleys of Period 3 sampling. Using high-resolution (~ 1 km) terrain data from the GTOPO30 dataset, we find that the standard deviation of altitude in the $7km \times 7km$ region centered at the corresponding observation location correlates well with the observed reactive aromatics with a R^2 value of 0.55 (Figure 2.18), which suggests that pollution transport is strongly

enhanced by the effects of complex terrain. The horizontal resolution of 36 km used in this study is inadequate to simulate this effect. Model resolution as high as 1 km appears to be necessary to capture the observed feature but the computational resource requirement will be exceptionally large for a global model such as that used for CFSR. Other issues related to complex terrains in this region were also discussed by previous studies (Maussion et al., 2011; Ménégoz et al., 2013; He et al., 2014; Kumar et al., 2015). The effects of complex terrain may have also affected the observations of Periods 1 and 2 but to a smaller extent since the terrain variation is lower and sampling altitude is higher in those periods.

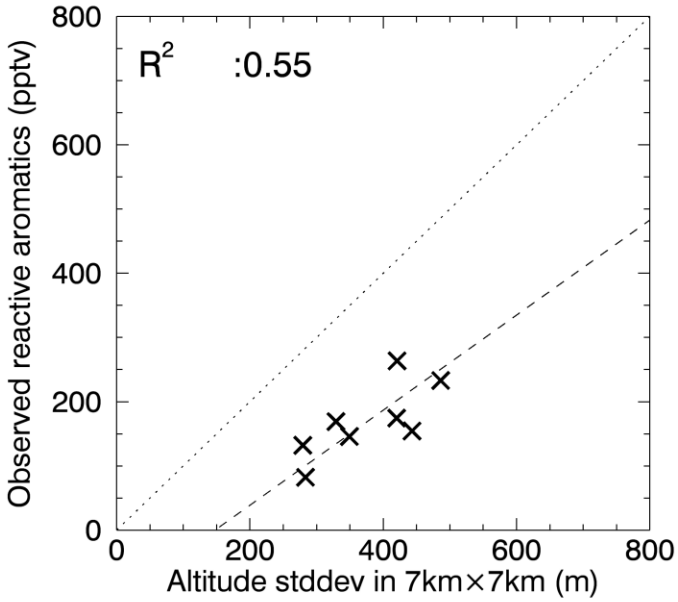

Figure 2.18 Observed reactive aromatics as a function of terrain complex during Period 3. The latter is computed as the standard deviation of altitude in a 7km x 7km region centered at the sampling location. The dash line denotes a least-squares regression.

2.4 Conclusions and Implications for Climate Studies

We apply the REAM model to analyze in situ observations of reactive aromatics across the Tibetan Plateau. Top-down estimate using SCIAMACHY CHOCHO observations suggests that the a priori inventory for aromatics emissions is low by a factor of 2 to 6 over the industrialized Indo-Gangetic Plain. Application of the top-down emission estimate greatly reduces the low bias of the model during Period 2. Model results suggest that the second half of Period 2 is characterized by rapid trans-Himalaya transport from India and nearby regions driven by the presence of a cut-off low system in the upper troposphere.

Model performance for Periods 1 and 3 is poor compared to Period 2 and employing top-down emission estimates does not significantly improve the model simulation of these periods. In situ observations show much stronger surface wind than simulated in the model during Period 1. The lack of radiosonde observations in the interior of the Tibetan Plateau is likely the reason that a cut-off low system, the scale of which is much less than the mid-latitude Rossby wave, is not simulated by the T382 (~38 km) CSFR reanalysis. Consequently, trans-Himalaya transport is greatly underestimated in the model. Sampling of Period 3 is in valleys surrounded by complex terrain. Although observed surface wind is weak, we find that reactive aromatics concentrations are strongly correlated with the complexity of surrounding terrain, implying enhanced pollution transport by terrain driven mixing. Model simulations at a resolution of 36 km are inadequate for simulating the terrain effect.

The height of the Tibetan Plateau is a natural barrier for pollution transport into this pristine region. This geographical feature is also a challenge for regional and global model

simulations. In this study, we use short-lived reactive aromatics as proxies to evaluate model simulated transport to the Tibetan Plateau on the basis of in situ observations. After correcting for the emission underestimation using satellite observations, simulated trans-Himalaya transport of proxy species (using WRF assimilated meteorological fields) still has significant low biases for two reasons, (1) poor representation of a cut-off low system, and (2) inadequate representation of terrain effect due to a coarse model resolution. These two transport-related issues likely exist in global climate models; the coarser resolution of climate models than our simulations or CSFR may further worsen the transport biases. Our results imply that pollution transport to the Tibetan Plateau, such as that of BC, is likely to be greatly underestimated in climate models, which was found previously (e.g., He et al., 2014). In addition to trans-Himalaya transport, BC emissions, chemical transformation, and wet deposition also require extensive evaluations with the observations over the region. Further analysis of reanalysis and climate model simulations is required to quantify potential model biases and the resulting effect of simulated BC deposition to glaciers on the Tibetan Plateau due to the transport issues we identified in this study.

CHAPTER 3. NOX EMISSION CHANGES DUE TO URBANIZATION AND POWERPLANT DENITRIFICATION IN YANGTZE RIVER REGION[2]

3.1 Introduction

Atmospheric NOx is notorious for the adverse health effects and for serving as precursors to other atmospheric pollutants (Zhao and Wang, 2009; Lin et al., 2010, 2013; Yang et al., 2011; Gu et al., 2013, 2016; Zhang et al., 2016), such as ozone (O_3) and particulate matters (PMs). The primary anthropogenic NOx source is fossil fuel combustion, of which the high temperature leads to NO formation from nitrogen and oxygen. Consequently, NOx hotspots mostly coincident with vehicle populated cities and industrialized regions in China where coal-fired powerplants are located (Gu et al., 2013; Liu et al., 2017). Due to the rapid economic development, air quality in China deteriorated severely (Lin et al., 2013; Zou et al., 2017). China has carried out several regulations to reduce NOx emissions, such as vehicle emission control (Liu et al., 2016) and the application of Selective Catalytic Reduction (SCR) or Selective Non-Catalytic Reduction (SNCR) in coal-fired powerplants (Gu et al., 2013; Tian et al., 2013). The bottom-up emission estimation approaches are commonly used to quantify the emission changes and

[2] This chapter is an extension of "NOx emission changes due to urbanization and powerplant denitrification in Yangtze River region", to be submitted to Environmental Science & Technology. The co-authors are Ruixiong Zhang, Yuhang Wang, Charles Smeltzer, Jianfeng Li, Yongjia Song, and Hang Qu.

regulation effectiveness. However, for lack of sufficient statistics and reliable emission factor measurements, the bottom-up approach in developing regions is challenging (Streets et al., 2013). Benefit from the global coverage and high spatial resolution, satellite NO_2 retrievals have been extensively applied in NO_2 emission estimations (Martin et al., 2003; Zhao and Wang, 2009; Lin et al., 2010, 2011, 2012; Beirle et al., 2011; Gu et al., 2013, 2014, 2016; Liu et al., 2017; Mijling et al., 2012, 2013; Ding et al., 2017) and evaluation of emission control effectiveness (Yang et al., 2011; Gu et al., 2013). Emission inversions using satellite retrievals compensate bottom-up emission inventories for data availability in developing regions.

Martin et al. (2003) used a CTM to derive monthly NOx emissions from satellite NO_2 retrieval. Based on this monthly inversion technique, Zhao et al. (2009) developed a Daily Inversion (DI) method which iteratively updates NOx emissions on a daily other than monthly basis. The DI method implicitly accounts for the chemical non-linearity (Gu et al., 2014). Gu et al. (2014) further coupled simultaneous retrieval with inversion (Daily Retrieval-Inversion, DRI). However, the inverse emission inventories in previous researches lack spatial resolution to study the detailed emission changes, such as urbanization. The High-resolution Daily Retrieval-Inversion (HDRI) developed in this study optimizes the DRI method for high resolution inversion. The spatial resolution of inverse emission improves significantly from 70km×70km to 4km×4km. We derive HDRI NOx emissions in Yangtze River region from OMI NO_2 retrieval during June-July-August (JJA) 2005-2015. We illustrate the effect of urbanization on NO_2 emission change. Also, we discuss on the powerplant emission changes between 2005-2009 and 2010-2015 due to

the application of deNOx systems. The HDRI method will be even more crucial in understanding NOx emission distribution with the launch of TROPOMI (Veefkind et al., 2012). TROPOMI provides 7km×7km resolution at nadir, which succeeds its predecessors by large.

3.2 Methods

3.2.1 3-D REAM Model

We use the 3-D REAM CTM (Section 1.2) in retrieving tropospheric NO_2 VCDs from OMI and NOx emission inversion. REAM features a spatial resolution of 4km×4km, 30 vertical layers in the troposphere and 5 vertical layers in the stratosphere. Figure 3.1 illustrates the model domain in this research. The meteorology fields are assimilated by WRF, which is constrained by NCEP CFSR 6-hourly products (Saha et al., 2010). The initial and boundary condition of chemical tracers are constrained by REAM simulation covering East Asia at a spatial resolution of 36km×36km, the latter is further constrained by the global GEOS-Chem simulation (Bey et al., 2001). The operator splitting timestep between chemistry and transport is 15 minutes. Anthropogenic emissions of NOx, CO and VOCs are from MEIC emission inventory (http://meicmodel.org/), prepared for 2010 at 0.25°×0.25° spatial resolution. We follow the manner of Wang et al. (1998) to simulate soil NOx emissions, and we parameterize lightning NOx as by Choi et al. (2005).

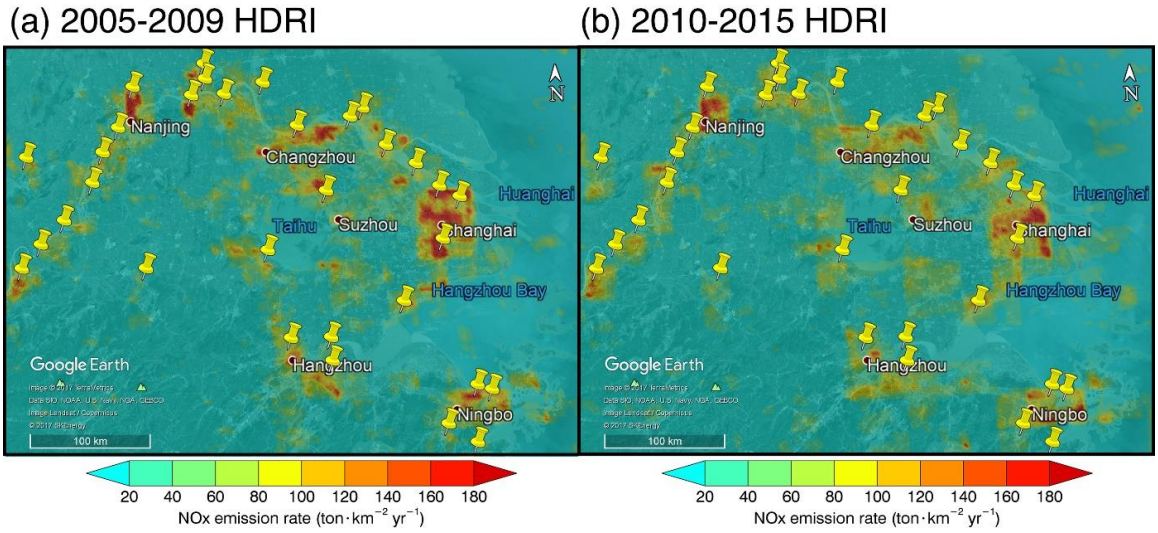

Figure 3.1 HDRI NOx emissions averaged during 2005-2009 (a) and 2010-2015 (b). Yellow pins illustrate the locations of powerplants visually coincident with emission hotspots.

Based on Gu et al. (2014) and Zhao and Wang (2009), High-resolution Daily Retrieval Inversion (HDRI) improves Daily Retrieval Inversion (DRI) with techniques optimized for high resolution satellite data. We use the OMI level-2 tropospheric NO_2 data during 2005-2015 JJA, when NOx lifetime is about several hours and the transport is less prevalent. For each OMI swath covering at least 10% of model domain, we calculate the retrieved tropospheric NO_2 VCDs (Section 3.2.2) and subsequently derive the a posteriori NOx emissions (Section 3.2.3), as depicted in Figure 3.2. Every day at 14:00 LT, we update the a priori NOx emissions used in REAM using the a posteriori NOx emissions from all available daily swaths, weighted inversely by the corresponding pixel sizes. To diminish the uncertainty of daily inversion, we turn back the model time by 30 hours and iteratively performed the daily retrieval-inversion three times for each day with the available OMI

data. The final a posteriori NOx emission is considered the HDRI NOx emission estimate of the day. In the HDRI method, we assume that the real emission varies each day, while the DRI method with more coarse resolution assumes that the emission is constant throughout the month (Zhao and Wang, 2009; Gu et al., 2013, 2014, 2016). The inversion error is then coupled with 50% day-to-day variance before moving forward to the next day. Figure 3.3 shows that the JJA averaged tropospheric NO_2 VCDs from REAM simulation and retrieval using HDRI emission. To ensure a fair comparison, the tropospheric NO_2 VCDs are sampled using OMI pixel geometry. The averaged regional discrepancies are 4-10%, implying that REAM can reasonably simulate tropospheric NO_2 VCDs with HDRI NOx emissions.

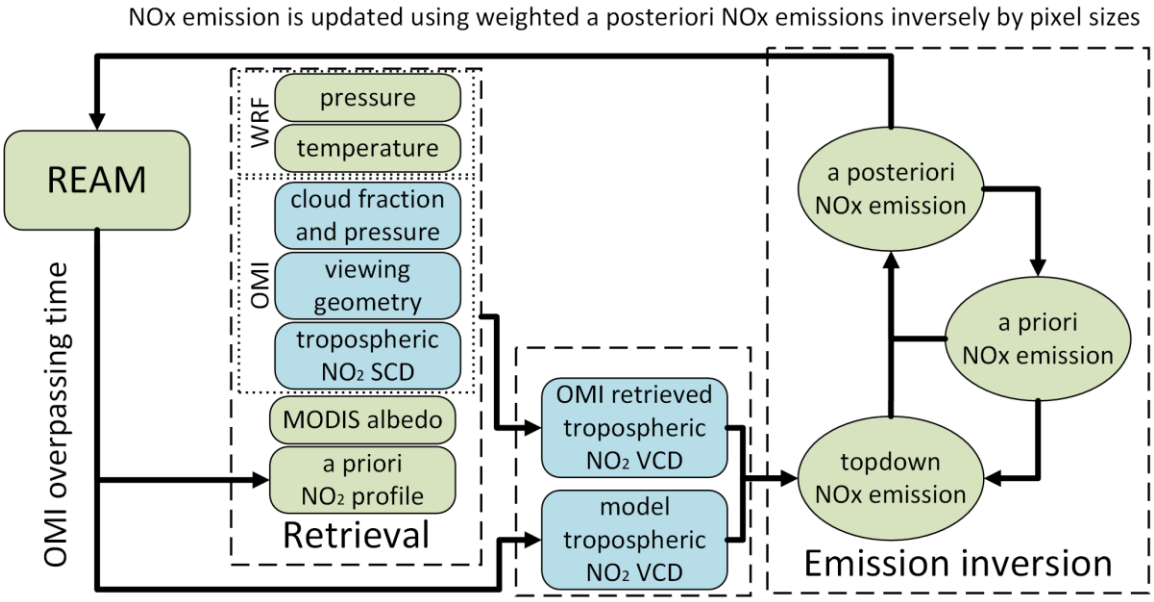

Figure 3.2 HDRI schematic illustration. The green colored boxes represent REAM resolution (4km). The blue colored boxes represent OMI pixel resolution.

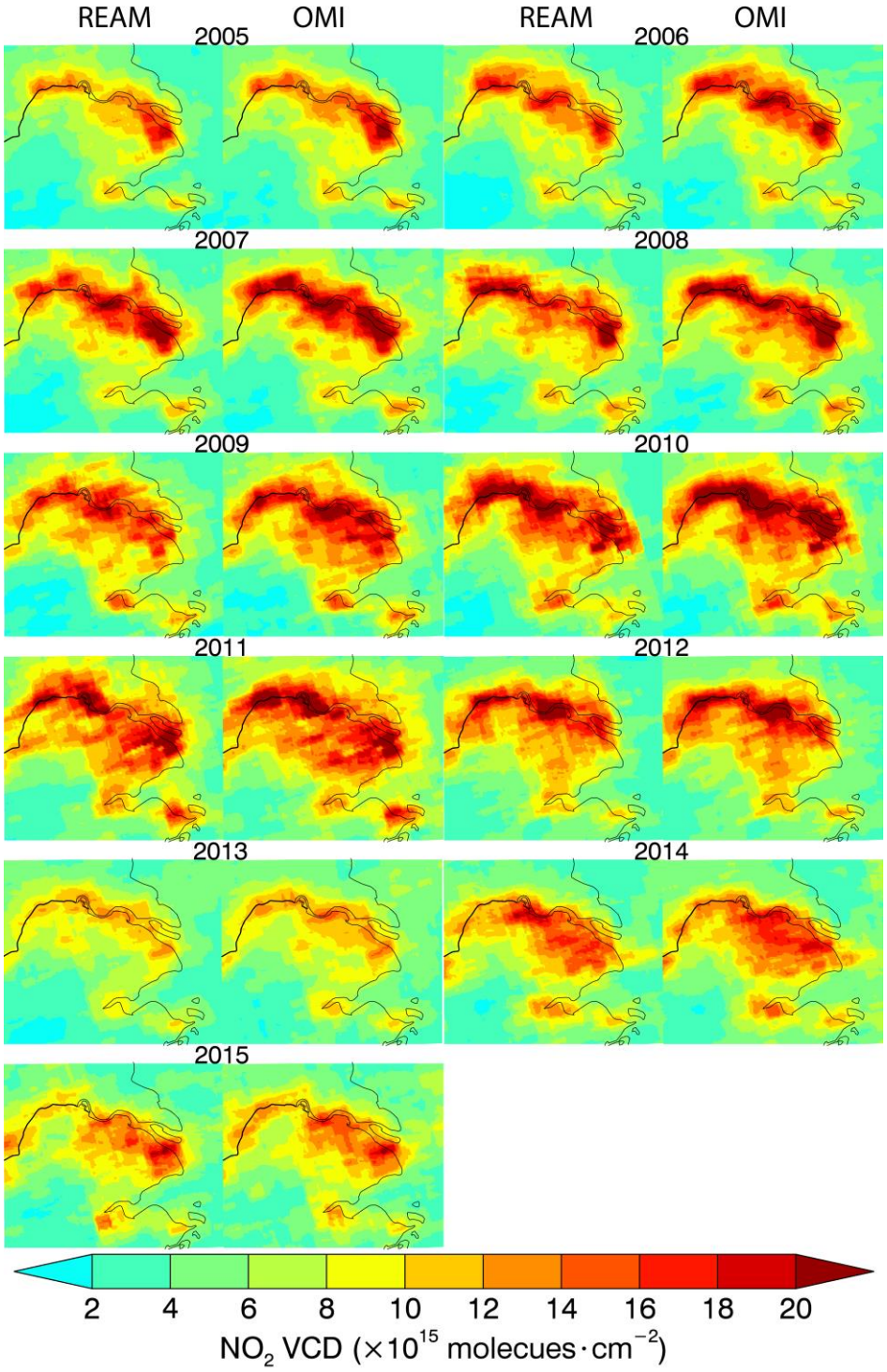

Figure 3.3 The yearly averaged tropospheric NO_2 VCDs from REAM simulation using HDRI emissions and OMI.

3.2.2 Tropospheric NO_2 VCD Retrievals

We implement DAK RTM to calculate tropospheric AMFs and subsequently derive tropospheric NO2 VCDs from SCDs, as illustrated in Figure 3.2. The tropospheric NO2 SCDs are from DOMINOv2.0 product (Boersma et al., 2011) using OMI spectral measurements with a fitting window of 405-465nm. OMI onboard satellite Aura has operated since July 2004 in a sun-synchronous orbit, with 13km×24km ground resolution at nadir pixel. The overpassing time of OMI in Yangtze River region is 11:30-13:30 LT. OMI pixels with cloud fraction more than 0.3 or row anomaly are removed in this study for quality assurance.

The original DOMINOv2.0 algorithm uses 2005-2009 climatology monthly surface reflectance data (Kleipool et al., 2008) inferred from OMI with a spatial resolution of 0.5°×0.5° at 440nm wavelength in calculating AMFs. To account for the rapid land use change and spatial variation in surface reflectance, we substitute the climatology albedo data with MODIS MYD09GA daily albedo product with 500m spatial resolution (Vermote et al., 2005). The MYD09GA albedo product uses the band 3 (459-479nm) of MODIS measurement onboard satellite Aqua, of which the equatorial overpassing time is about 13:30 LT. To account for the difference in wavelengths between the MODIS and OMI albedo products, we derive a ratio between the two products during 2005-2009 and use this ratio to scale MODIS albedo product. The reflectance data are then spatially integrated to 4km×4km resolution, in consistent with REAM grids.

In the calculation of AMFs, we use REAM simulated NO_2 and WRF assimilated temperature and pressure profiles instead of the default profiles in DOMINOv2.0 product, which are obtained from a global CTM TM4 with much coarser resolution (Boersma et al., 2007).

To better represent OMI pixel geometry, we further divide each REAM grid into 16 sub-grids with 1km spatial resolution. We use the ray-casting method (Roth, 1982) to identify the sub-grids within each pixel. Tropospheric NO_2 VCDs are retrieved for each sub-grid and we then derive a pixel-average retrieved tropospheric NO_2 VCD averaged from all the sub-grids within each pixel. This is equivalent to applying the harmonic mean AMF to calculate the pixel-average tropospheric NO_2 VCD.

3.2.3 Emission Inversion

Following the manner of deriving pixel-average retrieved tropospheric NO_2 VCD, we calculate the pixel-average REAM simulated tropospheric NO_2 VCD. The top-down emission is then estimated using the ratio between the retrieved and simulated pixel-average tropospheric NO_2 VCD and the a priori emission. Subsequently, we obtain the a posteriori NOx emission from top-down emission and the a priori emission using the Bayesian method (Martin et al., 2003; Zhao and Wang, 2009; Liu et al., 2012a; Gu et al., 2013, 2014, 2016).

When the horizontal transport is so strong, there are times when the tropospheric NO_2 VCD hotspots shift away from local emission hotspots. This makes inversion less accurate. To diminish the bias introduced by local transport, we develop an “active scaling”

technique: if one pixel of which the pixel-average emission is higher than that of the surrounding 8 pixels, we merge it with another pixel with the highest pixel-average tropospheric NO_2 VCD. The "active scaling" technique ensures more reliable HDRI emissions without compromising the resolution in general.

3.3 Results and Discussions

We compute the composite averaged of HDRI emissions for two periods, i.e. 2005-2009 and 2010-2015, as shown in Figure 3.1. The spatial resolution of HDRI emissions improves greatly compared to that of the MEIC bottom-up emissions (Figure 3.4). We obtain the coal-fired powerplants information (location, capacity, construction date, deNOx type, deNOx date) from China's Ministry of Environmental Protection (http://www.mep.gov.cn) and previous literature (Tian et al., 2013; National Bureau of Statistics of China, 2015; China Electricity Council, 2015). The yellow pins in Figure 3.1 illustrate part of the powerplant clusters, which are visually coincident (within 10km) with lcoal emission hotspots. This confirms that the NOx emissions coincide with coal-fire powerplants (Gu et al., 2014; Liu et al., 2017).

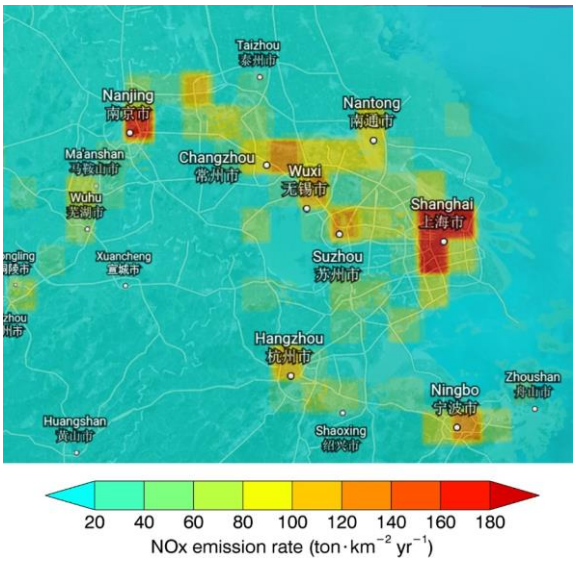

Figure 3.4 The 2010 MEIC NOx emissions.

We compute the total NOx emissions for each city which is fully covered by the simulation domain and summarize the results in Table 3.1 and Figure 3.5. We rank the cities by their gross domestic products (GDPs) in 2010. If not further noted, the economic data used in this research are from the National Bureau of Statistics of China and its local branches (http://www.stats.gov.cn). We additionally list Pudong New Area (Pudong and Nanhui before 2010) of Shanghai for its rapid economic development and high GDP, which is comparable to Nanjing. As expected, cities with higher GDPs generally emit more NOx (Figure 3.5a). Compared to 2010 MEIC emissions, the HDRI emissions are lower in big cities such as Shanghai, Suzhou and are higher by more than 100% in small cities such as Huzhou, Zhoushan and Xuancheng. The NOx emissions peaked at around 2011 according to previous studies (Liu et al., 2016, 2017), and this explains why 2010 MEIC NOx

emissions are higher than the HDRI emissions in big cities. The bottom-up emission estimation approach may be challenging considering the high uncertainties in the statistics of small cities (Streets et al., 2003; Gu et al., 2013). Also, the coarser resolution of MEIC will introduce additional bias in calculating the total emission from smaller cities. This is more evident in Zhoushan, which is an archipelago of islands. The land area of Zhoushan is 1440 km^2, equal to about 2 MEIC grids, while spreading over 6 MEIC grids. The spreading of NOx emissions over the unaccounted ocean in MEIC leads to this low bias.

Table 3.1 HDRI NOx emissions of the cities.

City	2010 GDP (billion RMB)	HDRI NOx emission			2010 MEIC NOx Emission (10^3ton/year)
		2005-2009 (10^3ton/year)	2010-2015 (10^3ton/year)	Change (%)	
Shanghai	1687	390±10	361±7	-8±3	466±25
Suzhou	917	271±7	280±5	3±3	370±16
Wuxi	576	199±6	190±5	-5±4	240±15
Nanjing	501	212±7	202±5	-5±4	216±15
Pudong	494	95±5	107±4	13±7	77±9
Nantong	342	130±6	128±3	-2±5	174±9
Changzhou	298	107±4	107±3	-1±5	129±10
Jiaxing	230	103±4	110±3	6±5	113±6
Zhenjiang	196	139±6	118±3	-15±5	137±9
Huzhou	130	132±5	123±4	-7±5	69±4
Wuhu	111	65±3	80±2	23±5	51±4
Ma'anshan	81	39±2	51±2	33±8	52±5
Zhoushan	63	30±2	29±2	-3±11	10±1
Xuancheng	53	91±3	117±3	29±5	45±2
Tongling	47	51±3	62±3	23±8	34±4

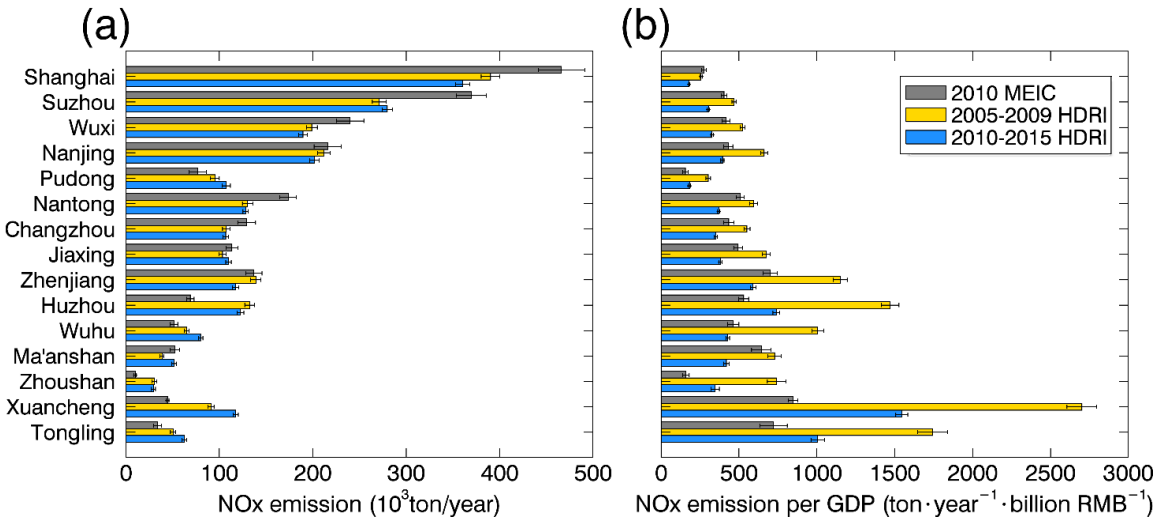

Figure 3.5 (a) NOx emissions of the cities ranked by GDPs. (b) NOx emission per GDP of the cities.

We further calculate NOx emission per GDP for each city by dividing NOx emission by the period averaged GDP (Figure 3.5b). Thanks to the stricter environmental regulations and updated technologies, NOx emission per GDP decreased by 30-58% during 2010-2015 than 2005-2009. The averaged NOx emission per GDP was 479±34, 905±38, 504±16ton yr^{-1} per billion RMB estimated by 2010 MEIC, 2005-2009 HDRI and 2010-2015 HDRI, respectively. Among all 15 cities, Pudong New Area has the smallest NOx emission per GDP, estimated as 156±19, 302±15, 181±7ton yr^{-1} per billion renminbi (RMB) by 2010 MEIC, 2005-2009 HDRI and 2010-2015 HDRI, respectively. In contrast, Xuancheng has the highest emission per GDP, estimated as 846±31, 2701±95, 1545±38ton yr^{-1} per billion RMB, by 2010 MEIC, 2005-2009 HDRI and 2010-2015 HDRI, respectively. The huge contrast between the NOx emission per GDP of Pudong New Area and Xuancheng results from both different levels of regulation enforcement and various

economic structures. The service sector of Pudong New Area contributed 57% to its total GDP in 2010 and this number increased to 67% in 2015. On the contrary, the contribution of industry sector to total GDP of Xuancheng increased from 37% in 2005 to 50% in 2015. The higher NOx emission per GDP in small cities like Xuancheng corresponds to the increasing industrialization.

3.3.1 Urbanization

We calculate the difference between 2005-2009 and 2010-2015 HDRI emissions in Figure 3.6. We then derive the relative change of NOx emissions in Figure 3.7. NOx emissions from coal-fired powerplants are computed as the HDRI emission of the powerplant locations. The derived powerplant emissions are reasonably compared with 2010 MEIC (Figure 3.8, Table 3.2). NOx emissions in Suzhou, Pudong, Jiaxing, Wuhu, Ma'anshan, Xuancheng and Tongling increase. The latter four cities with smaller GDPs feature higher NOx emission increase by 23±7%, 33±4%, 29±3%, and 23±3%, respectively. The powerplant and non-powerplant NOx emission changes offset each other in Nantong and Changzhou, resulting in negligible total NOx emission changes. Although China has enforced stricter vehicle emission standards, e.g. the use of Euro III and Euro IV standards (Wu et al., 2017), only Wuxi, Changzhou, Zhenjiang and Huzhou have a decrease of non-powerplant NOx emissions. The increases of non-powerplant NOx emissions in other cities might result from rapidly growing on-road vehicle population (Wu et al., 2017), urbanization and industrialization.

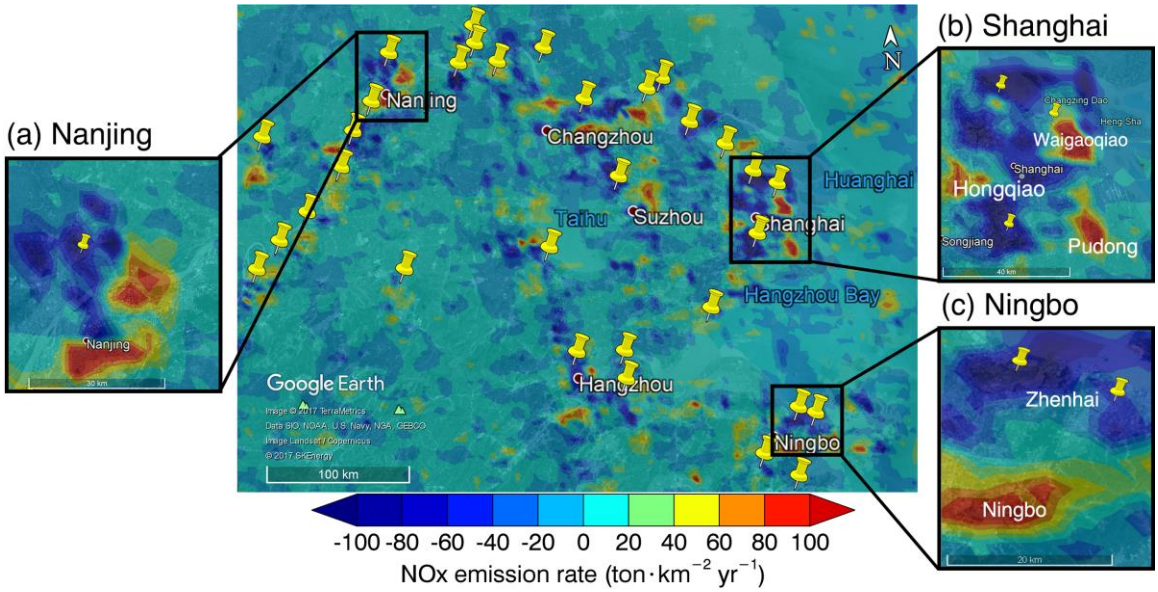

Figure 3.6 The difference between HDRI emissions averaged from 2010-2015 and 2005-2009, shown as the colored background. The panels (a)-(c) show the urbanization of Nanjing, Shanghai and Ningbo, respectively.

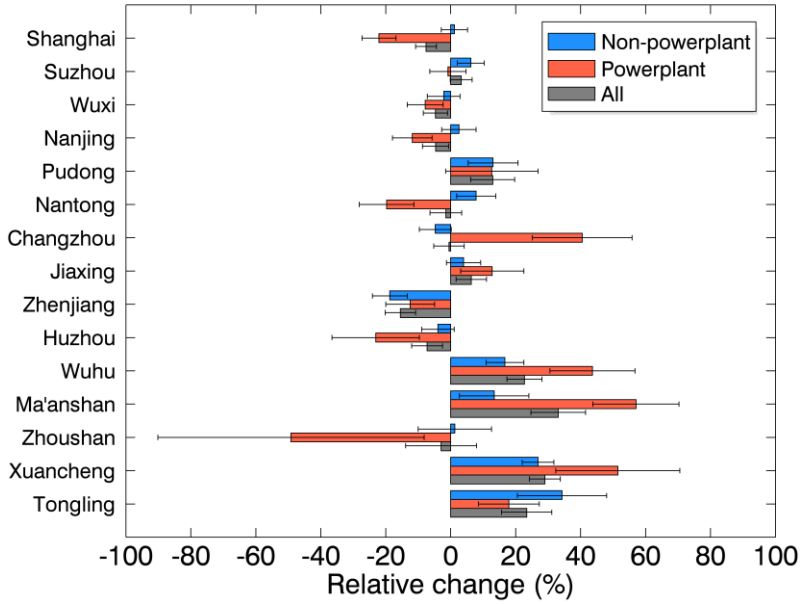

Figure 3.7 The relative changes of HDRI emissions between 2010-2015 and 2005-2009 in cities, which are fully covered by the model domain. The cities are ranked by the GDPs, with Shanghai the highest. Pudong, a district of Shanghai, is additionally listed as a separate city.

We highlight three cities, i.e. Nanjing, Ningbo and Shanghai to investigate the effects of urbanization on NOx emissions. In Nanjing (Figure 3.6a), NOx emissions shift southward from the more industrialized region to more commercialized district. Quantitively, the powerplant and non-powerplant NOx emissions of Nanjing change by -12±13% and 3±11%. The similar pattern is also seen in Ningbo (Figure 3.6c), where NOx emissions shift from coastal Zhenhai district towards urban Ningbo. Zhenhai is famous for its petro-chemical economy, especially Zhenhai Refinery and Chemical Corporation, the largest oil refinery in China.

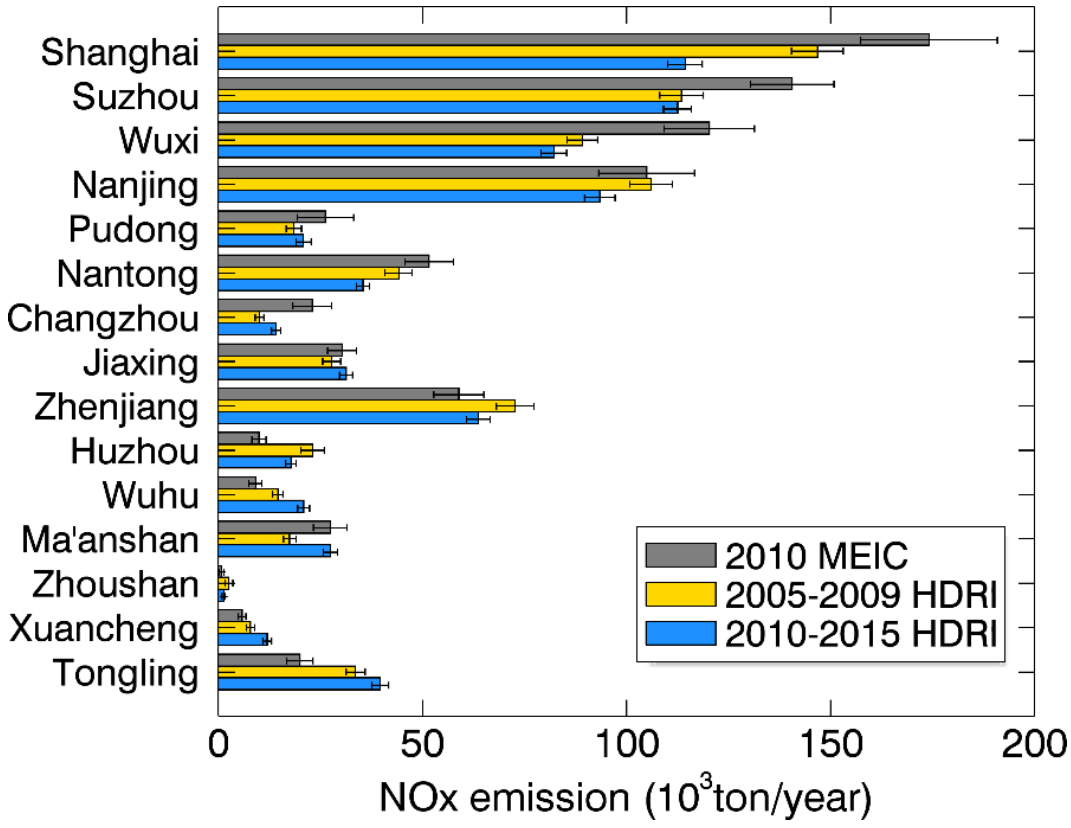

Figure 3.8 Coal-fired powerplant NOx emissions of the cities ranked by GDPs.

Table 3.2 HDRI NOx emissions from coal-fired powerplants of the cities.

City	2010 GDP (billion RMB)	HDRI NOx emission			2010 MEIC NOx Emission (10^3ton/year)
		2005-2009 (10^3ton/year)	2010-2015 (10^3ton/year)	Change (%)	
Shanghai	1687	147±6	114±4	-22±5	174±17
Suzhou	917	113±5	113±3	-1±6	141±10
Wuxi	576	89±4	82±3	-8±6	120±11
Nanjing	501	106±5	93±4	-12±6	105±12
Pudong	494	18±2	21±2	13±14	26±7
Nantong	342	44±3	35±2	-20±8	52±6
Changzhou	298	10±1	14±1	41±15	23±5
Jiaxing	230	28±2	31±2	13±10	30±4
Zhenjiang	196	73±5	64±3	-12±8	59±6
Huzhou	130	23±3	18±1	-23±13	10±2
Wuhu	111	15±1	21±1	44±13	9±2
Ma'anshan	81	17±1	27±2	57±13	27±4
Zhoushan	63	2.6±1.0	1.3±0.4	-49±41	1±0.6
Xuancheng	53	8±1	12±1	51±19	6±1
Tongling	47	34±2	40±2	18±9	20±3

Shanghai, the host city of Expo 2010, has enforced multiple strict environmental regulations since early 2010 (Wang et al., 2012). NOx emission in Shanghai is reduced by 8±8% during 2010-2015 compared to 2005-2009. Powerplant NOx emissions decrease by 22±9% while non-powerplant NOx emissions have an insignificant increase of 1±14%. In contrast, both powerplant and non-powerplant NOx emissions in Pudong increase (Figure 3.6b), by 13±13% and 13±6%, respectively. In 2005, the GDP of Pudong New Area (formerly as Pudong+Nanhui) was 240 billion RMB, constituting 25% that of Shanghai. In 2015, its GDP increased to 790 billion RMB and this portion increased to 32%. Pudong

New Area achieved an average GDP increasing rate of 11% yr^{-1}, succeeding Shanghai's averaged rate of 9% yr^{-1}. The surge of GDP of Pudong New Area partly attributes from favorable policies. Since August 2009, Pudong has merged with Nanhui, which was also a district of Shanghai. Pudong New Area took advantage of Pudong's Waigaoqiao port and Nanhui's Yangshan port, which complement each other. Also, the less urbanized Nanhui district offered opportunities for further urban expansion and development. In August 2013, Shanghai Free Trade Zone was established inside Pudong New Area, further increasing its economic potential. The economic growth boosts the development in the Southern part of Pudong New Area, formerly known as Nanhui, which is confirmed by the NOx emission increase in Figure 3.6b. The NOx emission growth in the Northern part of Pudong, also known as Waigaoqiao, results from the installations and operations of two 1000MW coal fired powerplants since 2008 and the ever-growing Waigaoqiao cargo port. The NOx emission increase in west Shanghai (Figure 3.6b) locates Hongqiao Central Business District (CBD). Hongqiao CBD and Pudong New area are now known as "Great Hongqiao" and "Great Pudong", the two major engines for further economic development. Hongqiao CBD has been a significant part of the 12^{th} (2011-2015) and 13^{th} (2016-2020) five-year plan of the Shanghai Municipal Government. Hongqiao Integrated Transport Hub supports the CBD to serve Yangtze River region and national needs. The two most essential parts of Hongqiao ITH are Hongqiao Airport and Hongqiao railway station. In March 2010, Hongqiao Airport finished its 5-year construction of the new Terminal 2 and a second aircraft runway, boosting the airport capacity from 9.6 to 40 million travelers per year. Hongqiao high-speed railway station with 30 platforms came to operations in July 2010.

Both policy and infrastructure favored the development in Hongqiao CBD. The associated construction as well as increasing traffic leads to higher NOx emission than before.

3.3.2 Powerplant deNOx Effectiveness

We calculate the NOx emission factors in coal-fired powerplants as the total NOx emissions divided by the total electricity generation within 10km of the powerplant locations. Figure 3.9a shows the NOx emission factors derived from 2010 MEIC and 2005-2015 HDRI inverse emissions. The averaged NOx emission factors are 2.0±0.5/kWh and 2.1±0.1g/kWh, respectively. These emission factors are expected slightly biased high since we implicitly assume that all the emissions in the corresponding grids are emitted from powerplants. Tian et al. (2013) estimated the NOx emission factors for Jiangsu, Zhejiang, Shanghai and Anhui are 1.8, 1.7, 1.6 and 2.3g/kWh (Tian et al., 2013), respectively. The high bias of our estimation is about 0.3g/kWh and 15%. Both MEIC and HDRI emissions capture that the NOx emission factors decline with higher generation capability. This implies higher environmental efficiency for larger powerplants (Tian et al., 2013).

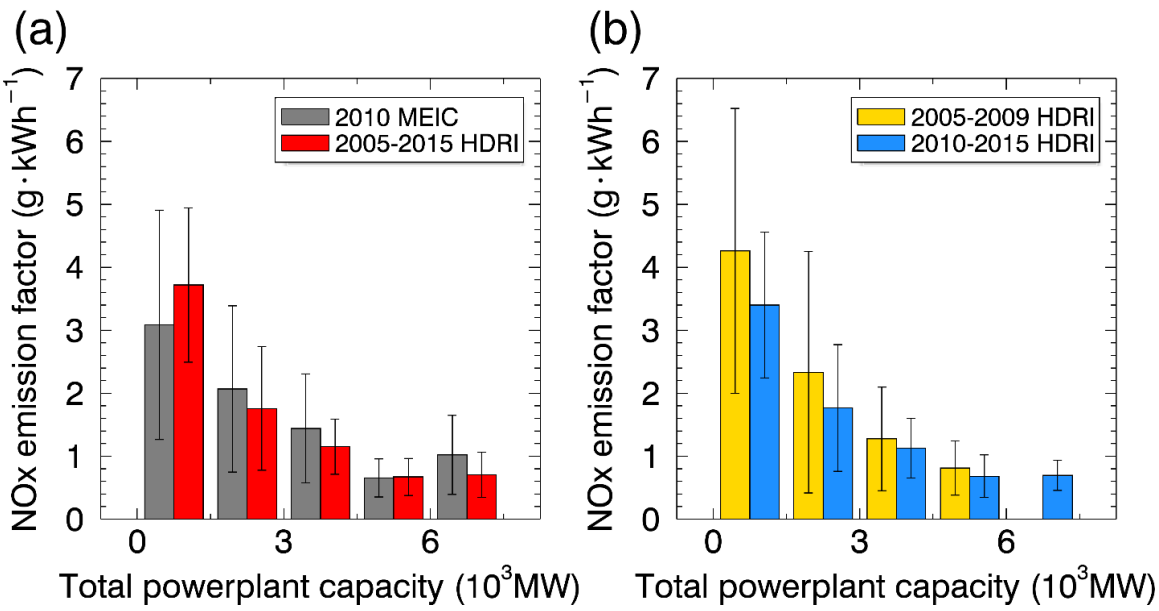

Figure 3.9 The panel (a) shows NOx emission factors derived from 2010 MEIC and 2005-2015 averaged HDRI emissions in this study. The panel (b) shows NOx emission factors calculated during 2005-2009 and 2010-2015 averaged HDRI emissions, respectively. The x-axis is the total powerplant capacity and is binned every 1500MW.

Before 2010, less than 10% of total coal-fired powerplant capacity was equipped with deNOx system in the model region. This number increased to over 60% in 2015. To quantify the NOx reduction due to the implementation of deNOx systems, we derive the NOx emission factors during 2005-2009 and 2010-2015 in Figure 3.9b. As expected, NOx emission factors are uniformly higher during the first period than the latter. The averaged NOx emission factors are 2.8±0.2 and 1.8±0.1g/kWh, with a 36% decrease. The non-parametric Wilcoxon test yields a p-value of 0.042, indicating that the NOx emission factor decrease is significant at the level of 0.05. In comparison, previous studies estimated that the national averaged NOx emission factors of coal-fired powerplants are 4.23 (Lv et al.,

2002), 2.28 (Tian et al., 2013), and 1.75g/kWh (Central People's Government of the People's Republic of China, 2012; Tian et al., 2013) for 2005, 2010, and 2015 respectively.

The two prevalent deNOx systems are SCR and SNCR. In practice, the fractions of NOx removed by SCR and SNCR were estimated to be 70% and 25% in 2010 (Tian et al., 2013). In Yangtze River region, only small powerplant units with less than 50MW capcity are installed with SNCR, constituting less than 2% of total capacity installed with deNOx systems. Larger powerplants are equipped with SCR for its higher NOx removal efficiency. Thus, the 36% decrease of NOx emission factor mainly results from the application of SCR.

The total powerplant capacity in the region increases by about 50% during 2010-2015 than 2005-2009, while the total powerplant NOx emission declines from 709 to 666 $\times 10^3$ton/year, by 6%. This is explained by the increasing applications of SCR and subsequent reduced NOx emission factor offset the ever-growing electricity generation. With more applications of deNOx systems, the emission factors from coal-fired powerplants are expected to continuously fall.

CHAPTER 4. RECONCILING THE DIFFERENCES BETWEEN OMI-BASED AND EPA AQS IN SITU NO_2 TRENDS[3]

4.1 Introduction

As we discuss in Section 3.1, NO_2 is harmful to both ecosystem and human health.

Surface NO_2 concentrations are regulated by the U.S. EPA through the National Ambient Air Quality Standards (NAAQS). NO_2 is measured routinely at the EPA AQS sites (Demerjian, 2000). Although the AQS network continually provides valuable hourly NO_2 measurements, AQS sites are mostly located in urban and suburban regions, leaving large regions of rural areas unmonitored. Satellite data provide a better spatial coverage than the in situ measurements.

Several satellites were launched to monitor tropospheric NO_2 VCDs, such as the SCIAMACHY, the Global Ozone Monitoring Experiment-2 (GOME-2), and OMI. For trend analysis, the tropospheric NO_2 products from OMI surpass the others for a relatively high spatial resolution and over one decade of continuous operation (Boersma et al., 2004; Boersma et al., 2011). Thus, OMI NO_2 retrievals are widely applied in NO_2 and NOx emission trend studies (e.g., Lin et al., 2010, 2011; Castellanos et al., 2012; Russell et al.,

[3] This chapter is an extension of "Reconciling the Differences between OMI-based and EPA AQS In Situ NO_2 Trends", to be submitted to Atmospheric Measurement Techniques. The co-authors are Ruixiong Zhang, Yuhang Wang, Charles Smeltzer, Hang Qu, William Koshak, Folkert Boersma, and Edward Celarier.

2012; Gu et al., 2013; Lamsal et al., 2015; Lu et al., 2015; Tong et al., 2015; Cui et al., 2016; Duncan et al., 2016; de Foy et al., 2016a, 2016b; Krotkov et al., 2016; Liu et al., 2017). Tong et al. (2015) reported that the reduction rates calculated from OMI NO_2 VCDs and AQS surface NO_2 data at eight cities were 35% and 38% during 2005-2012, respectively. Lamsal et al. (2015) also found the divergence between the annual trends inferred from the two datasets, i.e. -4.8% yr^{-1} vs -3.7% yr^{-1} during 2005-2008, and -1.2% yr^{-1} vs -2.1% yr^{-1} during 2010-2013.

To understand how the retrieval procedure affects the resulting OMI derived trends and their differences from those derived from the surface AQS measurements, we utilize a regional 3-D CTM, a RTM, and the Mann-Kendall method (Mann, 1945; Kendall, 1948) to calculate OMI-based NO_2 seasonal relative trends during Dec-Jan-Feb (DJF), Mar-Apr-May (MAM), Jun-Jul-Aug (JJA), and Sept-Oct-Nov (SON) (Section 4.3). To reconcile with the AQS based regional NO_2 trends, we find that three procedures are essential to ensure the quality of trend analysis using OMI tropospheric NO_2 VCDs, including the ocean trend removal, the MODIS albedo update in calculating the AMFs, and the screening of lightning events (Section 4.3.1). With these procedures implemented, the differences between OMI-based and AQS in situ annual relative trends are within 0.8% of coincident measurements for all the four regions. Finally, we estimate the OMI-based annual relative trends across the nation in Section 4.3.2. Conclusions are given in Section 4.4.

4.2 Methods

4.2.1 EPA AQS Surface NO_2 Measurements

The in situ surface NO_2 measurements from the U.S. EPA AQS network are used in this research. Sites with a continuous gap of more than 50 days are removed and the observations of 140 remaining cites are used (Figure 4.1). The AQS chemiluminescent analyzers are equipped with molybdenum converters to measure ambient NO_2 concentrations. These analyzers are known to have high biases, since the converters are not NO_2 specific and they measure some fractions of peroxyacetyl nitrate, nitric acid and organic nitrates (Demerjian, 2000; Lamsal et al., 2008). In addition to chemiluminescent analyzers, several NO_2 specific photolytic instruments were deployed since 2013. By utilizing the data from both chemiluminescent and photolytic measurements at coincident sites during the overpassing time of OMI, we calculate the observed NO_2 concentration ratio between both measurements in Figure 4.2.

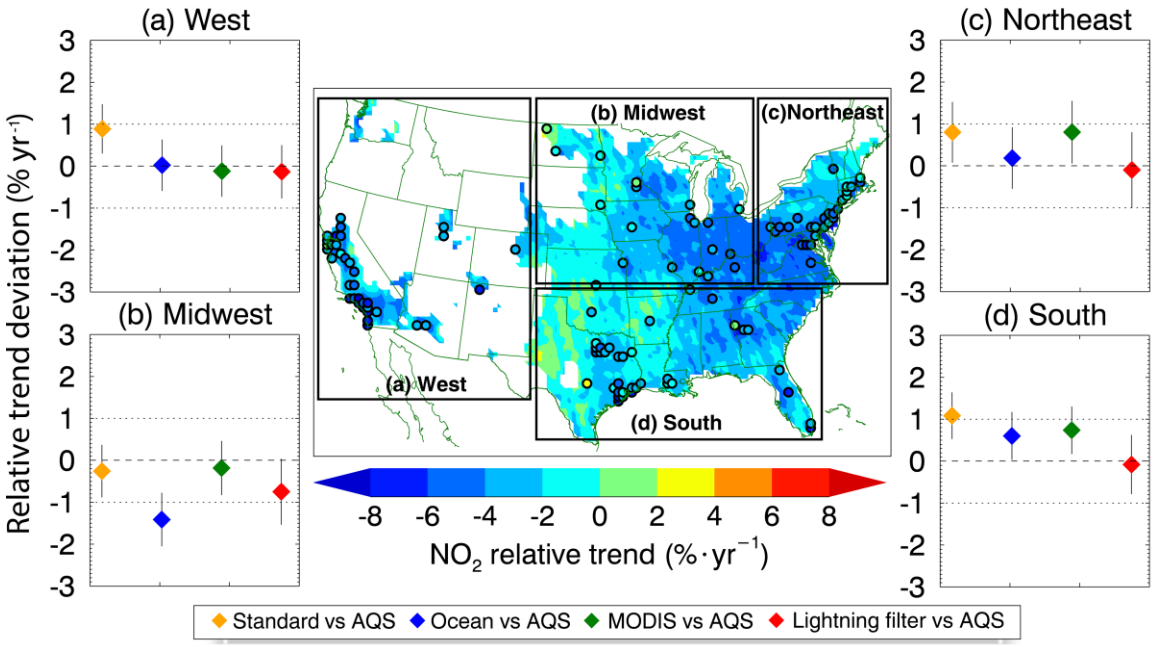

Figure 4.1 The solid black borders in the center map define the four regions used in this study. The colored background shows the OMI-based NO_2 annual relative trends of the "lightning filter" data. Mean NO_2 VCD values < $1\times10^{15} molec/cm^2$ during 2005-2014 are not used in this study and are shown in white. The black bordered circles represent the locations of AQS sites. Panel (a) through (d) show the regional difference of annual relative trend between coincident OMI-based and AQS in situ data. The colored diamonds are for "Standard" (orange), "Ocean" (blue), "MODIS" (green), and "Lightning filter" (red) OMI data, respectively. The different OMI VCD data are described in Section 4.2.3.

The ratio peaks at 2.3 in June and decreases to 1.3 in November, indicating that the chemiluminescent analyzers overestimate 27%-132% than photolytic instruments. This finding is in agreement with Lamsal et al. (2008). We correct the chemiluminescent NO_2 data by the observed ratio (Figure 4.2). This correction may contribute to the differences between in situ and OMI based absolute NO_2 trends but do not significantly affect the

relative trends (since the correction is canceled out in computing relative trends). In this study, we only examine the relative trends.

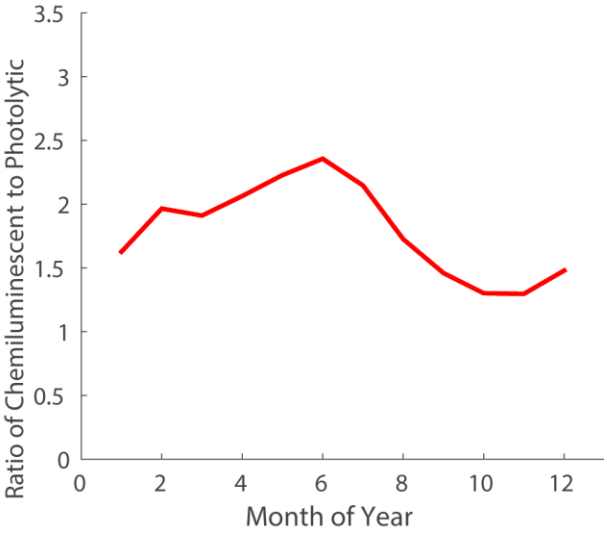

Figure 4.2 The ratios between surface NO_2 concentrations of chemiluminescence to photolytic instruments. The ratios are calculated for each month from the sites with coincident photolytic measurements.

4.2.2 3-D REAM Model

We use a 3-D REAM in the simulation of NO_2 profiles. As described in Section 1.2, REAM features a horizontal resolution of 36km, 30 vertical layers in the troposphere and 5 vertical layers in the stratosphere, with a model top of 10hpa. In this study, the domain of REAM is about 400km larger than contiguous United States (CONUS). Meteorology inputs driving transport process are simulated by the WRF assimilations constrained by NCEP CFSR (Saha et al., 2010) 6-hourly products. We run the WRF model

with the same resolution as in REAM but with a domain 10 grids larger than that of REAM. REAM updates most of the meteorology inputs every 30 minutes while those related to convective transport and lightning parameterization are updated every 5 minutes. The chemistry mechanism expands that of a global CTM GEOS-Chem (V9-02). For consistency, the GEOS-Chem (V9-02) simulation with 2.0°×2.5° resolution is used to generate initial and boundary conditions for chemical tracers.

Anthropogenic emissions of NOx and other chemical species are from the U.S. NEI 2008 prepared by Sparse Matrix Operator Kernel Emission (SMOKE) model. NEI is updated triennially, however, the changes are due to both real emission changes and different approaches. To keep consistent in this analysis, we only use NEI 2008 as anthropogenic emissions. Biogenic emissions are simulated online using the MEGAN algorithm (v2.1, Guenther et al., 2012). We parameterize lightning emitted NOx as a function of convective mass flux, Convective Available Potential Energy (CAPE) and the cloud-to-ground (CG) lightning detected by the National Lightning Detection Network (NLDN) (Choi et al., 2005). NOx production per flash is set to 250 moles NO per flash, and the emissions are distributed vertically following the C-shaped profiles by Pickering et al. (1998).

4.2.3 OMI-based NO_2 VCDs

We retrieve the tropospheric NO_2 VCDs using the SCDs from the KNMI DOMINOv2.0 (Boersma et al., 2011). OMI onboard the Aura satellite was launched in July 2004 and is still active. OMI overpasses the equator at about 13:30 LT and obtains

global coverage with a 2600 km viewing swath spanning 60 rows. It has a ground level spatial resolution up to $13km \times 24km$ (at nadir). In the DOMINOv2.0 algorithm, is computed from a fitting window of 405-465nm of backscattered sunlight. The stratospheric portion of SCDs are estimated and subsequently removed with a global CTM TM4 with stratospheric ozone assimilation (Boersma et al., 2007). Deriving tropospheric VCDs from the remaining tropospheric SCDs requires the calculation of tropospheric AMFs. Being an optically thin gas, tropospheric AMF for NO_2 can be calculated from AMF for each vertical layer (AMF_l) weighted by NO_2 VCDs at the corresponding layer (x_l) (Boersma et al., 2004), as shown in equation (1).

$$tropospheric\ AMF = \frac{tropospheric\ SCD}{tropospheric\ VCD} = \frac{\int AMF_l x_l dl}{\int x_l dl} \quad (1)$$

As the vertical distribution of NO_2 is usually unknown, we typically substitute x_l by an a priori profile ($x_{l,apriori}$) from a CTM. AMF_l is the sensitivity of NO_2 absorption at a given altitude weighted by NO_2 abundance (Eskes and Boersma, 2003), and is computed using a RTM.

As a result, the retrieved tropospheric NO_2 VCD is hereby determined and influenced by the a priori NO_2 vertical profile, the surface reflectance, the surface pressure, the temperature profile, and the geometry (Boersma et al., 2011). Previous studies have addressed sources of uncertainties in NO_2 retrievals, including surface reflectance resolutions (Russell et al., 2011; Lin et al., 2014), lightning events (Martin et al., 2007; Bucsela et al., 2010), a priori CTM uncertainties (Russell et al., 2011; Heckel et al., 2011; Lin et al., 2012; Laughner et al., 2016), surface pressure in rugged terrain (Zhou et al.,

2009), cloud and aerosol radiance (Lin et al., 2014, 2015), and boundary layer dynamics (Zhang et al., 2016). We find that the first two contribute most to the NO_2 trend, and will discuss these in the following sections.

We calculate AMF_l using the DAK v2 RTM, with NO_2 profiles from REAM, temperature and pressure from WRF, viewing geometry and cloud information from DOMINOv2.0 product. We use the model results of 2010 to avoid the uncertainty introduced by variability of NO_2 profiles. The yearly variation of meteorology has little impact on the trend analysis (Lamsal et al., 2015). We use the surface reflectance from DOMINOv2.0 product as default, and update it using a surface reflectance product with higher temporal resolution (Section 4.2.3.2).

We develop three variations of the "Standard" OMI-based NO_2 relative trends, i.e. "Ocean" in Section 4.2.3.1, "MODIS" in Section 4.2.3.2 and "Lightning filter" in Section 4.2.3.3. These variations progressively decrease until minimize the discrepancy between OMI-based and AQS in situ NO_2 relative trends, as discussed in Section 4.3.

4.2.3.1 Ocean Trend Removal

For trend and other analyses of OMI tropospheric VCDs, the data of anomalous pixels must be removed. The row anomaly initially occurred in June 2007 and subsequently expanded to include row 26 to 40 (Boersma et al., 2011). We choose a region in the remote North Pacific with minimum marine traffic (Figure 4.3a) to illustrate the effect of row anomaly on NO_2 VCDs (Figure 4.3b). Additional anomalies can be found in some years in row 41 to 55. For trend analysis from 2005-2014, we exclude row 26 to 55. In addition, the

data of coarse spatial resolution from row 1 to 5 and row 56 to 60 are also excluded, as suggested by Lamsal et al. (2015). Furthermore, we exclude OMI data with cloud fraction > 0.3 to minimize retrieval uncertainties due to clouds and aerosols (Boersma et al., 2011; Lin et al., 2014).

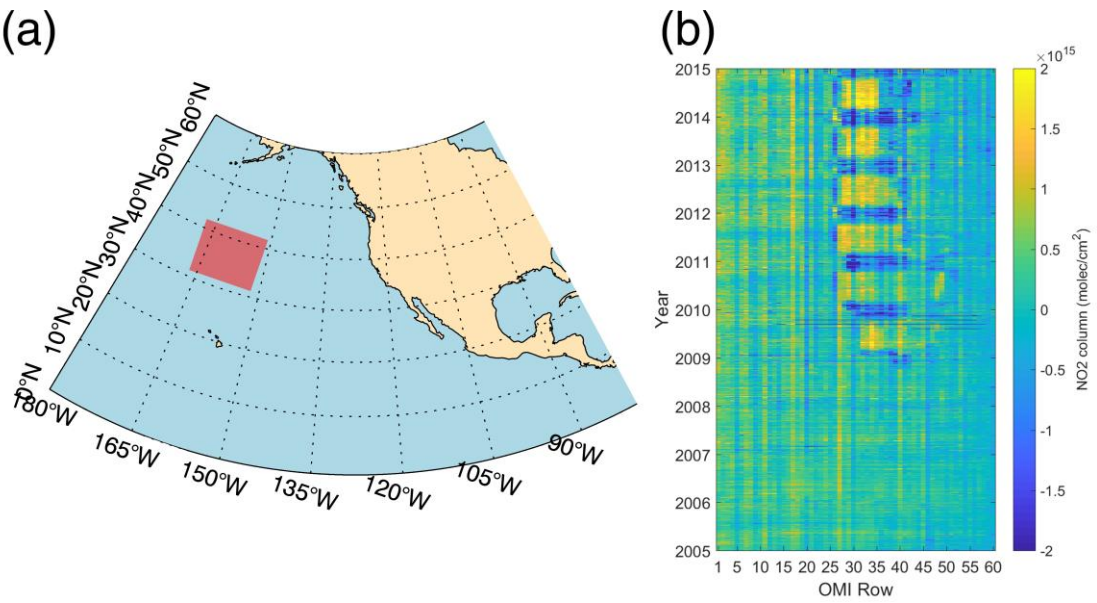

Figure 4.3 The panel (a) shows the OMI tropospheric NO_2 VCDs from different OMI rows (x-axis) in a remote region (the red area in panel (b)) during 2005-2014. The row anomaly (row 25 to 55) becomes apparent after 2009.

Figure 4.3 shows that there is an apparent increasing trend of the residual tropospheric VCDs in the remote ocean region. The reason is unclear; it may reflect an increase of noise in the OMI sensor. Figure 4.4 shows that there is a positive annual trend of $2.49\pm0.27\times10^{13}$ molecules cm^{-2} yr^{-1}. We only analyze OMI tropospheric column trend for data with 2005-2014 averaged VCDs > 1×10^{15} molecules cm^{-2}, which tends to minimize

the effect of the background noise. However, removing this background ocean (absolute) trend has a non-negligible effect in reducing the OMI relative trend (Figure 4.1). We refer such derived (relative) trend data as "Ocean". An alternative method is to subtract monthly VCDs of the remote ocean region from the OMI tropospheric VCD data. Although the end results are essentially the same as the trend removal method, noises are added to the VCD data, making it more difficult to understand the effects of MODIS albedo update and lightning filtering (next sections). We therefore choose to use the (absolute) trend removal method here.

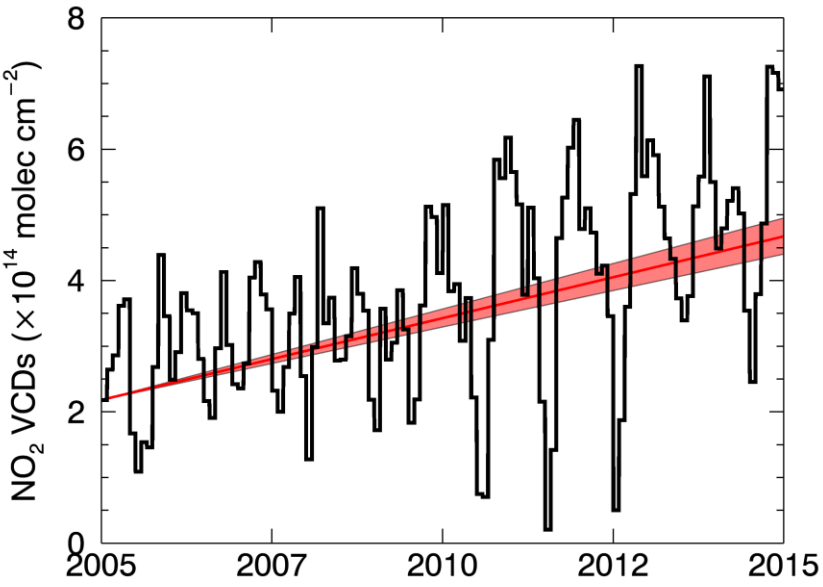

Figure 4.4 The black line shows the monthly OMI tropospheric NO_2 VCD values in the North Pacific region (red box in Figure 4b). The red line represents the ocean trend used in this research, with the 95% confidence intervals shaded in red.

4.2.3.2 MODIS Albedo Update

The albedo used to calculate the AMF_l in "Standard" and "Ocean" is from DOMINOv2.0 product, which is the climatology of averaged OMI measurements during 2005-2009 with a spatial resolution of 0.5°×0.5° (Kleipool et al., 2008) and is valid for 440 nm. We recalculate the AMF_l using the MODIS 16-day MCD43B3 albedo product with 1km spatial resolution, which combines data from both MODIS onboard Aqua and Terra satellites (Schaaf et al., 2002; Tang and Zhang, 2007). Aqua and Terra have an equatorial overpassing time of 13:30 LT and 10:30 LT, respectively. The band 3 (459nm-479nm) is used to match the NO_2 fitting window (405nm-465nm). The albedo is spatially integrated to the geometry of OMI pixels and is temporally interpolated to match OMI overpassing dates. In order to maintain the consistency of the DOMINO retrieval algorithm (Boersma et al., 2011), we only use the MODIS data to improve the temporal variations of albedo data used in the retrieval by scaling the MODIS albedo data such that the mean albedo is the same as the OMI climatology at 0.5°×0.5°. We recalculate OMI tropospheric VCDs using the MODIS albedo data as described. We recalculate the relative OMI trend and remove the ocean (absolute) trend (Section 4.2.3.1). We refer this version of OMI relative trend data as "MODIS".

4.2.3.3 Lightning Event Filter

Over North America, lightning is a major source of NOx in the free troposphere and its simulations in CTMs are uncertain (e.g., Zhao et al., 2009a; Luo et al., 2017). The large temporospatial variations of lightning NOx make it difficult to compute satellite

based NO_2 trends by changing the vertical distributions of NO_2 affecting the AMFs calculation (e.g., Choi et al., 2008b; Lamsal et al., 2010) and the SCD values. Given the difficulty to simulate lightning NOx accurately across different years, we use a "lightning filter" to filter out potential effects of lightning NOx on the basis of the flash rate observations of CG lightning by the NLDN network (Cummins and Murphy, 2009; Rudlosky and Fuelberg, 2010). Since the lifetime of NOx in the free troposphere can be up to 1 week, we filter out the data with a radius of 90 km (about 2 model grid cells around the lightning flash cell) of a CG occurrence for a period of 72 hours after the occurrence. Since lightning usually occur along the track of a thunderstorm; the 90km radius is more a constraint on lightning NOx effects across the track. The extended period of 72 hours is to ensure that we exclude data affected by lightning NOx. Figure 5 shows the distribution of the number of days of 2005-2014 with lightning detection.

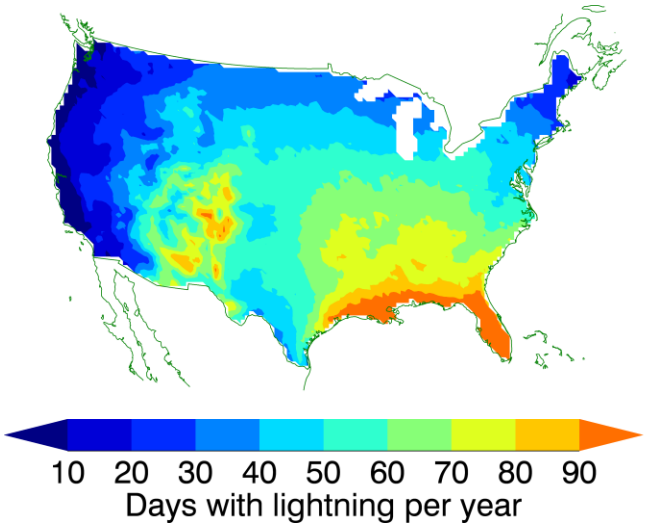

Figure 4.5 Days with NLDN detected lightning per year during 2005-2014. The lightning occurrences are calculated using the REAM grid resolution.

The Southwest monsoon and South regions have more lightning days than the other areas. While there are fewer lightnings in the Northeast than the South (Figure 4.5), large amounts lightning NOx can be produced by high flash ratios of severe thunderstorms and they can be transported northward from the South to the Northeast (Choi et al., 2005). We therefore further screen the data in the Northeast on the basis of CG lightning flash rates in the South. If the averaged CG flash rate in the South grid cells exceeds the 95th percentile value of the NLDN observations, which is 0.035 flash km^{-2} day^{-1} (Figure 4.6), we exclude in the analysis the Northeast OMI data in the following 72 hours.

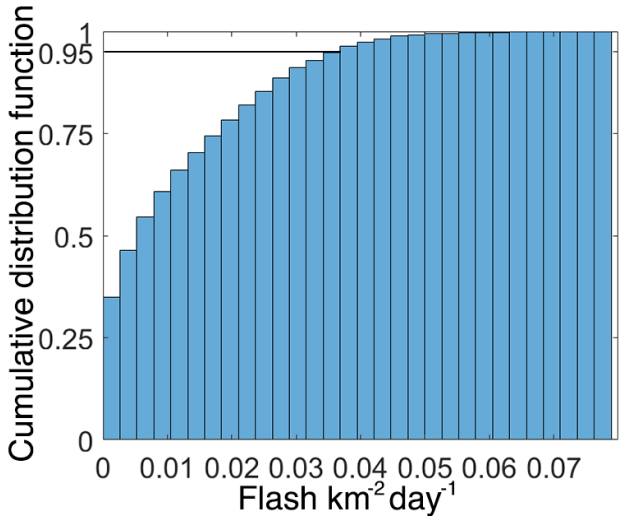

Figure 4.6 The cumulative distribution function of NLDN detected CG lightning density over the South of the United States.

4.3 Results and Discussion

We group the analysis results into different regions: (a) West, (b) Midwest, (c) Northeast, and (d) South (Figure 4.1), following the regional divisions by the United States

Census Bureau. To make a fair comparison between the in situ and OMI-based trends, we only use spatially and temporally coincident in situ and OMI NO_2 observations. We apply the Mann-Kendall method to calculate the relative trend of NO_2 for each season, i.e. DJF, MAM, JJA, and SON, during 2005-2014. We construct the uncertainties of the trends with a confidence level of 95%. Noted that the screen of data in variation "Lightning filter" leads to slightly different in situ NO_2 trends in the comparisons (Section 4.3.1.3). We first compute the trends using the "Standard" OMI VCD data. The ocean trend removal, MODIS albedo update, and lightning filter are then added in sequence to compute 3 different OMI-based NO_2 trends to compare to the AQS in situ results. A subtlety in the comparison is that the coincident data change when the lightning filter is applied. As a result, the AQS in situ results in this set of comparison differ from those in the other three sets.

4.3.1 In Situ and "Standard" OMI-based Trends

Figure 4.7 shows that both AQS in situ and "Standard" OMI-based seasonal relative trends are negative for all seasons across the regions. OMI-based trends generally underestimate the decreasing trends by up to 3.7% yr^{-1} except for the large overestimation in the Midwest and Northeast regions during DJF. The overestimates in these two regions are 3.4% yr^{-1} and 1.1% yr^{-1}, respectively. On average, the differences between OMI-based and in situ seasonal relative trends are 1.4% yr^{-1}, -1.0% yr^{-1}, 1.0% yr^{-1}, and 1.4% yr^{-1} for the West, Midwest, Northeast and South regions, respectively. Note that the relative trends are calculated using coincident measurements for the comparisons. The seasonal difference of the trends reflects in part the non-linear photochemistry (Gu et al., 2013), which is more

active in summer than the other seasons. The focus of this work is to reconcile the difference between AQS in situ and OMI-based trends, which will be discussed in the following sections.

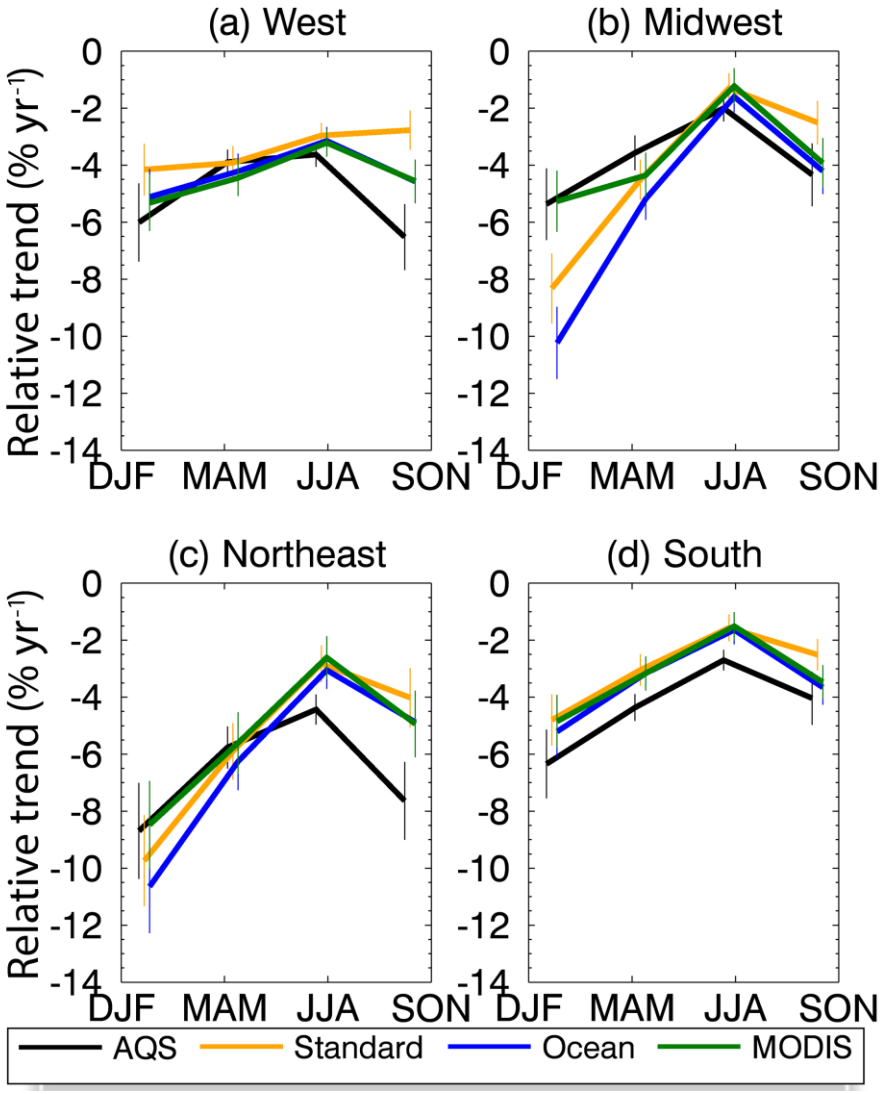

Figure 4.7 Seasonal relative trends of NO_2 calculated from the AQS in situ measurements ("AQS", black line) and those derived from different OMI VCD data ("Standard", orange line; "Ocean", blue line; "MODIS", green line). The error bars represent 95% confidence intervals.

4.3.1.1 Improvement due to Ocean Trend Removal

After removing the ocean trend as discussed in Section 4.2.3.1, the OMI-based trends are less as shown in Figure 4.7 ("Ocean", blue line) by 0.1-1.7% yr^{-1}. The regional relative trends have different sensitivities to the ocean trend removal due to different tropospheric VCDs levels. In general, the discrepancies between OMI-based and in situ trends are reduced except for the Midwest and Northeast regions during DJF, which are already biased low. The averaged differences between OMI-based and in situ seasonal relative trends for the West, Midwest, Northeast and South regions are 0.7% yr^{-1}, -2.0% yr^{-1}, 0.4% yr^{-1}, and 0.9% yr^{-1}. Only in the Midwest region, removing the ocean trend enlarges the differences due to the large winter bias.

4.3.1.2 Improvement due to MODIS Albedo Update

The adoption of the up-to-date MODIS albedo (Section 4.2.3.2) greatly reduces the relative trend difference in the Midwest during DJF from 5.0% yr^{-1} ("Ocean") to -0.2% yr^{-1} ("MODIS"), the improvement of DJF trend difference is more moderate from 2.0% to -0.2% (Figure 4.7). There are no significant changes of the comparisons in other regions or other seasons. Figure 4.8 shows seasonal albedo relative trends for the 4 regions using coincident with AQS in situ NO_2 data. The OMI DOMINOv2.0 incorporates a climatology albedo dataset (Kleipool et al., 2008) with inputs from the NASA Near-real-time Ice and Snow Extent (NISE) dataset (Boersma et al., 2011). OMI pixel geometry and data availability also affect the albedo data. The noticeable seasonal trend of the OMI DOMINOv2.0 albedo dataset is the 3.9% yr^{-1} increase in DJF of the Midwest and a smaller

DJF increase (1.0%) of the Northeast. In contrast, the MODIS albedo dataset exhibits a smaller positive DJF trend (0.8% yr^{-1}), 3.1% yr^{-1} less than the trend from DOMINOv2.0, in the Midwest, and a small negative DJF trend (-0.8%) in the Northeast. The comparison to the AQS data shows that the MODIS albedo update leads to better agreement between satellite and in suit trends in winter in these regions (Figure 4.7).

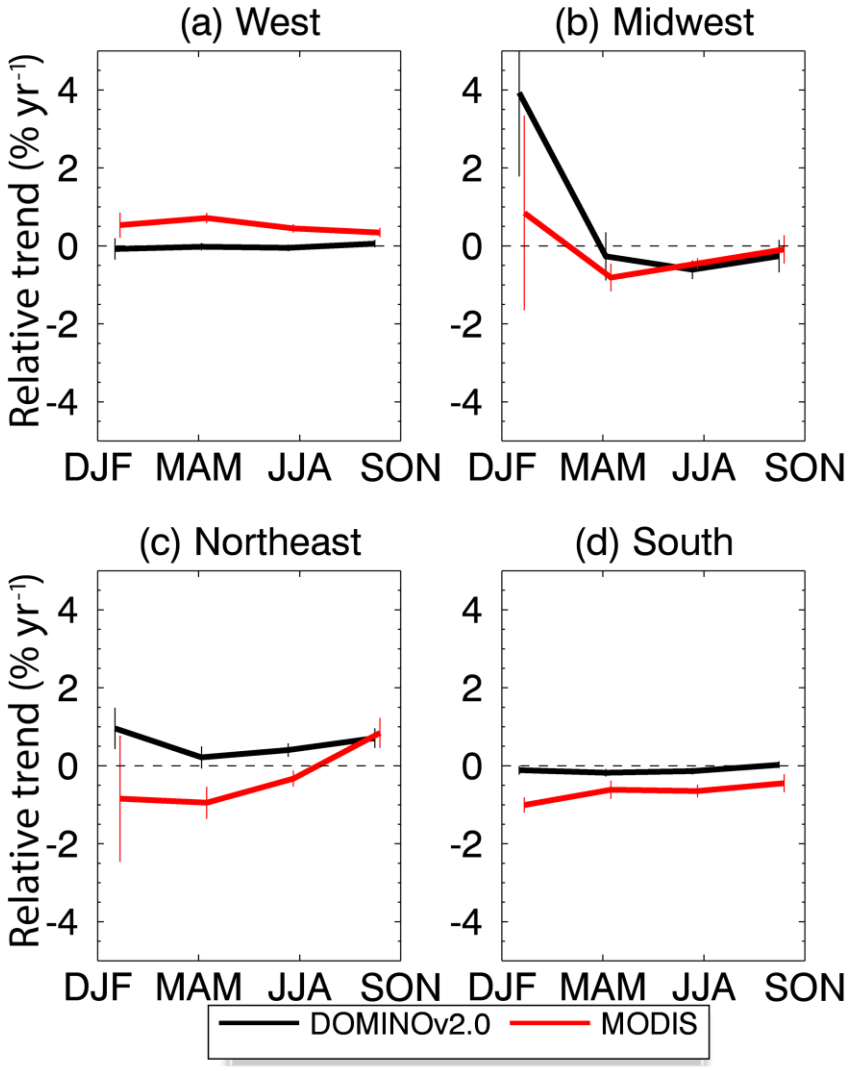

Figure 4.8 Seasonal relative albedo trends of OMI (black line) and MODIS (red line) surface reflectance products, coincident with AQS in situ data used in Figure 4.7. The error bars represent 95% confidence intervals.

4.3.1.3 Improvement due to Lightning Filter

As discussed in Section 4.2.3.3, lightning NOx affects the retrievals of satellite tropospheric NO_2 VCDs. Figure 4.9 shows that the lightning filter significantly reduces the difference of the OMI-based relative trend from that of the AQS data by 0.5-1.4% yr^{-1} in the Northeast and 0.8-1.4% yr^{-1} in the South. As a result, the seasonal trend differences are within 0.5% yr^{-1} in these two regions except during SON. The lightning filter has little effect on the West and Midwest. While lightning NOx can be significant during the monsoon season in some regions of the West (Figure 4.5), the averaged tropospheric NO_2 VCDs are usually less than $1x10^{15}$ molecules cm^{-2} and few data are used in trend analysis. The effect of lightning filter (Figure 4.9) cannot be shown in Figure 4.7 because the coincident OMI and AQS data points are less after applying the lightning filter.

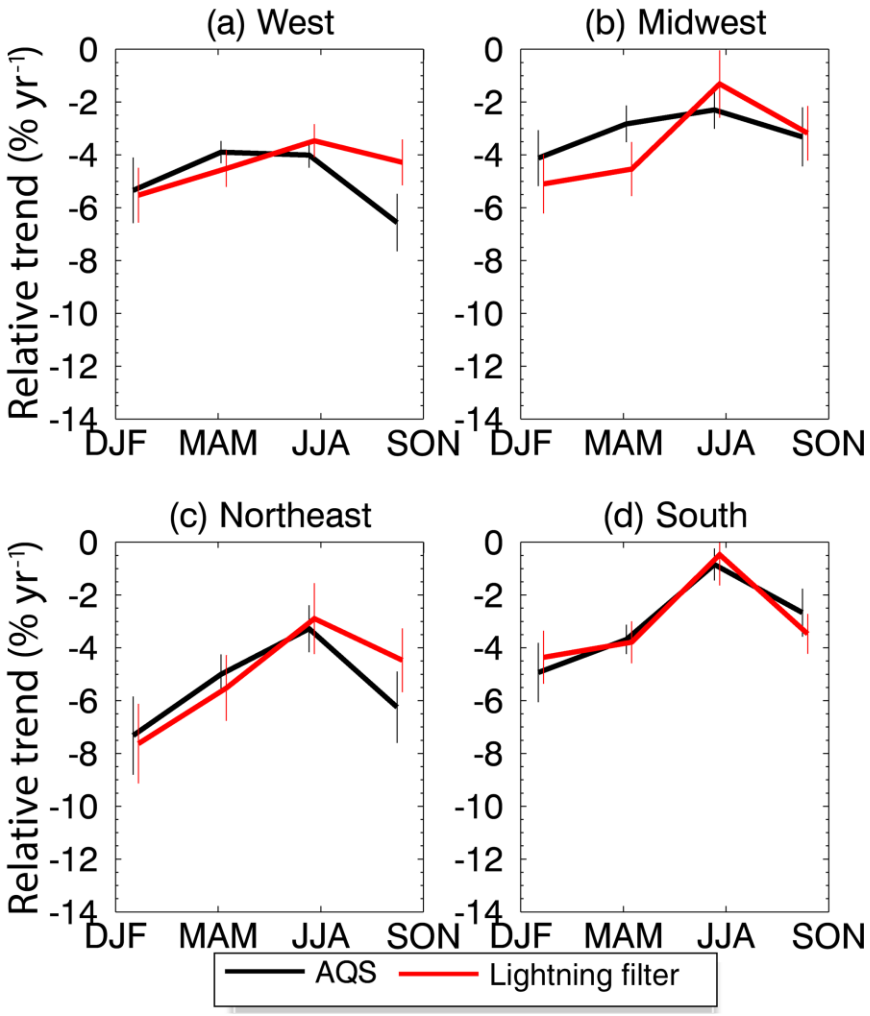

Figure 4.9 Same as Figure 4.7 but for coincident AQS (black line) and OMI data (red line) after applying the lightning filter. The coincident data points are less than used in Figure 4.7 and therefore the AQS trends are not the same.

We examine the improvements of ocean trend removal, MODIS albedo update, and lightning filter by comparing the differences of different OMI-based seasonal relative trends from the AQS in situ trends in Figure 4.10. The previously discussed improvements such as OMI albedo update for DJF Midwest and Northeast are shown. By subtracting the

AQS trends, we can now find clear improvements of lightning filter for the South and Northeast. There remains seasonal variation of OMI-based trend biases relative to in situ data but the discrepancies of the annual trends after the three discussed procedures are relatively small at -0.1% yr^{-1}, -0.7% yr^{-1}, -0.1% yr^{-1}, and -0.1% yr^{-1}, in the West, Midwest, Northeast and South regions, respectively.

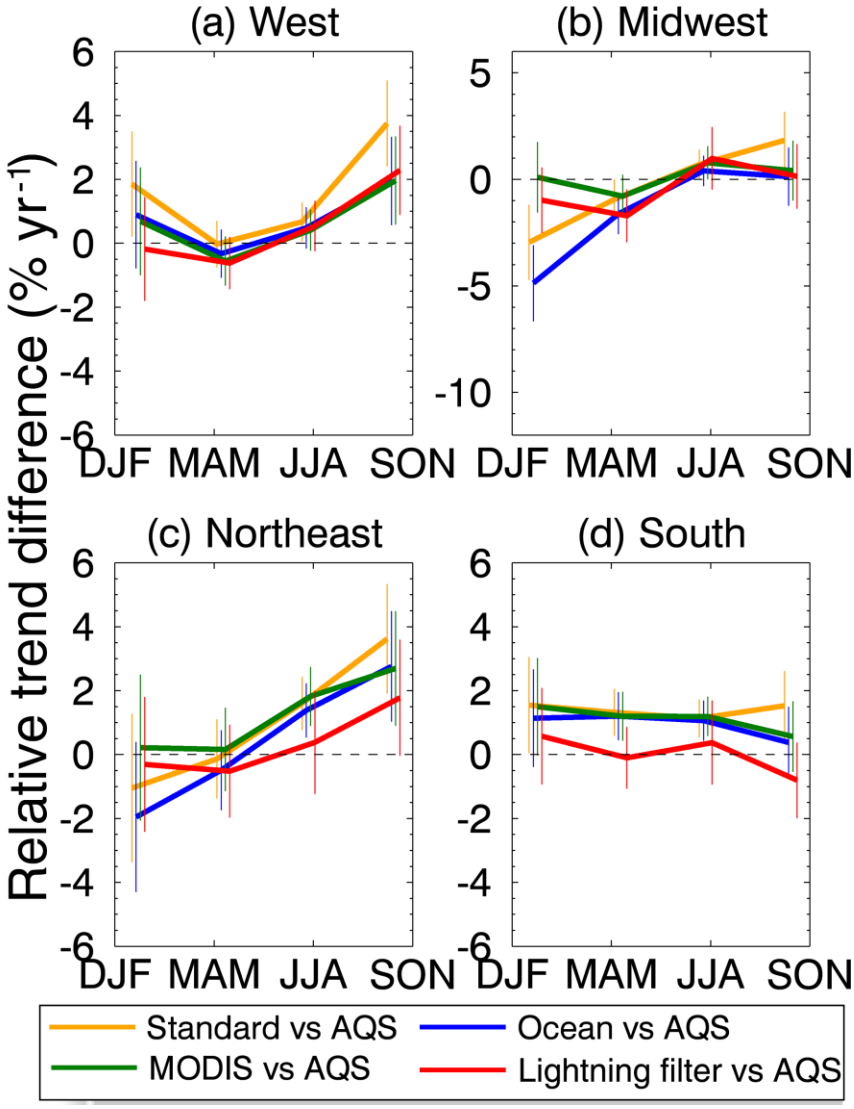

Figure 4.10 Seasonal differences of OMI-based relative trends from those computed from AQS in situ data. The relative trends are shown in Figures 7 and 9.

4.3.2 OMI-based NO_2 Trends

Table 4.1 summarizes the regional annual trends of coincident AQS in situ and OMI data. The "Standard" OMI data (following the DOMINO2 algorithm) tend to show less decreases than AQS data. After applying the three corrections discussed in the previous section in the "lightning filter" OMI data, the agreement with the AQS trends is within the uncertainties of the trends.

Without the lightning filter, AQS decreasing trends are higher (Table 1) while the decreasing trends of OMI data are less (Figure 4.10). The lightning trend in the NLDN data is unclear due in part to the changing instrument sensitivity (Koshak et al., 2015). If lightning NOx is not accounted for in OMI retrieval, tropospheric NO_2 VCDs are overestimated. On the other hand, lightning accompanies low pressure systems which mix the atmosphere vertically and tend to reduce surface NO_2 concentrations when anthropogenic emissions are high such as urban and suburban regions. Therefore, lightning has opposite effects on surface and satellite trends. The low-pressure dilution effect on surface NO_2 concentrations depends on anthropogenic emissions (since the end point of dilution is the background NO_2 value). Therefore, the reduction of decreasing surface trends likely reflects a reduction of low-pressure dilution effect. Similarly, as anthropogenic emissions decrease, the positive bias of tropospheric VCDs due to lightning NOx becomes larger, likely resulting in a reduction of decreasing trends. We consider the lightning effects on surface NO_2 trends to be mostly meteorological driven not by lightning NOx directly (e.g., Ott et al., 2010; Lu et al., 2017) and hence the "lightning filter" data are likely closer to emission related concentration changes.

Table 4.1 Annual relative trends calculated with coincident data and all available data. 95% confidence intervals from Mann-Kendall method are also listed.

Region	Annual relative trends at coincident sites (% yr^{-1})				Annual relative trends using all data (% yr^{-1})			
	Standard		Lightning filter		Standard		Lightning filter	
	AQS	OMI	AQS	OMI	AQS	OMI	AQS	OMI
West	-4.1±0.5	-3.2±0.4	-4.2±0.5	-4.3±0.4	-4.1±0.5	-0.9±0.4	-4.2±0.5	-2.8±0.4
Midwest	-3.4±0.5	-3.6±0.4	-2.8±0.6	-3.6±0.6	-2.5±0.5	-0.9±0.4	-2.2±0.5	-2.4±0.4
Northeast	-5.8±0.5	-5.0±0.5	-5.2±0.6	-5.3±0.7	-4.7±0.5	-3.0±0.4	-4.1±0.5	-3.5±0.5
South	-3.8±0.4	-2.7±0.3	-3.0±0.5	-3.1±0.5	-3.5±0.4	-0.2±0.4	-3.0±0.5	-1.3±0.3
Nationwide	-4.3±0.4	-3.5±0.3	-4.1±0.4	-4.2±0.3	-4.0±0.4	-0.7±0.3	-3.9±0.4	-2.0±0.2

The AQS in situ NO_2 annual relative trends (coincident with "Lightning filter" OMI data) are most significant in the Northeast (-5.2±0.6% yr^{-1}) and West (-4.2±0.5% yr^{-1}), followed by the South (-3.0±0.5% yr^{-1}) and Midwest (-2.8±0.6% yr^{-1}) regions. The nationwide annual trend is -4.1±0.4% yr^{-1}, which are consistent with the previous studies (Lamsal et al., 2015; Lu et al., 2015; Tong et al., 2015; de Foy et al., 2016b; Duncan et al., 2016; Krotkov et al., 2016). The significant NO_2 reductions result from updated technologies and strict regulations (Krotkov, et al., 2016).

The OMI-based NO_2 trends ("Lightning filter" coincident with AQS data) show slightly higher reduction rates in Northeast (-5.3±0.7% yr^{-1}), West (-4.3±0.4% yr^{-1}), the South (-3.1±0.5% yr^{-1}), and Midwest (-3.6±0.6% yr^{-1}) regions. The nationwide annual trend is -4.2±0.3% yr^{-1}.

One advantage of satellite observations over a surface monitoring network is spatial coverage. The corrected OMI data coincident with the AQS data show a similar national annual trend of -4.2±0.3% yr^{-1} similar to the AQS in situ trend of -4.1±0.4% yr^{-1}. Using all data available (Figure 4.11), the corrected OMI data show a much lower trend of -2.0±0.2%yr^{-1}, about half of the AQS trend (-3.9±0.4% yr^{-1}). Figure 4.12 shows that the AQS sites, which are mostly urban and suburban sites, tend to be located in regions with high tropospheric NO_2 VCDs. The OMI decreasing trend with corrected data is a function of tropospheric NO_2 VCDs, increasing from -2% yr^{-1} to -6% yr^{-1} (Figure 4.12). The national annual trend is close to the value of clean regions which are much larger than polluted regions. The larger decrease near the anthropogenic source regions reflect in part the nonlinear photochemistry (Gu et al., 2013) and in part to a stronger influence of NOx sources such as soils in rural regions.

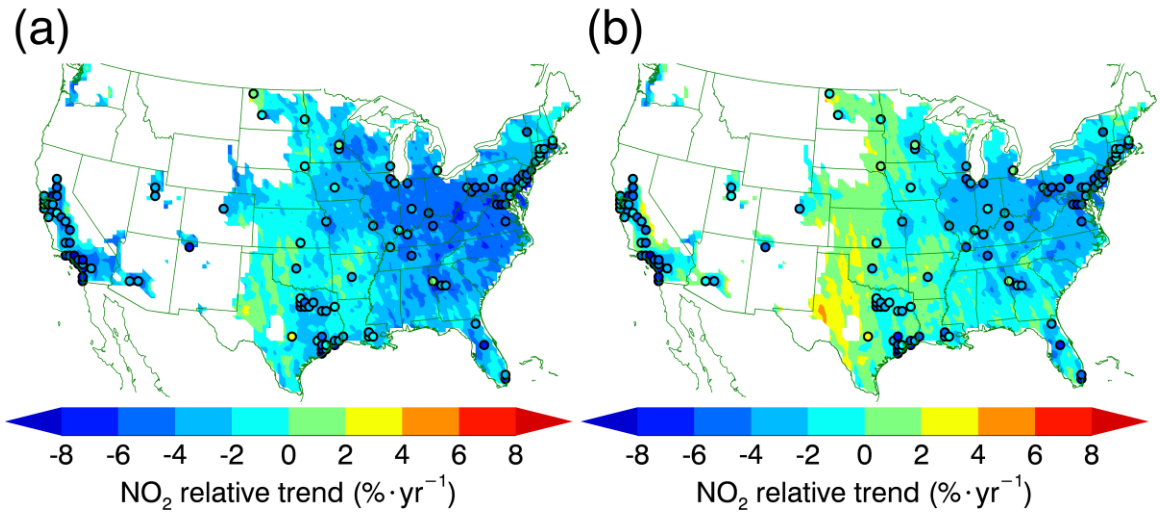

Figure 4.11 Annual relative trends of OMI-based NO_2 for "Standard" (a) and for "Lightning filter" (b) as the colored background. Black bordered circles indicate corresponding AQS NO_2 trends. NO_2 VCD less than $1\times10^{15} molec/cm^2$ is considered missing data and shown in white.

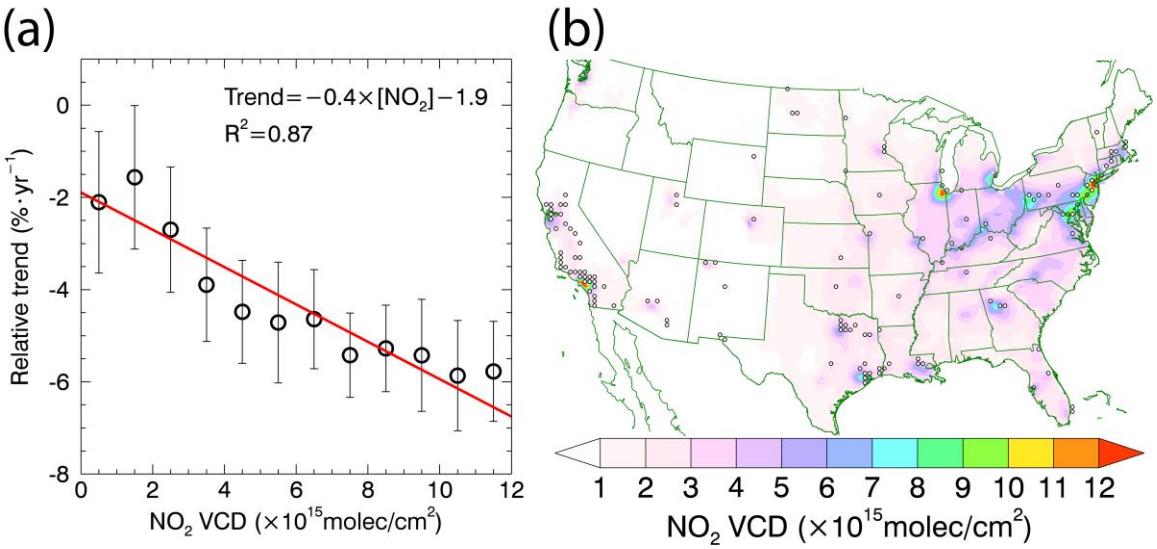

Figure 4.12 (a) OMI-based NO_2 relative trend as a function 2005-2014 averaged OMI tropospheric NO_2 VCD binned every $1\times10^{15} molec/cm^2$. Red line shows a least-squares regression. (b) The distribution of 2005-2014 averaged OMI tropospheric NO_2 VCD. Black bordered circles represent AQS sites. The corrected OMI tropospheric NO_2 data are used.

4.4 Conclusions

Using the DOMINOv2 algorithm, we find that the computed seasonal NO_2 trends greatly underestimate the decreasing trends of the EPA AQS data by up to 3.7% yr^{-1}. We attribute most of the discrepancies to OMI retrievals since the retrieval algorithm was not specifically designed for trend analysis. In this study, we show that removing the background ocean trend (likely a result of sensor noise and drift), adopting MODIS albedo data (with better temporospatial resolutions), and filtering lightning influences can bring OMI tropospheric NO_2 VCD trends in close agreement (<0.8% yr^{-1}) with those of the AQS data. The largest effects of MODIS albedo update are in winter in Midwest and Northeast

and those of lightning filter are in South and Northeast. As our focus is the comparison between OMI-based and in situ NO_2 trends, the ocean trend removal and the lightning filter are also essential in removing the NO_2 trends in the free troposphere, which are not captured by ground-based measurements.

The national annual trend of the corrected OMI data is -2.0±0.2%yr^{-1}, about half of the AQS trend (-3.9±0.4% yr^{-1}). It reflects that the AQS sites are mostly in the urban and suburban regions, where OMI data show much larger decreasing trends than rural regions. The reasons for the dependence of OMI derived trends on tropospheric NO_2 VCDs and the seasonal/regional trend differences are still not understood. Further studies are necessary to improve our understanding of these trends. The observation-based lightning filter implemented in this study is preliminary. Incorporating chemical transport modeling may improve this filter. Inversion studies (e.g., Zhao and Wang, 2009; Gu et al., 2013, 2014, 2016) will be needed to understand the emission changes corresponding to the OMI tropospheric NO_2 VCD trends.

CHAPTER 5. CONCLUSIONS AND FUTURE WORKS

5.1 Summary of Findings

5.1.1 Underestimated Aromatic Emissions in South Asia and the trans-Himalaya Pollution Transport

Using the indirect emission inversion method (Liu et al., 2012a), we find that the low bias of CHOCHO VCDs by REAM is mainly attributed to the underestimation of the bottom-up INTEX-b aromatic emissions by a factor of 2 to 6 over the industrialized Indo-Gangetic Plain. REAM simulated aromatics using the top-down aromatic emissions are compared well (slope: 0.91, R^2: 0.66) with in situ measurements during October 19-24, 2010. Analysis of the meteorology data shows that the air mass flux increases significantly in the presence of the 300hpa cut-off low system. The increasing air mas flux results in evident aromatics transport from the South Asia into the Tibetan Plateau. The results also suggest that other pollutants with long lifetime (>1 day) can also penetrate the natural barrier through this transport pathway. The elevated anthropogenic pollutants can be detrimental to the vulnerable local ecosystem. For example, BC can deposit on glaciers, increase the received solar radiation, and consequently facilitate the melting of the glaciers (He et al., 2014).

REAM underestimates the aromatics during other two periods. The comparison between in situ measured and WRF simulated winds suggests that the discrepancy is due to a missing cut-off low system in the WRF model. This results from the rather scarce

meteorological constraints in this region. Another factor contributing to the model bias is the complex terrains. The coarse model resolution (36km×36km) is inadequate to simulate where topography changes rapidly. The climate models with even lower resolution will further worsen these biases.

5.1.2 NO_2 and NOx Changes in Yangtze River and the U.S.

The HDRI NOx emissions greatly surpass the bottom-up MEIC emission inventory in terms of spatial resolution, and prove powerful in quantifying the effects of urbanization. The HDRI NOx emissions are higher than MEIC NOx emissions by more than 100% in small cities such as Huzhou, Zhoushan, and Xuancheng. The bottom-up approach may have difficulty estimating emissions of smaller cities due to the larger uncertainties in statistics, spatial proxies, and resolution.

Compared to the HDRI method, the averaged satellite NO_2 VCDs ("super-sampling" or "over-sampling") may not serve as good proxies to identify the surface NO_2 hotspots or NOx emission hotspots with high resolution. This results from the transport of NOx and subsequent smoothing of data.

Due to the high economic portion of service sector, Pudong New Area of Shanghai has the smallest NOx emission per GDP with 302±15, 181±7ton yr^{-1} per billion RMB during 2005-2009 and 2010-2015, compared to the regional average of 905±38, 504±16ton yr^{-1} per billion RMB. The rapid development and favorable policies in Pudong New Area result in a 13±5% NOx emission increase, despite the NOx emission reduction of 8±8% in

Shanghai. Hongqiao CBD, the other economic engine of Shanghai, also has increasing NOx emissions.

Although the total coal-fired powerplant capacity in the region increases by about 50%, the total coal-fired powerplant NOx emissions decrease by 6%. This results from the implementation of deNOx systems in coal-fired powerplants, which reduce the NOx emission factors from 2.8±0.2 g/kWh during 2005-2009 to 1.8±0.1g/kWh during 2010-2015. Before 2010, less than 10% of total coal-fired powerplant capacity was equipped with deNOx system in the model region. This number increased to over 60% in 2015. Thus, the reduce NOx emission factors benefit from the increasing implementation of deNOx system. The NOx emission factors from coal-fired powerplants are expected to fall with the increasing installments of deNOx systems in the next few years.

In general, cities with higher GDPs have larger NOx emissions but smaller NOx emissions per GDPs. The comparison between NOx emissions during 2010-2015 and 2005-2009 shows that most smaller cities feature increasing NOx emissions. The HDRI NOx emissions increase by 23±7%, 33±4%, 29±3%, and 23±3% in Wuhu, Ma'anshan, Xuancheng and Tongling, respectively. On the other hand, megacities generally have decreasing NOx emissions, except for Suzhou and Pudong. This is due to the transition from industrialized economy to service-based economy in large cities. Meanwhile small cities feature economic boost in industry sector.

The trend analysis in the U.S. also reveals that the NO_2 changes differ in grids with various NO_2 levels during 2005-2014. The optimized OMI-based NO_2 reduction is a

function of tropospheric NO_2 VCDs, increasing from -2% yr^{-1} to -6% yr^{-1}. In other words, more polluted regions have more NOx reduction. This may be partly explained by the chemical non-linearity (Gu et al., 2013). More polluted regions have longer NOx atmospheric lifetime. If we assume the NOx emission rates are the same for polluted and clean areas alike, the NOx reduction in polluted regions results in larger NOx lifetime decrease than less polluted areas. As a result, NOx emission reduction in polluted areas has more dramatic NO_2 VCDs decrease.

5.1.3 Sources of Discrepancy between OMI-based and In-situ NO_2 Trends

The OMI retrieved tropospheric NO_2 VCDs underestimate seasonal NO_2 reduction rate by up to 3.7% yr^{-1}, compared to coincident EPA AQS in situ measurements. The positive ocean trend observed in the North Pacific may result from sensor noise or row anomalies. The adoption of MODIS albedo data in AMFs calculation improves temporal representativeness, especially in Northeast and Midwest during the wintertime. CTMs have difficulty simulating lightning event due to the temporospatial variance of lightning. The lightning NOx and convection during storms change vertical NO_2 profiles, affect AMFs calculation and subsequently make NO_2 trend less accurate.

Hereby, three procedures are necessary to ensure the quality of the OMI-based NO_2 trends, i.e. removing the background ocean trend, adopting MODIS albedo data, and filtering lightning event. The resulting differences between OMI-based and in situ annual relative trends are negligible in the West, Northeast, and South (<-0.1% yr^{-1}). While the discrepancy in the Midwest is -0.8% yr^{-1}. EPA AQS sites are located in urban and suburban

regions, leaving vast area uncovered. As a result, the national annual trend of the corrected OMI data is -2.0±0.2%yr^{-1}, about half of the AQS trend (-3.9±0.4% yr^{-1}).

5.2 Recommendations for Future Works

5.2.1 Implications for Climate Studies in the Tibetan Plateau

For lack of radiosonde data in the Tibetan Plateau and surrounding areas, assimilated meteorological fields are less accurate. Transport of BC and other pollutants are likely underestimated in the Tibetan Plateau for potential missing cut-off lows. The complex topography in south-eastern Tibet is another challenge for climate models and CTMs. One way to justify whether the meteorological fields are well simulated is to compare simulated and in situ meteorological measurements, such as precipitation, winds, and pressures. Further analysis of reanalysis and climate model simulations is required to quantify the potential model biases and the resulting effect of simulated BC deposition to glaciers on the Tibetan Plateau due to the transport issues we identified in this study.

In addition to trans-Himalaya transport, BC emissions, chemical transformation, and wet deposition also require extensive evaluations with the observations over the Tibetan Plateau and South Asia.

5.2.2 Transport Related Uncertainties in High-resolution Emission Inversion

Previous studies suggest that the inverse emission uncertainties due to transport is negligible when the spatial resolution is coarse (Zhao and Wang, 2009; Gu et al., 2013). Although study implies that the shift of the emission hotspot from the powerplant location

is small (<10km), the transport related uncertainty may be more evident in regions with stronger horizontal winds. Future studies should focus on evaluating this uncertainty by using higher resolution (e.g., 1km×1km) inverse modelling with TROPOMI retrievals.

Since OMI retrievals suffer from row anomalies and subsequent insufficient data, we use the multi-year averaged HDRI emissions in the study. The operation of TROPOMI casts light on the possibility of more frequent and operational inverse emissions.

5.2.3 Future NO_2 Trend Analysis Recommendations

Future analysis on NO_2 trend should implement the discussed three procedures to minimize uncertainties from retrieval, especially in developing regions without long-term and high-coverage in situ NO_2 measurements.

There are two derivative problems following this research, as follows.

5.2.3.1 Overestimated NO_2 Reduction Trend in Midwest of the U.S.

The discrepancy between optimized OMI-based and in situ annual relative trends in Midwest remains -0.8% yr^{-1}. The cause of this disagreement is yet to be studied. One possible explanation is that the data becomes insufficient after the lightning filter, given that the discrepancy is -0.2% yr^{-1} before the lightning filter and after the ocean trend removal and MODIS albedo update. The rapid changes of NOx emissions consequently introduce NO_2 profile changes, affecting the AMF calculation. Inversion studies (e.g., Zhao and Wang, 2009; Gu et al., 2013, 2014, 2016) will be needed to understand the effects of emission changes on OMI-based trends.

5.2.3.2 Increasing NO_2 Reduction with Higher NO_2 VCDs

The NO_2 reduction rates are found to be linearly and positively correlated with tropospheric NO_2 VCDs. This could attribute to the chemical non-linearity (Gu et al., 2013), which makes reduction in polluted areas more evident. Future studies should focus on the nature of this relationship to quantify the effectiveness of emission reduction.

REFERENCES

Alvarado, L. M. A., Richter, A., Vrekoussis, M., Wittrock, F., Hilboll, A., Schreier, S. F., and Burrows, J. P.: An improved glyoxal retrieval from OMI measurements, Atmospheric Measurement Techniques, 7, 4133-4150, 10.5194/amt-7-4133-2014, 2014.

Alvarado, L. M. A.: Investigating the role of glyoxal using satellite and MAX-DOAS measurements, Ph.D. thesis, University of Bremen, http://elib.suub.uni-bremen.de/edocs/00105347-1.pdf, 2016

Andreae, M. O., and Merlet, P.: Emission of trace gases and aerosols from biomass burning, Global Biogeochemical Cycles, 15, 955-966, 10.1029/2000GB001382, 2001.

Atkinson, R.: Atmospheric chemistry of VOCs and NOx, Atmospheric Environment, 34, 2063-2101, 10.1016/S1352-2310(99)00460-4, 2000.

Balk, D. L., Deichmann, U., Yetman, G., Pozzi, F., Hay, S. I., and Nelson, A.: Determining Global Population Distribution: Methods, Applications and Data, Advances in Parasitology, 62, 119-156, 2006.

Barnett, T. P., Adam, J. C., and Lettenmaier, D. P.: Potential impacts of a warming climate on water availability in snow-dominated regions, Nature, 438, 303-309, 2005.

Beirle, S., Boersma, K. F., Platt, U., Lawrence, M. G., and Wagner, T.: Megacity Emissions and Lifetimes of Nitrogen Oxides Probed from Space, Science, 333, 1737-1739, 10.1126/science.1207824, 2011.

Bey, I., Jacob, D. J., Yantosca, R. M., Logan, J. A., Field, B. D., Fiore, A. M., Li, Q. B., Liu, H. G. Y., Mickley, L. J., and Schultz, M. G.: Global modeling of tropospheric chemistry with assimilated meteorology: Model description and evaluation, Journal of Geophysical Research-Atmospheres,106, 23073-23095, 10.1029/2001jd000807, 2001.

Boersma, K. F., Eskes, H. J., and Brinksma, E. J.: Error analysis for tropospheric NO2 retrieval from space, Journal of Geophysical Research: Atmospheres, 109, 10.1029/2003JD003962, 2004.

Boersma, K. F., Eskes, H. J., Veefkind, J. P., Brinksma, E. J., van der A, R. J., Sneep, M., van den Oord, G. H. J., Levelt, P. F., Stammes, P., Gleason, J. F., and Bucsela, E. J.: Near-real time retrieval of tropospheric NO2 from OMI, Atmospheric Chemistry and Physics, 7, 2103-2118, 10.5194/acp-7-2103-2007, 2007.

Boersma, K. F., Eskes, H. J., Dirksen, R. J., van der A, R. J., Veefkind, J. P., Stammes, P., Huijnen, V., Kleipool, Q. L., Sneep, M., Claas, J., Leitão, J., Richter, A., Zhou, Y., and Brunner, D.: An improved tropospheric NO2 column retrieval algorithm for the Ozone Monitoring Instrument, Atmospheric Measurement Techniques, 4, 1905-1928, 10.5194/amt-4-1905-2011, 2011.

Bond, T. C., Bhardwaj, E., Dong, R., Jogani, R., Jung, S., Roden, C., Streets, D. G., and Trautmann, N. M.: Historical emissions of black and organic carbon aerosol from energy-related combustion, 1850–2000, Global Biogeochemical Cycles, 21, 10.1029/2006GB002840, 2007.

Bovensmann, H., Burrows, J. P., Buchwitz, M., Frerick, J., Noël, S., Rozanov, V. V., Chance, K. V., and Goede, A. P. H.: SCIAMACHY: Mission Objectives and Measurement Modes, Journal of the Atmospheric Sciences, 56, 127-150, doi:10.1175/1520-0469(1999)056<0127:SMOAMM>2.0.CO;2, 1999.

Bucsela, E. J., Pickering, K. E., Huntemann, T. L., Cohen, R. C., Perring, A., Gleason, J. F., Blakeslee, R. J., Albrecht, R. I., Holzworth, R., Cipriani, J. P., Vargas-Navarro, D., Mora-Segura, I., Pacheco-Hernández, A., and Laporte-Molina, S.: Lightning-generated NOx seen by the Ozone Monitoring Instrument during NASA's Tropical Composition, Cloud and Climate Coupling Experiment (TC4), Journal of Geophysical Research: Atmospheres, 115, 10.1029/2009JD013118, 2010.

Burrows, J. P., Hölzle, E., Goede, A. P. H., Visser, H., and Fricke, W.: Earth ObservationSCIAMACHY—scanning imaging absorption spectrometer for atmospheric chartography, Acta Astronautica, 35, 445-451, 10.1016/0094-5765(94)00278-T, 1995.

Cabrera-Perez, D., Taraborrelli, D., Sander, R., and Pozzer, A.: Global atmospheric budget of simple monocyclic aromatic compounds, Atmospheric Chemistry and Physics, 16, 6931-6947, 10.5194/acp-16-6931-2016, 2016.

Cagliari, J., Fedrizzi, F., Rodrigues Finotti, A., Echevenguá Teixeira, C., and do Nascimento Filho, I.: Volatilization of monoaromatic compounds (benzene, toluene, and xylenes; BTX) from gasoline: Effect of the ethanol, Environmental Toxicology and Chemistry, 29, 808-812, 10.1002/etc.111, 2010.

Castellanos, P., and Boersma, K. F.: Reductions in nitrogen oxides over Europe driven by environmental policy and economic recession, Scientific Reports, 2, 265, 10.1038/srep00265, 2012.

Central People's Government of the People's Republic of China: "12th Five-Year-Plan" on Energy Conservation and Emission Reduction, China, 2012.

Cheng, Y., Wang, Y., Zhang, Y., Chen, G., Crawford, J. H., Kleb, M. M., Diskin, G. S., and Weinheimer, A. J.: Large biogenic contribution to boundary layer O3-CO regression slope in summer, Geophysical Research Letters, 44, 7061-7068, 10.1002/2017GL074405, 2017.

China Electricity Council: China Electrical Power Industry Statistics, (2005–2015), China Power Press, Beijing, China, 2015.

Choi, Y., Wang, Y., Zeng, T., Martin, R. V., Kurosu, T. P., and Chance, K.: Evidence of lightning NOx and convective transport of pollutants in satellite observations over North America, Geophysical Research Letters, 32, L02805, 10.1029/2004GL021436, 2005.

Choi, Y., Wang, Y., Zeng, T., Cunnold, D., Yang, E. S., Martin, R., Chance, K., Thouret, V., and Edgerton, E.: Springtime transitions of NO2, CO, and O-3 over North America: Model evaluation and analysis, Journal of Geophysical Research-Atmospheres,113, 16, 10.1029/2007jd009632, 2008a.

Choi, Y., Wang, Y., Yang, Q., Cunnold, D., Zeng, T., Shim, C., Luo, M., Eldering, A., Bucsela, E., and Gleason, J.: Spring to summer northward migration of high O3 over the western North Atlantic, Geophysical Research Letters, 35, L04818, 10.1029/2007GL032276, 2008b.

CIESIN (Center for International Earth Science Information Network), C. C. U., International Food Policy Research Institute, I., The World, B., and Centro Internacional de Agricultura Tropical, C.: Global Rural-Urban Mapping Project, Version 1 (GRUMPv1): Population Density Grid, NASA Socioeconomic Data and Applications Center (SEDAC), Palisades, NY, doi: 10.7927/H4R20Z93, 2011.

CIESIN (Center for International Earth Science Information Network), C. C. U.: Gridded Population of the World, Version 4 (GPWv4): Population Density Adjusted to Match 2015 Revision UN WPP Country Totals, NASA Socioeconomic Data and Applications Center (SEDAC), Palisades, NY, doi: 10.7927/H4HX19NJ, 2016.

Cong, Z., Kang, S., Gao, S., Zhang, Y., Li, Q., and Kawamura, K.: Historical Trends of Atmospheric Black Carbon on Tibetan Plateau As Reconstructed from a 150-Year Lake Sediment Record, Environmental Science & Technology, 47, 2579-2586, 10.1021/es3048202, 2013.

Cong, Z., Kawamura, K., Kang, S., and Fu, P.: Penetration of biomass-burning emissions from South Asia through the Himalayas: new insights from atmospheric organic acids, Sci. Rep., 5, 10.1038/srep09580, 2015.

Cui, Y., Lin, J., Song, C., Liu, M., Yan, Y., Xu, Y., and Huang, B.: Rapid growth in nitrogen dioxide pollution over Western China, 2005–2013, Atmospheric Chemistry and Physics, 16, 6207-6221, 10.5194/acp-16-6207-2016, 2016.

Cummins, K. L., and Murphy, M. J.: An Overview of Lightning Locating Systems: History, Techniques, and Data Uses, With an In-Depth Look at the U.S. NLDN, IEEE Transactions on Electromagnetic Compatibility, 51, 499-518, 10.1109/TEMC.2009.2023450, 2009.

de Foy, B., Lu, Z., and Streets, D. G.: Impacts of control strategies, the Great Recession and weekday variations on NO2 columns above North American cities, Atmospheric Environment, 138, 74-86, j.atmosenv.2016.04.038, 2016a.

de Foy, B., Lu, Z., and Streets, D. G.: Satellite NO2 retrievals suggest China has exceeded its NOx reduction goals from the twelfth Five-Year Plan, Scientific Reports, 6, 35912, 10.1038/srep35912, 2016b.

Demerjian, K. L.: A review of national monitoring networks in North America, Atmospheric Environment, 34, 1861-1884, 10.1016/S1352-2310(99)00452-5, 2000.

Ding, J., van der A, R. J., Mijling, B., and Levelt, P. F.: Space-based NOx emission estimates over remote regions improved in DECSO, Atmospheric Measurement Techniques, 10, 925-938, 10.5194/amt-10-925-2017, 2017.

Dumka, U. C., Moorthy, K. K., Kumar, R., Hegde, P., Sagar, R., Pant, P., Singh, N., and Babu, S. S.: Characteristics of aerosol black carbon mass concentration over a high altitude location in the Central Himalayas from multi-year measurements, Atmospheric Research96, 510-521, 10.1016/j.atmosres.2009.12.010, 2010.

Duncan, B. N., Lamsal, L. N., Thompson, A. M., Yoshida, Y., Lu, Z., Streets, D. G., Hurwitz, M. M., and Pickering, K. E.: A space-based, high-resolution view of notable changes in urban NOx pollution around the world (2005–2014), Journal of Geophysical Research: Atmospheres, 121, 976-996, 10.1002/2015JD024121, 2016.

Eskes, H. J., and Boersma, K. F.: Averaging kernels for DOAS total-column satellite retrievals, Atmospheric Chemistry and Physics, 3, 1285-1291, 10.5194/acp-3-1285-2003, 2003.

Fu, T.-M., Jacob, D. J., Wittrock, F., Burrows, J. P., Vrekoussis, M., and Henze, D. K.: Global budgets of atmospheric glyoxal and methylglyoxal, and implications for formation of secondary organic aerosols, Journal of Geophysical Research, 113, 10.1029/2007jd009505, 2008.

Gray, B. A., Wang, Y., Gu, D., Bandy, A., Mauldin, L., Clarke, A., Alexander, B., and Davis, D. D.: Sources, transport, and sinks of SO2 over the equatorial Pacific during the Pacific Atmospheric Sulfur Experiment, Journal of Atmospheric Chemistry, 68, 27-53, 10.1007/s10874-010-9177-7, 2011.

Gu, D. S., Wang, Y. H., Smeltzer, C., and Liu, Z.: Reduction in NOx Emission Trends over China: Regional and Seasonal Variations, Environmental Science & Technology, 47, 12912-12919, 10.1021/es401727e, 2013.

Gu, D., Wang, Y., Smeltzer, C., and Boersma, K. F.: Anthropogenic emissions of NOx over China: Reconciling the difference of inverse modeling results using GOME-

2 and OMI measurements, Journal of Geophysical Research: Atmospheres, 119, 2014JD021644, 10.1002/2014JD021644, 2014.

Gu, D., Wang, Y., Yin, R., Zhang, Y., and Smeltzer, C.: Inverse modelling of NOx emissions over eastern China: uncertainties due to chemical non-linearity, Atmospheric Measurement Techniques, 9, 5193-5201, 10.5194/amt-9-5193-2016, 2016.

Guenther, A. B., Jiang, X., Heald, C. L., Sakulyanontvittaya, T., Duhl, T., Emmons, L. K., and Wang, X.: The Model of Emissions of Gases and Aerosols from Nature version 2.1 (MEGAN2.1): an extended and updated framework for modeling biogenic emissions, Geosci. Model Dev., 5, 1471-1492, 10.5194/gmd-5-1471-2012, 2012.

Hansen, J., and Nazarenko, L.: Soot climate forcing via snow and ice albedos, Proceedings of the National Academy of Sciences of the United States of America, 101, 423-428, 10.1073/pnas.2237157100, 2004.

He, C., Li, Q. B., Liou, K. N., Zhang, J., Qi, L., Mao, Y., Gao, M., Lu, Z., Streets, D. G., Zhang, Q., Sarin, M. M., and Ram, K.: A global 3-D CTM evaluation of black carbon in the Tibetan Plateau, Atmospheric Chemistry and Physics, 14, 7091-7112, 10.5194/acp-14-7091-2014, 2014.

Heckel, A., Kim, S. W., Frost, G. J., Richter, A., Trainer, M., and Burrows, J. P.: Influence of low spatial resolution a priori data on tropospheric NO2 satellite retrievals, Atmospheric Measurement Techniques, 4, 1805-1820, 10.5194/amt-4-1805-2011, 2011.

Henze, D. K., Seinfeld, J. H., Ng, N. L., Kroll, J. H., Fu, T. M., Jacob, D. J., and Heald, C. L.: Global modeling of secondary organic aerosol formation from aromatic hydrocarbons: high- vs. low-yield pathways, Atmospheric Chemistry and Physics, 8, 2405-2420, 10.5194/acp-8-2405-2008, 2008.

Hindman, E. E., and Upadhyay, B. P.: Air pollution transport in the Himalayas of Nepal and Tibet during the 1995–1996 dry season, Atmospheric Environment, 36, 727-739, 10.1016/S1352-2310(01)00495-2, 2002.

Hoskins, B. J., McIntyre, M. E., and Robertson, A. W.: On the use and significance of isentropic potential vorticity maps, Quarterly Journal of the Royal Meteorological Society, 111, 877-946, 10.1002/qj.49711147002, 1985.

Ji, Z., Kang, S., Cong, Z., Zhang, Q., and Yao, T.: Simulation of carbonaceous aerosols over the Third Pole and adjacent regions: distribution, transportation, deposition, and climatic effects, Climate Dynamics, 45, 2831-2846, 10.1007/s00382-015-2509-1, 2015.

Kain, J. S., and Fritsch, J. M.: Convective Parameterization for Mesoscale Models: The Kain-Fritsch Scheme, in: The Representation of Cumulus Convection in Numerical Models, edited by: Emanuel, K. A., and Raymond, D. J., American Meteorological Society, Boston, MA, 165-170, 1993.

Kang, S., Huang, J., Wang, F., Zhang, Q., Zhang, Y., Li, C., Wang, L., Chen, P., Sharma, C. M., Li, Q., Sillanpää, M., Hou, J., Xu, B., and Guo, J.: Atmospheric Mercury Depositional Chronology Reconstructed from Lake Sediments and Ice Core in the Himalayas and Tibetan Plateau, Environmental Science & Technology, 50, 2859-2869, 10.1021/acs.est.5b04172, 2016.

Kehrwald, N. M., Thompson, L. G., Tandong, Y., Mosley-Thompson, E., Schotterer, U., Alfimov, V., Beer, J., Eikenberg, J., and Davis, M. E.: Mass loss on Himalayan glacier endangers water resources, Geophysical Research Letters, 35, 10.1029/2008GL035556, 2008.

Kendall, M. G.: Rank correlation methods, Rank correlation methods., Griffin, Oxford, England, 1948.

Kleipool, Q. L., Dobber, M. R., de Haan, J. F., and Levelt, P. F.: Earth surface reflectance climatology from 3 years of OMI data, Journal of Geophysical Research: Atmospheres, 113, 10.1029/2008JD010290, 2008.

Kopacz, M., Mauzerall, D. L., Wang, J., Leibensperger, E. M., Henze, D. K., and Singh, K.: Origin and radiative forcing of black carbon transported to the Himalayas and Tibetan Plateau, Atmospheric Chemistry and Physics, 11, 2837-2852, 10.5194/acp-11-2837-2011, 2011.

Koshak, W., Peterson, H., Biazar, A., Khan, M., and Wang, L.: The NASA Lightning Nitrogen Oxides Model (LNOM): Application to air quality modeling, Atmospheric Research135–136, 363-369, 10.1016/j.atmosres.2012.12.015, 2014.

Koshak, W. J., Cummins, K. L., Buechler, D. E., Vant-Hull, B., Blakeslee, R. J., Williams, E. R., and Peterson, H. S.: Variability of CONUS Lightning in 2003–12 and Associated Impacts, J Appl Meteorol Clim, 54, 15-41, 10.1175/jamc-d-14-0072.1, 2015.

Krotkov, N., Herman, J., Bhartia, P. K., Seftor, C., Arola, A., Kaurola, J., Koskinen, L., Kalliskota, S., Taalas, P., and Geogdzhaev, I.: Version 2 TOMS UV algorithm: problems and enhancements, in: P Soc Photo-Opt Ins, edited by: Slusser, J. R., Herman, J. R., and Gao, W., Proceedings of the Society of Photo-Optical Instrumentation Engineers (Spie), Spie-Int Soc Optical Engineering, Bellingham, 82-93, 2002.

Krotkov, N. A., McLinden, C. A., Li, C., Lamsal, L. N., Celarier, E. A., Marchenko, S. V., Swartz, W. H., Bucsela, E. J., Joiner, J., Duncan, B. N., Boersma, K. F., Veefkind, J. P., Levelt, P. F., Fioletov, V. E., Dickerson, R. R., He, H., Lu, Z., and Streets, D. G.: Aura OMI observations of regional SO2 and NO2 pollution changes from 2005 to 2015, Atmospheric Chemistry and Physics, 16, 4605-4629, 10.5194/acp-16-4605-2016, 2016.

Kumar, R., Barth, M. C., Pfister, G. G., Nair, V. S., Ghude, S. D., and Ojha, N.: What controls the seasonal cycle of black carbon aerosols in India?, Journal of Geophysical Research: Atmospheres, 120, 7788-7812, 10.1002/2015JD023298, 2015.

Lamsal, L. N., Martin, R. V., van Donkelaar, A., Steinbacher, M., Celarier, E. A., Bucsela, E., Dunlea, E. J., and Pinto, J. P.: Ground-level nitrogen dioxide concentrations inferred from the satellite-borne Ozone Monitoring Instrument, Journal of Geophysical Research: Atmospheres, 113, 10.1029/2007JD009235, 2008.

Lamsal, L. N., Martin, R. V., van Donkelaar, A., Celarier, E. A., Bucsela, E. J., Boersma, K. F., Dirksen, R., Luo, C., and Wang, Y.: Indirect validation of tropospheric nitrogen dioxide retrieved from the OMI satellite instrument: Insight into the seasonal variation of nitrogen oxides at northern midlatitudes, Journal of Geophysical Research: Atmospheres, 115, 10.1029/2009JD013351, 2010.

Lamsal, L. N., Duncan, B. N., Yoshida, Y., Krotkov, N. A., Pickering, K. E., Streets, D. G., and Lu, Z.: U.S. NO2 trends (2005–2013): EPA Air Quality System (AQS) data versus improved observations from the Ozone Monitoring Instrument (OMI), Atmospheric Environment, 110, 130-143, j.atmosenv.2015.03.055, 2015.

Laughner, J. L., Zare, A., and Cohen, R. C.: Effects of daily meteorology on the interpretation of space-based remote sensing of NO2, Atmospheric Chemistry and Physics, 16, 15247-15264, 10.5194/acp-16-15247-2016, 2016.

Lawrence, M. G., and Lelieveld, J.: Atmospheric pollutant outflow from southern Asia: a review, Atmospheric Chemistry and Physics, 10, 11017-11096, 10.5194/acp-10-11017-2010, 2010.

Lerot, C., Stavrakou, T., De Smedt, I., Muller, J. F., and Van Roozendael, M.: Glyoxal vertical columns from GOME-2 backscattered light measurements and comparisons with a global model, Atmospheric Chemistry and Physics, 10, 12059-12072, 10.5194/acp-10-12059-2010, 2010.

Li, C., Bosch, C., Kang, S., Andersson, A., Chen, P., Zhang, Q., Cong, Z., Chen, B., Qin, D., and Gustafsson, Ö.: Sources of black carbon to the Himalayan–Tibetan Plateau glaciers, Nature Communications, 7, 12574, 10.1038/ncomms12574, 2016.

Li, M., Zhang, Q., Streets, D. G., He, K. B., Cheng, Y. F., Emmons, L. K., Huo, H., Kang, S. C., Lu, Z., Shao, M., Su, H., Yu, X., and Zhang, Y.: Mapping Asian anthropogenic emissions of non-methane volatile organic compounds to multiple chemical mechanisms, Atmospheric Chemistry and Physics, 14, 5617-5638, 10.5194/acp-14-5617-2014, 2014.

Li, M., Zhang, Q., Kurokawa, J., Woo, J. H., He, K. B., Lu, Z., Ohara, T., Song, Y., Streets, D. G., Carmichael, G. R., Cheng, Y. F., Hong, C. P., Huo, H., Jiang, X. J., Kang, S. C., Liu, F., Su, H., and Zheng, B.: MIX: a mosaic Asian anthropogenic emission inventory for the MICS-Asia and the HTAP projects, Atmos. Chem. Phys. Discuss., 2015, 34813-34869, 10.5194/acpd-15-34813-2015, 2015.

Li, H., He, Q., Song, Q., Chen, L., Song, Y., Wang, Y., Lin, K., Xu, Z., and Shao, M.: Diagnosing Tibetan pollutant sources via volatile organic compound observations, Atmospheric Environment, 166, 244-254, 10.1016/j.atmosenv.2017.07.031, 2017.

Lin, J.-T., Pan, D., and Zhang, R.-X.: Trend and Interannual Variability of Chinese Air Pollution since 2000 in Association with Socioeconomic Development: A Brief Overview, Atmospheric and Oceanic Science Letters, 6, 84-89, 10.1080/16742834.2013.11447061, 2013.

Lin, J. T., McElroy, M. B., and Boersma, K. F.: Constraint of anthropogenic NOx emissions in China from different sectors: a new methodology using multiple satellite retrievals, Atmospheric Chemistry and Physics, 10, 63-78, 10.5194/acp-10-63-2010, 2010.

Lin, J. T., and McElroy, M. B.: Detection from space of a reduction in anthropogenic emissions of nitrogen oxides during the Chinese economic downturn, Atmospheric Chemistry and Physics, 11, 8171-8188, 10.5194/acp-11-8171-2011, 2011.

Lin, J. T., Liu, Z., Zhang, Q., Liu, H., Mao, J., and Zhuang, G.: Modeling uncertainties for tropospheric nitrogen dioxide columns affecting satellite-based inverse modeling of nitrogen oxides emissions, Atmospheric Chemistry and Physics, 12, 12255-12275, 10.5194/acp-12-12255-2012, 2012.

Lin, J. T., Martin, R. V., Boersma, K. F., Sneep, M., Stammes, P., Spurr, R., Wang, P., Van Roozendael, M., Clémer, K., and Irie, H.: Retrieving tropospheric nitrogen dioxide from the Ozone Monitoring Instrument: effects of aerosols, surface reflectance anisotropy, and vertical profile of nitrogen dioxide, Atmospheric Chemistry and Physics, 14, 1441-1461, 10.5194/acp-14-1441-2014, 2014.

Lin, J. T., Liu, M. Y., Xin, J. Y., Boersma, K. F., Spurr, R., Martin, R., and Zhang, Q.: Influence of aerosols and surface reflectance on satellite NO2 retrieval: seasonal and spatial characteristics and implications for NOx emission constraints, Atmospheric Chemistry and Physics, 15, 11217-11241, 10.5194/acp-15-11217-2015, 2015.

Liu, F., Zhang, Q., van der A, R. J., Zheng, B., Tong, D., Yan, L., Zheng, Y., and He, K.: Recent reduction in NO x emissions over China: synthesis of satellite observations and emission inventories, Environmental Research Letters, 11, 114002, 2016.

Liu, F., Beirle, S., Zhang, Q., van der A, R. J., Zheng, B., Tong, D., and He, K.: NO2 emission trends over Chinese cities estimated from OMI observations during 2005 to 2015, Atmos. Chem. Phys. Discuss., 2017, 1-21, 10.5194/acp-2017-369, 2017.

Liu, Z., Wang, Y., Gu, D., Zhao, C., Huey, L. G., Stickel, R., Liao, J., Shao, M., Zhu, T., Zeng, L., Liu, S.-C., Chang, C.-C., Amoroso, A., and Costabile, F.: Evidence of Reactive Aromatics As a Major Source of Peroxy Acetyl Nitrate over China, Environmental Science & Technology, 44, 7017-7022, 10.1021/es1007966, 2010.

Liu, Z., Wang, Y., Vrekoussis, M., Richter, A., Wittrock, F., Burrows, J. P., Shao, M., Chang, C.-C., Liu, S.-C., Wang, H., and Chen, C.: Exploring the missing source of glyoxal (CHOCHO) over China, Geophysical Research Letters, 39, L10812, 10.1029/2012GL051645, 2012a.

Liu, Z., Wang, Y., Gu, D., Zhao, C., Huey, L. G., Stickel, R., Liao, J., Shao, M., Zhu, T., Zeng, L., Amoroso, A., Costabile, F., Chang, C. C., and Liu, S. C.: Summertime photochemistry during CAREBeijing-2007: ROx budgets and O3 formation, Atmospheric Chemistry and Physics, 12, 7737-7752, 10.5194/acp-12-7737-2012, 2012b.

Liu, Z., Wang, Y., Costabile, F., Amoroso, A., Zhao, C., Huey, L. G., Stickel, R., Liao, J., and Zhu, T.: Evidence of Aerosols as a Media for Rapid Daytime HONO Production over China, Environmental Science & Technology, 48, 14386-14391, 10.1021/es504163z, 2014.

Lu, Z., Streets, D. G., Zhang, Q., and Wang, S.: A novel back-trajectory analysis of the origin of black carbon transported to the Himalayas and Tibetan Plateau during 1996–2010, Geophysical Research Letters, 39, 10.1029/2011GL049903, 2012.

Lu, Z., Streets, D. G., de Foy, B., Lamsal, L. N., Duncan, B. N., and Xing, J.: Emissions of nitrogen oxides from US urban areas: estimation from Ozone Monitoring Instrument retrievals for 2005–2014, Atmospheric Chemistry and Physics, 15, 10367-10383, 10.5194/acp-15-10367-2015, 2015.

Luo, C., Wang, Y., and Koshak, W. J.: Development of a self-consistent lightning NOx simulation in large-scale 3-D models, Journal of Geophysical Research: Atmospheres, 122, 3141-3154, 10.1002/2016JD026225, 2017.

Lüthi, Z. L., Škerlak, B., Kim, S. W., Lauer, A., Mues, A., Rupakheti, M., and Kang, S.: Atmospheric brown clouds reach the Tibetan Plateau by crossing the Himalayas, Atmospheric Chemistry and Physics, 15, 6007-6021, 10.5194/acp-15-6007-2015, 2015.

Lutz, A. F., Immerzeel, W. W., Shrestha, A. B., and Bierkens, M. F. P.: Consistent increase in High Asia's runoff due to increasing glacier melt and precipitation, Nature Clim. Change, 4, 587-592, 10.1038/nclimate2237, 2014.

Lv, W. Y., Tang, Y. L., and Fang, Z.: Outline of optimization of thermal power structures and study on technical upgrading in China, Electr. Power Constr., 23, 9, 2002.

Mann, H. B.: NONPARAMETRIC TESTS AGAINST TREND, Econometrica, 13, 245-259, 10.2307/1907187, 1945.

Martin, R. V., Jacob, D. J., Chance, K., Kurosu, T. P., Palmer, P. I., and Evans, M. J.: Global inventory of nitrogen oxide emissions constrained by space-based observations of NO2 columns, Journal of Geophysical Research: Atmospheres, 108, 10.1029/2003JD003453, 2003.

Martin, R. V., Sauvage, B., Folkins, I., Sioris, C. E., Boone, C., Bernath, P., and Ziemke, J.: Space-based constraints on the production of nitric oxide by lightning, Journal of Geophysical Research: Atmospheres, 112, 10.1029/2006JD007831, 2007.

Maussion, F., Scherer, D., Finkelnburg, R., Richters, J., Yang, W., and Yao, T.: WRF simulation of a precipitation event over the Tibetan Plateau, China – an assessment using remote sensing and ground observations, Hydrol. Earth Syst. Sci., 15, 1795-1817, 10.5194/hess-15-1795-2011, 2011.

Ménégoz, M., Gallée, H., and Jacobi, H. W.: Precipitation and snow cover in the Himalaya: from reanalysis to regional climate simulations, Hydrol. Earth Syst. Sci., 17, 3921-3936, 10.5194/hess-17-3921-2013, 2013.

Menon, S., Hansen, J., Nazarenko, L., and Luo, Y.: Climate Effects of Black Carbon Aerosols in China and India, Science, 297, 2250-2253, 10.1126/science.1075159, 2002.

Mijling, B., and van der A, R. J.: Using daily satellite observations to estimate emissions of short-lived air pollutants on a mesoscopic scale, Journal of Geophysical Research: Atmospheres, 117, 10.1029/2012JD017817, 2012.

Mijling, B., van der A, R. J., and Zhang, Q.: Regional nitrogen oxides emission trends in East Asia observed from space, Atmospheric Chemistry and Physics, 13, 12003-12012, 10.5194/acp-13-12003-2013, 2013.

Ming, J., Xiao, C., Cachier, H., Qin, D., Qin, X., Li, Z., and Pu, J.: Black Carbon (BC) in the snow of glaciers in west China and its potential effects on albedos, Atmospheric Research92, 114-123, 10.1016/j.atmosres.2008.09.007, 2009.

Myriokefalitakis, S., Vrekoussis, M., Tsigaridis, K., Wittrock, F., Richter, A., Brühl, C., Volkamer, R., Burrows, J. P., and Kanakidou, M.: The influence of natural and anthropogenic secondary sources on the glyoxal global distribution, Atmospheric Chemistry and Physics, 8, 4965-4981, 10.5194/acp-8-4965-2008, 2008.

National Bureau of Statistics of China: China Power Statistical Yearbook (2005–2015), China Power Press, Beijing, China, 2015.

N. S. S. O. (NSSO), Household Consumption of various Goods and Services in India, (July 2009-June 2010), vol. KI of 69th round. National Sample Survey Office, Ministry of Statistics & Programme Implementation, Government of India, 2012a

N. S. S. O. (NSSO), Energy Sources of Indian Households, (July 2009-June 2010), vol. KI of 69th round. National Sample Survey Office, Ministry of Statistics & Programme Implementation, Government of India, 2012b

Ohara, T., Akimoto, H., Kurokawa, J.-I., Horii, N., Yamaji, K., Yan, X., and Hayasaka, T.: An Asian emission inventory of anthropogenic emission sources for the period 1980–2020, Atmospheric Chemistry and Physics, 7, 4419-4444, 2007.

Ott, L. E., Pickering, K. E., Stenchikov, G. L., Allen, D. J., DeCaria, A. J., Ridley, B., Lin, R.-F., Lang, S., and Tao, W.-K.: Production of lightning NOx and its vertical distribution calculated from three-dimensional cloud-scale chemical transport model simulations, Journal of Geophysical Research: Atmospheres, 115, 10.1029/2009JD011880, 2010.

Palmer, P. I., Jacob, D. J., Chance, K., Martin, R. V., Spurr, R. J. D., Kurosu, T. P., Bey, I., Yantosca, R., Fiore, A., and Li, Q.: Air mass factor formulation for spectroscopic measurements from satellites: Application to formaldehyde retrievals from the Global Ozone Monitoring Experiment, Journal of Geophysical Research: Atmospheres, 106, 14539-14550, 10.1029/2000JD900772, 2001.

Pettersson, E., Boman, C., Westerholm, R., Boström, D., and Nordin, A.: Stove Performance and Emission Characteristics in Residential Wood Log and Pellet Combustion, Part 2: Wood Stove, Energy & Fuels, 25, 315-323, 10.1021/ef1007787, 2011.

Pickering, K. E., Wang, Y., Tao, W.-K., Price, C., and Müller, J.-F.: Vertical distributions of lightning NOx for use in regional and global chemical transport models, Journal of Geophysical Research: Atmospheres, 103, 31203-31216, 10.1029/98JD02651, 1998.

Ramanathan, V., and Carmichael, G.: Global and regional climate changes due to black carbon, Nature Geosci, 1, 221-227, 2008.

Roth, S. D.: Ray casting for modeling solids, Computer Graphics and Image Processing, 18, 109-144, 10.1016/0146-664X(82)90169-1, 1982.

Rudlosky, S. D., and Fuelberg, H. E.: Pre- and Postupgrade Distributions of NLDN Reported Cloud-to-Ground Lightning Characteristics in the Contiguous United States, Mon Weather Rev, 138, 3623-3633, 10.1175/2010mwr3283.1, 2010.

Russell, A. R., Perring, A. E., Valin, L. C., Bucsela, E. J., Browne, E. C., Wooldridge, P. J., and Cohen, R. C.: A high spatial resolution retrieval of NO2 column densities from OMI: method and evaluation, Atmospheric Chemistry and Physics, 11, 8543-8554, 10.5194/acp-11-8543-2011, 2011.

Russell, A. R., Valin, L. C., and Cohen, R. C.: Trends in OMI NO2 observations over the United States: effects of emission control technology and the economic recession, Atmospheric Chemistry and Physics, 12, 12197-12209, 10.5194/acp-12-12197-2012, 2012.

Sack, T. M., Steele, D. H., Hammerstrom, K., and Remmers, J.: A survey of household products for volatile organic compounds, Atmospheric Environment. Part A. General Topics, 26, 1063-1070, 10.1016/0960-1686(92)90038-M, 1992.

Saha, S., Moorthi, S., Pan, H.-L., Wu, X., Wang, J., Nadiga, S., Tripp, P., Kistler, R., Woollen, J., Behringer, D., Liu, H., Stokes, D., Grumbine, R., Gayno, G., Wang, J., Hou, Y.-T., Chuang, H.-Y., Juang, H.-M. H., Sela, J., Iredell, M., Treadon, R., Kleist, D., Van Delst, P., Keyser, D., Derber, J., Ek, M., Meng, J., Wei, H., Yang, R., Lord, S., Van Den Dool, H., Kumar, A., Wang, W., Long, C., Chelliah, M., Xue, Y., Huang, B., Schemm, J.-K., Ebisuzaki, W., Lin, R., Xie, P., Chen, M., Zhou, S., Higgins, W., Zou, C.-Z., Liu, Q., Chen, Y., Han, Y., Cucurull, L., Reynolds, R. W., Rutledge, G., and Goldberg, M.: The NCEP Climate Forecast System Reanalysis, Bulletin of the American Meteorological Society, 91, 1015-1057, 10.1175/2010BAMS3001.1, 2010.

Schaaf, C. B., Gao, F., Strahler, A. H., Lucht, W., Li, X., Tsang, T., Strugnell, N. C., Zhang, X., Jin, Y., Muller, J.-P., Lewis, P., Barnsley, M., Hobson, P., Disney, M., Roberts, G., Dunderdale, M., Doll, C., d'Entremont, R. P., Hu, B., Liang, S., Privette, J. L., and Roy, D.: First operational BRDF, albedo nadir reflectance products from MODIS, Remote Sens Environ, 83, 135-148, 10.1016/S0034-4257(02)00091-3, 2002.

Shim, C., Wang, Y., Choi, Y., Palmer, P. I., Abbot, D. S., and Chance, K.: Constraining global isoprene emissions with Global Ozone Monitoring Experiment (GOME) formaldehyde column measurements, Journal of Geophysical Research: Atmospheres, 110, 10.1029/2004JD005629, 2005.

Singh, P., and Bengtsson, L.: Hydrological sensitivity of a large Himalayan basin to climate change, Hydrological Processes, 18, 2363-2385, 2004.

Stavrakou, T., Muller, J. F., De Smedt, I., Van Roozendael, M., Kanakidou, M., Vrekoussis, M., Wittrock, F., Richter, A., and Burrows, J. P.: The continental source of glyoxal estimated by the synergistic use of spaceborne measurements and inverse modelling, Atmospheric Chemistry and Physics, 9, 8431-8446, 10.5194/acp-9-8431-2009, 2009.

Streets, D. G., Bond, T. C., Carmichael, G. R., Fernandes, S. D., Fu, Q., He, D., Klimont, Z., Nelson, S. M., Tsai, N. Y., Wang, M. Q., Woo, J. H., and Yarber, K. F.: An inventory of gaseous and primary aerosol emissions in Asia in the year 2000, Journal of Geophysical Research: Atmospheres, 108, 8809, 10.1029/2002JD003093, 2003.

Tang, J. K., and Zhang, A. J.: The earth surface reflectance retrieval by exploiting the synergy of TERRA and AQUA MODIS data, Int Geosci Remote Se, 1697-1700, 10.1109/Igarss.2007.4423144, 2007.

Taylor, J. W., Allan, J. D., Allen, G., Coe, H., Williams, P. I., Flynn, M. J., Le Breton, M., Muller, J. B. A., Percival, C. J., Oram, D., Forster, G., Lee, J. D., Rickard, A. R., Parrington, M., and Palmer, P. I.: Size-dependent wet removal of black carbon in Canadian biomass burning plumes, Atmospheric Chemistry and Physics, 14, 13755-13771, 10.5194/acp-14-13755-2014, 2014.

Tian, H., Liu, K., Hao, J., Wang, Y., Gao, J., Qiu, P., and Zhu, C.: Nitrogen Oxides Emissions from Thermal Power Plants in China: Current Status and Future Predictions, Environmental Science & Technology, 47, 11350-11357, 10.1021/es402202d, 2013.

Tong, D. Q., Lamsal, L., Pan, L., Ding, C., Kim, H., Lee, P., Chai, T., Pickering, K. E., and Stajner, I.: Long-term NOx trends over large cities in the United States during the great recession: Comparison of satellite retrievals, ground observations, and emission inventories, Atmospheric Environment, 107, 70-84, 10.1016/j.atmosenv.2015.01.035, 2015.

van der Werf, G. R., Randerson, J. T., Giglio, L., Collatz, G. J., Mu, M., Kasibhatla, P. S., Morton, D. C., DeFries, R. S., Jin, Y., and van Leeuwen, T. T.: Global fire emissions and the contribution of deforestation, savanna, forest, agricultural, and peat fires (1997–2009), Atmospheric Chemistry and Physics, 10, 11707-11735, 10.5194/acp-10-11707-2010, 2010.

Veefkind, J. P., Aben, I., McMullan, K., Förster, H., de Vries, J., Otter, G., Claas, J., Eskes, H. J., de Haan, J. F., Kleipool, Q., van Weele, M., Hasekamp, O., Hoogeveen, R., Landgraf, J., Snel, R., Tol, P., Ingmann, P., Voors, R., Kruizinga, B., Vink, R., Visser, H., and Levelt, P. F.: TROPOMI on the ESA Sentinel-5 Precursor: A GMES mission for global observations of the atmospheric composition for climate, air quality and ozone layer applications, Remote Sens Environ, 120, 70-83, 10.1016/j.rse.2011.09.027, 2012.

Vermote, E. W., R: MYD09GA MODIS/Aqua Surface Reflectance Daily L2G Global 1kmand 500m SIN Grid, NASA LP DAAC, 10.5067/MODIS/MYD09GA.006, 2015.

Volkamer, R., Molina, L. T., Molina, M. J., Shirley, T., and Brune, W. H.: DOAS measurement of glyoxal as an indicator for fast VOC chemistry in urban air, Geophysical Research Letters, 32, 10.1029/2005GL022616, 2005.

Vrekoussis, M., Wittrock, F., Richter, A., and Burrows, J. P.: Temporal and spatial variability of glyoxal as observed from space, Atmospheric Chemistry and Physics, 9, 4485-4504, 10.5194/acp-9-4485-2009, 2009.

Wang, M., Xu, B., Wang, N., Cao, J., Tie, X., Wang, H., Zhu, C., and Yang, W.: Two distinct patterns of seasonal variation of airborne black carbon over Tibetan Plateau, Science of The Total Environment, 573, 1041-1052, 10.1016/j.scitotenv.2016.08.184, 2016.

Wang, S., Zhou, B., Wang, Z., Yang, S., Hao, N., Valks, P., Trautmann, T., and Chen, L.: Remote sensing of NO2 emission from the central urban area of Shanghai (China) using the mobile DOAS technique, Journal of Geophysical Research: Atmospheres, 117, 10.1029/2011JD016983, 2012.

Wang, X., Gong, P., Sheng, J., Joswiak, D. R., and Yao, T.: Long-range atmospheric transport of particulate Polycyclic Aromatic Hydrocarbons and the incursion of aerosols to the southeast Tibetan Plateau, Atmospheric Environment, 115, 124-131, 10.1016/j.atmosenv.2015.04.050, 2015.

Wang, Y., Jacob, D. J., and Logan, J. A.: Global simulation of tropospheric O3-NO x - hydrocarbon chemistry: 3. Origin of tropospheric ozone and effects of nonmethane hydrocarbons, Journal of Geophysical Research: Atmospheres, 103, 10757-10767, 10.1029/98JD00156, 1998.

Wang, Y., Choi, Y., Zeng, T., Ridley, B., Blake, N., Blake, D., and Flocke, F.: Late-spring increase of trans-Pacific pollution transport in the upper troposphere, Geophysical Research Letters, 33, 10.1029/2005GL024975, 2006.

Wang, Y., Choi, Y., Zeng, T., Davis, D., Buhr, M., Gregory Huey, L., and Neff, W.: Assessing the photochemical impact of snow emissions over Antarctica during ANTCI 2003, Atmospheric Environment, 41, 3944-3958, 10.1016/j.atmosenv.2007.01.056, 2007.

Wittrock, F., Richter, A., Oetjen, H., Burrows, J. P., Kanakidou, M., Myriokefalitakis, S., Volkamer, R., Beirle, S., Platt, U., and Wagner, T.: Simultaneous global

observations of glyoxal and formaldehyde from space, Geophysical Research Letters, 33, 5, 10.1029/2006gl026310, 2006.

Wu, Y., Zhang, S., Hao, J., Liu, H., Wu, X., Hu, J., Walsh, M. P., Wallington, T. J., Zhang, K. M., and Stevanovic, S.: On-road vehicle emissions and their control in China: A review and outlook, Science of The Total Environment, 574, 332-349, 10.1016/j.scitotenv.2016.09.040, 2017.

Xu, B., Cao, J., Hansen, J., Yao, T., Joswia, D. R., Wang, N., Wu, G., Wang, M., Zhao, H., Yang, W., Liu, X., and He, J.: Black soot and the survival of Tibetan glaciers, Proceedings of the National Academy of Sciences, 106, 22114-22118, 10.1073/pnas.0910444106, 2009.

Yang, Q., Wang, Y., Zhao, C., Liu, Z., Gustafson, W. I., and Shao, M.: NOx Emission Reduction and its Effects on Ozone during the 2008 Olympic Games, Environmental Science & Technology, 45, 6404-6410, 10.1021/es200675v, 2011.

Yao, T., Wang, Y., Liu, S., Pu, J., Shen, Y., and Lu, A.: Recent glacial retreat in High Asia in China and its impact on water resource in Northwest China, Science in China Series D: Earth Sciences, 47, 1065-1075, 10.1360/03yd0256, 2004.

Yasunari, T. J., Bonasoni, P., Laj, P., Fujita, K., Vuillermoz, E., Marinoni, A., Cristofanelli, P., Duchi, R., Tartari, G., and Lau, K. M.: Estimated impact of black carbon deposition during pre-monsoon season from Nepal Climate Observatory – Pyramid data and snow albedo changes over Himalayan glaciers, Atmospheric Chemistry and Physics, 10, 6603-6615, 10.5194/acp-10-6603-2010, 2010.

Zeng, T., Wang, Y., Chance, K., Browell, E. V., Ridley, B. A., and Atlas, E. L.: Widespread persistent near-surface ozone depletion at northern high latitudes in spring, Geophysical Research Letters, 30, 2298, 10.1029/2003GL018587, 2003.

Zeng, T., Wang, Y., Chance, K., Blake, N., Blake, D., and Ridley, B.: Halogen-driven low-altitude O3 and hydrocarbon losses in spring at northern high latitudes, Journal of Geophysical Research: Atmospheres, 111, D17313, 10.1029/2005JD006706, 2006.

Zhang, Q., Streets, D. G., Carmichael, G. R., He, K. B., Huo, H., Kannari, A., Klimont, Z., Park, I. S., Reddy, S., Fu, J. S., Chen, D., Duan, L., Lei, Y., Wang, L. T., and Yao, Z. L.: Asian emissions in 2006 for the NASA INTEX-B mission,

Atmospheric Chemistry and Physics, 9, 5131-5153, 10.5194/acp-9-5131-2009, 2009.

Zhang, R., Wang, H., Qian, Y., Rasch, P. J., Easter, R. C., Ma, P. L., Singh, B., Huang, J., and Fu, Q.: Quantifying sources, transport, deposition, and radiative forcing of black carbon over the Himalayas and Tibetan Plateau, Atmospheric Chemistry and Physics, 15, 6205-6223, 10.5194/acp-15-6205-2015, 2015.

Zhang, R., Wang, Y., He, Q., Chen, L., Zhang, Y., Qu, H., Smeltzer, C., Li, J., Alvarado, L. M. A., Vrekoussis, M., Richter, A., Wittrock, F., and Burrows, J. P.: Enhanced trans-Himalaya pollution transport to the Tibetan Plateau by cut-off low systems, Atmospheric Chemistry and Physics, 17, 3083-3095, 10.5194/acp-17-3083-2017, 2017.

Zhang, Y., Wang, X., Blake, D. R., Li, L., Zhang, Z., Wang, S., Guo, H., Lee, F. S., Gao, B., and Chan, L.: Aromatic hydrocarbons as ozone precursors before and after outbreak of the 2008 financial crisis in the Pearl River Delta region, south China, Journal of geophysical research: atmospheres, 117, 2012.

Zhang, Y., Wang, Y., Gray, B. A., Gu, D., Mauldin, L., Cantrell, C., and Bandy, A.: Surface and free tropospheric sources of methanesulfonic acid over the tropical Pacific Ocean, Geophysical Research Letters, 41, 2014GL060934, 10.1002/2014GL060934, 2014.

Zhang, Y., and Wang, Y.: Climate-driven ground-level ozone extreme in the fall over the Southeast United States, Proceedings of the National Academy of Sciences, 113, 10025-10030, 10.1073/pnas.1602563113, 2016.

Zhang, Y., Wang, Y., Chen, G., Smeltzer, C., Crawford, J., Olson, J., Szykman, J., Weinheimer, A. J., Knapp, D. J., Montzka, D. D., Wisthaler, A., Mikoviny, T., Fried, A., and Diskin, G.: Large vertical gradient of reactive nitrogen oxides in the boundary layer: Modeling analysis of DISCOVER-AQ 2011 observations, Journal of Geophysical Research: Atmospheres, 121, 1922-1934, 10.1002/2015JD024203, 2016.

Zhao, C., and Wang, Y.: Assimilated inversion of NOx emissions over east Asia using OMI NO2 column measurements, Geophysical Research Letters, 36, L06805, 10.1029/2008GL037123, 2009.

Zhao, C., Wang, Y., and Zeng, T.: East China Plains: A “Basin” of Ozone Pollution, Environmental Science & Technology, 43, 1911-1915, 10.1021/es8027764, 2009a.

Zhao, C., Wang, Y., Choi, Y., and Zeng, T.: Summertime impact of convective transport and lightning NOx production over North America: modeling dependence on meteorological simulations, Atmospheric Chemistry and Physics, 9, 4315-4327, 10.5194/acp-9-4315-2009, 2009b.

Zhao, C., Wang, Y., Yang, Q., Fu, R., Cunnold, D., and Choi, Y.: Impact of East Asian summer monsoon on the air quality over China: View from space, Journal of Geophysical Research: Atmospheres, 115, D09301, 10.1029/2009JD012745, 2010.

Zhao, Z., Cao, J., Shen, Z., Xu, B., Zhu, C., Chen, L. W. A., Su, X., Liu, S., Han, Y., Wang, G., and Ho, K.: Aerosol particles at a high-altitude site on the Southeast Tibetan Plateau, China: Implications for pollution transport from South Asia, Journal of Geophysical Research: Atmospheres, 118, 11,360-311,375, 10.1002/jgrd.50599, 2013.

Zhou, Y., Brunner, D., Boersma, K. F., Dirksen, R., and Wang, P.: An improved tropospheric NO2 retrieval for OMI observations in the vicinity of mountainous terrain, Atmospheric Measurement Techniques, 2, 401-416, 10.5194/amt-2-401-2009, 2009.

Zou, Y., Wang, Y., Zhang, Y., and Koo, J.-H.: Arctic sea ice, Eurasia snow, and extreme winter haze in China, Science Advances, 3, 10.1126/sciadv.1602751, 2017.